

Scuola di Scienze

Corso di Laurea Magistrale in Fisica del Sistema Terra

**Arctic Ocean**  
**Submesoscale Brine Driven Eddies:**  
**Modeling of a Sea Ice Edge Front**

Supervisor:

Prof. Nadia Pinardi

Submitted by:

Anna Lo Piccolo

Advisors:

Prof. Baylor Fox-Kemper

Prof. Christopher Horvat

Sessione III

Anno Accademico 2019 · 2020

# Abstract

Characteristic features of the wintertime Arctic Ocean are narrow and elongated fractures in the sea ice cover, up to hundreds of kilometers long and up to tens of kilometers wide, called leads. Leads expose the ocean to the cold atmosphere, establishing air-sea heat fluxes which freeze the oceanic surface. During new sea ice formation, dense and salt-enriched plumes of brine are rejected into the oceanic mixed layer. Due to brine rejection, lateral density gradients appear at sea ice edges, creating fronts. Fronts store potential energy and are subjected to gravitational overturning. The effect of Earth's rotation prevents the complete slumping establishing along sea ice edge currents in a geostrophic balance state, known as geostrophic adjustment, leaving the isopycnals tilted. Baroclinic instabilities develop and grow into submesoscale eddies – typical vortical coherent structures of the oceanic mixed-layer. Transferring momentum and tracer properties laterally, submesoscale eddies are the leading order process of mixed-layer restratification. Current global climate models can not resolve this small scale turbulence and Arctic Ocean observations are limited due to the presence of sea ice. High resolution numerical models are therefore a powerful tool for investigating these unknown processes. In this work, idealized high resolution model experiments are setup in order to study the wintertime refreezing of an open ocean area near a sea ice edge. The results confirm that submesoscale eddies enhance the mixed-layer restratification subtracting energy from the mean flow and increasing the turbulent kinetic energy. Through the study of lateral density transfer scaling rate, a departure from the deformation radius emerges in geostrophic adjustment experiments and more strongly under ageostrophy predominance. The presence of an ageostrophic diffusion process can explain the frontal region widening.

# Sommario

L'Oceano Artico nella stagione invernale è caratterizzato da lunghe e strette fratture nello spesso strato di ghiaccio marino, chiamate *leads*, che espongono la superficie dell'acqua alle fredde temperature artiche, liberando, durante il congelamento, sacche di acqua ipersalata che fluiscono nel *mixed-layer* oceanico. Questo processo, noto come *brine rejection* crea gradienti orizzontali di densità tra le due zone di acqua di mare separate dal bordo del ghiaccio, dando luogo a un fronte oceanico, che contiene energia potenziale. L'effetto della rotazione terrestre impedisce al fronte di cadere sotto l'effetto della gravità, creando uno stato di equilibrio in bilancio geostrofico. A seguito di questo processo, chiamato *geostrophic adjustment*, le perturbazioni presenti a causa della instabilità baroclina si trasformano in strutture vorticoso tipiche del *mixed-layer* oceanico – *submesoscale eddies*. Gli *eddies*, grazie al loro trasferimento laterale di energia e di altre proprietà dell'acqua marina, riescono a ristrutturare con efficacia la superficie dell'oceano. Questi processi di piccola scala non possono essere rilevati dagli attuali modelli climatici globali. Inoltre, la presenza di spessi strati di ghiaccio rende difficoltose le osservazioni dell'Oceano Artico. Per questi motivi, si preferisce ricorrere all'uso di modelli numerici ad alta risoluzione che permettono di studiare e comprendere i fenomeni ancora poco conosciuti. Il presente elaborato studia i processi che causano il ricongelamento della superficie marina a contatto con un bordo di ghiaccio durante la stagione invernale, utilizzando simulazioni numeriche ad alta risoluzione. I risultati confermano l'effetto dei *submesoscale eddies* nel processo di ristrutturazione e suggeriscono l'esistenza di diffusione per spiegare il maggiore allargamento della regione frontale rispetto al raggio di deformazione tipico del *geostrophic adjustment*, che è osservato anche in assenza di *submesoscale eddies*.

# Contents

<b>Introduction</b>	<b>5</b>
<b>1 Phenomenology and Theoretical basis</b>	<b>7</b>
1.1 Polar regions and climate change . . . . .	7
1.2 Arctic Ocean, stratification and circulation . . . . .	10
1.3 Sea ice . . . . .	13
1.3.1 Sea ice dynamics and thermodynamics . . . . .	14
1.3.2 Polynyas and leads . . . . .	16
1.3.3 Brine rejection phenomenon . . . . .	18
1.4 Observations in the Arctic Ocean . . . . .	19
1.5 Global climate models . . . . .	21
1.5.1 Smagorinsky viscosity . . . . .	25
1.6 Submesoscale eddies . . . . .	26
1.6.1 Mesoscale and submesoscale baroclinic instability . . . . .	27
1.6.2 Mixed-layer eddies in the frontal spin-down problem . . . . .	31
1.6.3 Geostrophic adjustment . . . . .	32
1.6.4 Mixed-layer eddy phenomenology . . . . .	34
1.6.5 Mixed-layer eddy parametrization . . . . .	36
1.7 Previous studies in the Arctic . . . . .	37
1.8 Motivations and objectives . . . . .	39
<b>2 Numerical model configuration and Diagnostics</b>	<b>41</b>
2.1 MITgcm model . . . . .	41
2.1.1 Hydrostatic form . . . . .	44
2.1.2 Model discretization and algorithm . . . . .	45
2.1.3 Thermodynamic sea ice package . . . . .	50
2.1.4 CheapAML package . . . . .	51
2.1.5 Eddy viscosity and diffusivity . . . . .	51
2.2 Numerical model configuration . . . . .	52
2.2.1 Initial ocean state . . . . .	52
2.2.2 External atmospheric forcing . . . . .	53

2.2.3	Two and three-dimensional configurations . . . . .	53
2.2.4	Coriolis parameter . . . . .	55
2.2.5	Covered and open ocean configurations . . . . .	55
2.3	Diagnostics . . . . .	56
2.3.1	Anomalies from initial state . . . . .	56
2.3.2	The along ice-edge average . . . . .	57
2.3.3	Buoyancy budget . . . . .	58
2.3.4	Potential vorticity budget . . . . .	58
2.3.5	Energy budget . . . . .	60
2.3.6	Overturning streamfunction . . . . .	62
<b>3</b>	<b>Results and Discussion</b>	<b>64</b>
3.1	Surface forcing . . . . .	64
3.2	Sea ice thermodynamics . . . . .	66
3.3	Characterization of the dynamics . . . . .	67
3.3.1	Eddy visualization . . . . .	67
3.3.2	Surface velocity field . . . . .	69
3.4	Effect of brine rejection . . . . .	71
3.4.1	Buoyancy evolution . . . . .	71
3.4.2	Stratification . . . . .	76
3.5	Geostrophic currents . . . . .	78
3.6	Potential vorticity dynamics . . . . .	80
3.7	Energetics . . . . .	83
3.8	Eulerian and eddy overturning streamfunctions . . . . .	88
3.9	Lateral density transfer scale analysis . . . . .	91
	<b>Conclusion</b>	<b>96</b>
	<b>A Derivation of MLE parametrization</b>	<b>99</b>
	<b>B Derivation of the Ertel PV equation</b>	<b>102</b>
	<b>C Derivation of MKE and EKE equations</b>	<b>104</b>
	<b>Acknowledgements</b>	<b>107</b>
	<b>Bibliography</b>	<b>107</b>

# Introduction

Polar regions are an important part of the Earth System that, at present and in the near future, is facing challenges due to climate change. Global warming is forcing rapid changes, especially in the Arctic, that affect global climate, high-latitude marine ecosystems in the Northern Hemisphere, and the socio-economical systems that rely on this region. The presence of sea ice creates a unique environment modifying the heat exchange between the atmosphere and the ocean, which ultimately impacts the global energy balance. The study of the Arctic Ocean is the study of ocean, sea ice and their interactions – a variety of different processes occurring at the same time and enhancing one another.

Wintertime oceanic surface areas exposed to the cold atmosphere contribute to the formation of dense water when sea ice forms. During polar winter, large consolidated regions of sea ice can crack and create long and narrow elongated fractures, called leads, up to hundreds of kilometers long and up to tens of kilometers wide. These openings freeze, releasing great amount of latent heat. During new sea ice formation, salt-enriched water is rejected from the largely fresh sea ice and injected into the oceanic mixed-layer in the form of dense plumes of brine. Fronts at sea ice edges are formed and store potential energy, but are soon subjected to gravitational overturning. The effect of Earth's rotation creates along sea ice edge currents in a geostrophic balance state, known as geostrophic adjustment. This prevents the complete frontal spin-down. The tilted isopycnals are then baroclinically unstable and lead to the development of mixed-layer eddies (MLEs), also called submesoscale eddies. Submesoscale eddies are the leading order process of mixed-layer restratification at mid latitudes [*Boccaletti et al.*, 2007; *Fox-Kemper et al.*, 2008]. They can be important also at high latitudes where the weak diurnal cycle during polar night and the continuous supply of brine even after a thin layer of sea ice is created let submesoscale eddies grow and spread laterally.

Due to their coarse resolution, global climate models (GCMs) can't resolve small scale processes, such as submesoscale turbulence or leads. Thus this requires that scientists study these features to develop parameterizations. In addition,

the presence of sea ice in the Arctic Ocean causes a lack of consistent data from observations. High resolution numerical models are therefore a powerful tool for investigating these unknown processes and understanding the effects of subgrid scale turbulence on the resolved flow.

In this work, idealized high resolution numerical model experiments are setup in order to investigate and quantify the complexity of the frontal circulation at an Arctic Ocean sea ice edge. The Massachusetts Institute of Technology general circulation model (MITgcm) [Marshall *et al.*, 1997] in the hydrostatic form coupled with the thermodynamic sea ice package [Winton, 2000] is used. The initial atmospheric and oceanic conditions resemble a highly simplified wintertime Arctic Ocean: constant air temperature and quiescent ocean at the freezing point temperature. Different experiments are compared to evaluate the effects of different forcing in the system. The output of the simulations are then diagnosed by visualizing the ocean response to forcing conditions and separating between mean and turbulent flows. The length scale proposed by Matsumura and Hasumi [2008] for the frontal spin-down process at a re-freezing lead is discussed. The single sea ice edge system is considered as a necessary step toward the more challenging lead configuration of two interacting ice edges.

Arctic Ocean stratification and circulation, sea ice dynamics, and phenomenology of brine rejection are shown in Chapter 1. Observations in the Arctic Ocean and global climate models are also introduced. Then theoretical basis for frontal spin-down process and submesoscale turbulence are presented. At the end of the chapter previous studies at Arctic Ocean leads and motivations and objectives of this thesis are explained. The MITgcm model and its characteristics are presented in Chapter 2. The experimental setups and the diagnostic tools used in this work are also provided. Results are shown and discussed in Chapter 3. A conclusion is then given at the end of the thesis.

# Chapter 1

## Phenomenology and Theoretical basis

In this chapter the theoretical basis for the development of the modeling experiments carried out in this work are presented. First, the importance of the polar regions in a climate change perspective and the Arctic Ocean characteristics, stratification and circulation are shown in Sec. 1.1 and 1.2. Secondly, sea ice dynamics and thermodynamics is introduced in Sec. 1.3, with a focus on the brine rejection phenomenon, which typically happens in wintertime opening structures such as leads and polynyas. Finally, the limitations of observations in the Arctic Ocean and of coarse resolution climate models, treated in Sec. 1.4 and 1.5, emphasize the importance of deeply understanding the submesoscale restratification mechanism (Sec. 1.6) and lead to the motivations of this study (Sec. 1.8).

### 1.1 Polar regions and climate change

Polar regions are greatly affected by climate change. Of particular interest are the northern hemisphere high latitudes, where the global warming is leading to a completely new environment, due to sea ice cover disappearing (Fig. 1.1). One of the key signal of climate change is the decline of the Arctic sea ice cover that has been recorded in satellite imagery since 1970s. It is estimated that since 1979 the areal proportion of thick ice at least 5 years old has declined by approximately 90% [IPCC, 2019]. The transition to ice-free summer is projected for around 2050 [Collins *et al.*, 2013a] (Fig. 1.2).

The presence of sea ice is of vital importance for the resilience of the Arctic ecosystem. Polar sea ice provides one of the most extensive habitat on Earth, accomplishing a unique marine and terrestrial biology [Arrigo, 2014]. The decreasing

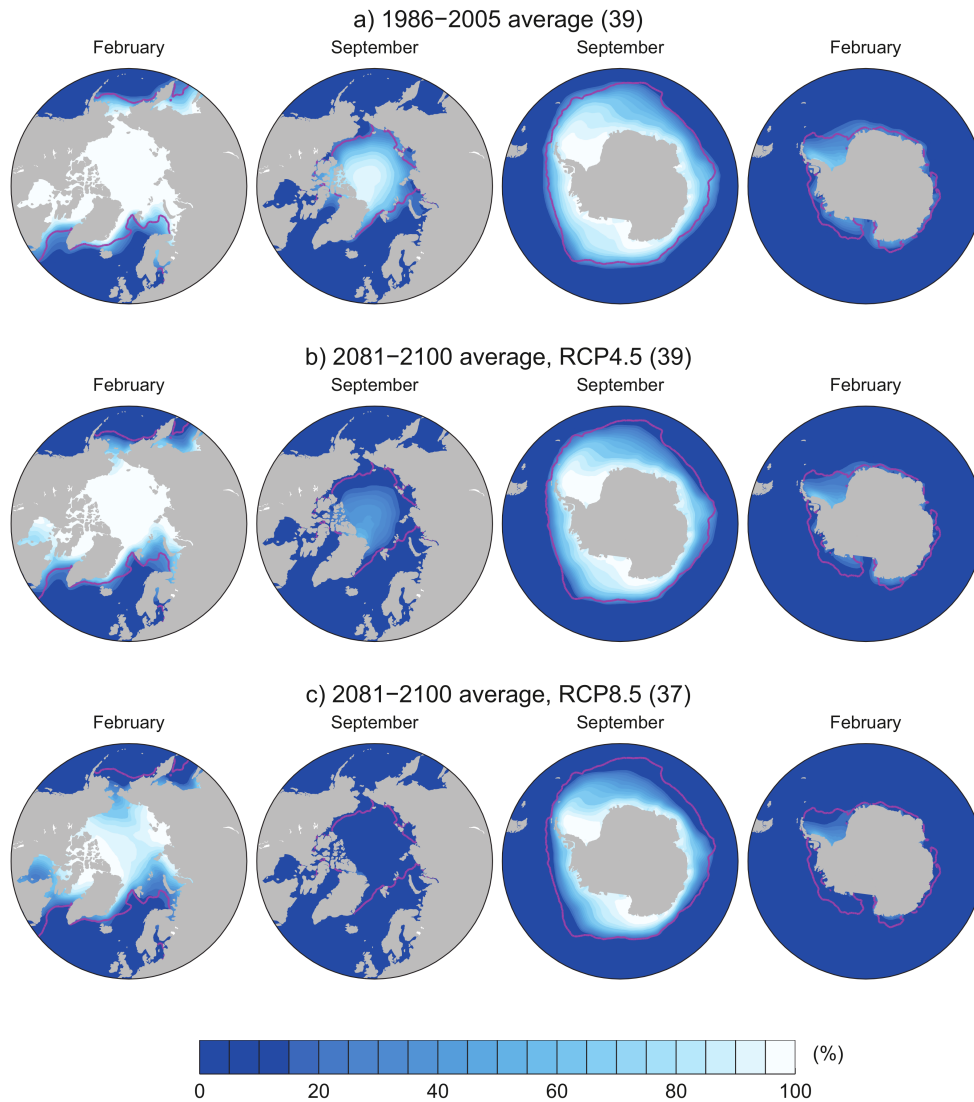


Figure 1.1: February and September CMIP5 multi-model mean sea ice concentrations (%) in the Northern and Southern Hemispheres for the periods (a) 1986–2005, (b) 2081–2100 under RCP4.5 and (c) 2081–2100 under RCP8.5. The pink lines indicate the observed 15% sea ice concentration limits averaged over 1986–2005. Figure from *Collins et al.* [2013a] in the IPCC report.

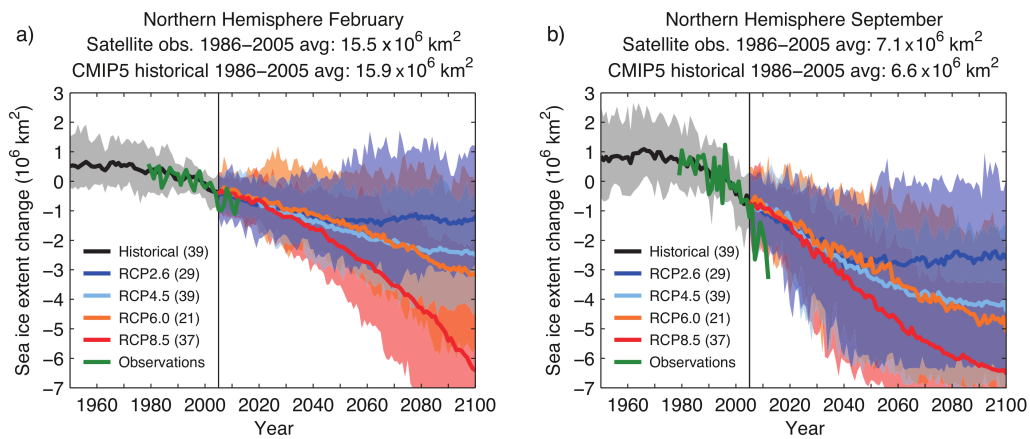


Figure 1.2: Changes in the Arctic sea ice extent as simulated by CMIP5 models under RCP2.6, RCP4.5, RCP6.0 and RCP8.5 projections. Solid curves show the multi-model means and the shading denotes the 5 to 95% range of the ensemble. The vertical line marks the end of CMIP5 historical climate change simulations. Sea ice extent is defined as the total ocean area where sea ice concentration exceeds 15%. Changes are relative to the reference period 1986–2005. Also plotted (solid green curves) are satellite data. Figure from *Collins et al.* [2013a] in the IPCC report.

sea ice extent and the reduction in sea ice thickness is opening to new shipping viable routes bringing together many implications such as the intensification of commerce via the Arctic Ocean, the increase in risks and noise, the exploitation of the energetic resources of the Arctic and the increase of black carbon emissions from shipping activity [IPCC, 2019]. Beside the natural Arctic organisms, also the human population of the Arctic depends on ice sheets and sea ice for survival. Accordingly to the IPCC [2019], four million people reside in the Arctic region, 10% of which is indigenous.

Due to the ice albedo feedback, changes in the Arctic climate are enhanced one another, a process known as Arctic amplification. Indeed, higher air temperatures melt sea ice and reduce its albedo, thus further increasing temperatures and causing a positive feedback. The Arctic is warming faster than the global mean and its ocean is increasing the heat content.

A combination of general circulation models (GCMs) and regional climate models integrated with in situ measurements and satellite observations are powerful tools to investigate climate change. However, due to the presence of sea ice and the complex air-sea-ice-ocean interactions, still many processes remain unknown. In fact, current climate models can not have the high resolution needed to resolve the small scale phenomena, such as the highly variable heat flux. Furthermore, the presence of sea ice limits the observations of the Arctic Ocean. For these reasons, conceptual models can guide scientists to have a better understanding of small scale phenomena, and may suggest new subgridscale parametrizations to improve GCMs [Maslowski *et al.*, 2012; Timmermans and Marshall, 2020].

Since Arctic sea ice cover extent reaches its minimum in September after the melting season, many studies focus on the small scale effects in the melting season. However, an important heat exchange between the atmosphere and the ocean also happens in wintertime, when the refreezing of the exposed open ocean areas injects dense plumes of brine into the ocean. Brine rejection at a refreezing sea ice edge is the focus of this work.

## 1.2 Arctic Ocean, stratification and circulation

The Arctic Ocean, also called Arctic Mediterranean, is a large deep semi-enclosed basin of water centered in the north pole and surrounded by lands and shallower channels. In winter, it is entirely covered by a thin layer of sea ice, which is not permanent throughout the year. In the Arctic, sea ice cover, in fact, has a large seasonal cycle. The bathymetry of the Arctic Ocean is very complex. The

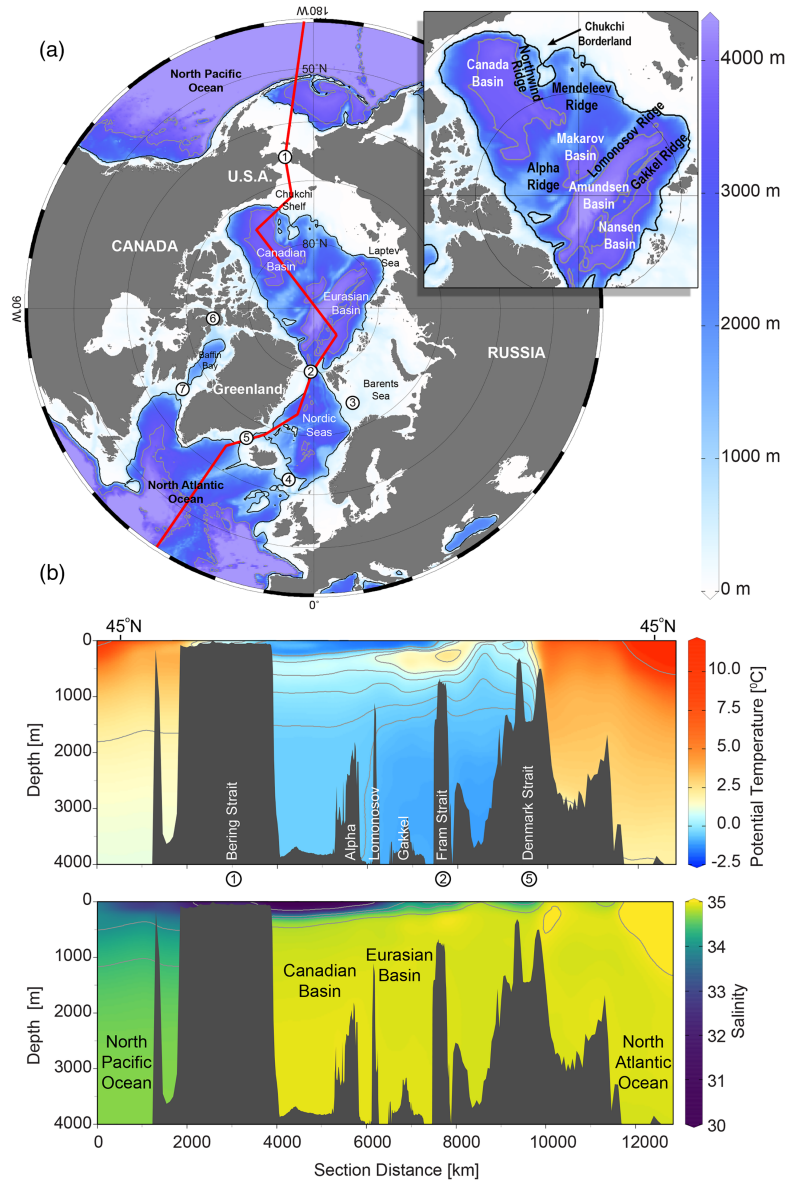


Figure 1.3: The Arctic Ocean. (a) The main geographic features of the Arctic. The 1000 m and 3500 m bathymetric contours are shown. Numbers refer to (1) Bering Strait, (2) Fram Strait, (3) Barents Sea Opening, (4) Greenland-Scotland Ridge, (5) Denmark Strait, (6) Lancaster Sound, and (7) Davis Strait. (b) potential temperature and salinity sections following red line in (a) from the Pacific Ocean, left, to the Atlantic Ocean, right. Figure taken from *Timmermans and Marshall [2020]*.

Central Arctic basin can be divided into two main basins, the Eurasian and the Canadian Basins of about 4000 m depth, separated by the Lomonosov Ridge of 1500 m depth. Fram Strait and Barents Sea are the openings of the Central Arctic toward the Nordic Seas, and, thence, toward the Atlantic Ocean, with relatively warm and salty water; Bering Strait is the connection with the Pacific Ocean, relatively warm and fresh.

The freshwater balance in the Arctic Ocean is composed by inflows of water from the Atlantic and the Pacific Oceans and rivers runoff and precipitation and outflows of water through channels in the Canadian Archipelago and via Fram Strait. Melting and freezing of sea ice are also part of the hydrological cycle. They are seen as the high latitude equivalent of precipitation and evaporation respectively [*Aagaard and Carmack, 1989*].

In winter and in permanent sea ice regions, sea surface temperature is at freezing point, which, for seawater, is about  $-2^{\circ}\text{C}$ , and it can reach few degrees above 0 in summer free-ice regions. The mean salinity of the Arctic ocean is 34.8 psu [*IPCC, 2019*]. The Arctic Ocean stratification is predominately set by salinity. This is because, at high latitude, the density distribution is governed by changes in salinity more than changes in temperature. In fact, in the linearized equation of state

$$\rho = \rho_0[1 - \alpha(T - T_0) + \beta(S - S_0)] \quad (1.1)$$

where the dependence on pressure changes has been neglected,  $\alpha$  is the thermal expansion coefficient and  $\beta$  is the haline contraction coefficient,  $\alpha$  is almost proportional to temperature. Thus, at low temperature, temperature changes in the equation of state of seawater are smaller than salinity changes:  $\beta/\alpha = 30$  and 10 (in units of K/psu) at freezing point and  $2^{\circ}\text{C}$  respectively and 34.5 psu, and the variability ranges for temperature and salinity are of the same order of magnitude. For this reason, polar oceans are also called  $\beta$ -oceans, to differentiate from the  $\alpha$ -oceans at subtropical latitudes stratified in temperature.

Thereby, since at high latitude the ocean pycnocline is mainly a halocline rather than a thermocline, the Arctic Ocean waters are separated in surface fresh water and deep salty water, forming a mixed layer of 25-50 m in winter and 5-30 m in summer [*Peralta-Ferriz and Woodgate, 2015*]. The inflow of warm and salty Atlantic water sits beneath the surface Arctic water, between 150 and 500 m depth at a temperature of 0 to  $3^{\circ}\text{C}$ , preventing warming of the mixed layer and melting of sea ice. In other words, the presence of sea ice at the surface is guaranteed by the stratification in salinity of the Arctic Ocean. Changes in freshwater cycle of the Arctic implies changes in stratification, circulation and mixing.

The Arctic Ocean circulation is mainly driven by buoyancy and it can be explained as an estuarine-like with the inflow from Nordic Seas and outflow of freshwater. But there are also two main wind driven circulation patterns that follow the atmospheric circulation. The Beaufort Gyre is an anticyclonic motion swinging around a high pressure in the Canadian Basin, acting as a reservoir of freshwater; the Transpolar Drift Stream, due to the presence of a low pressure above Iceland, drives the outflow of freshwater via Fram Strait. Melting and growing of sea ice play important role in the circulation of the Arctic Ocean by injecting freshwater and brine, respectively.

### 1.3 Sea ice

In addition to the seasonal cycle, Arctic sea ice has also strong spatial variability in horizontal and vertical directions. Sea ice is made up by many floating individual pieces, floes, from meters to tens of kilometers across with thickness of centimeters up to tens of meters with a winter average of 2 m. Sea ice cover extent is maximum in March and minimum in September. Sea ice can be distinguished into perennial and seasonal ice accordingly to its capability of survive a melting season.

Sea ice evolves accordingly to thermodynamics and dynamics forcing which set the melting/freezing and the motion of sea ice, respectively. Thermodynamics forcing are given by energy fluxes at the surface, internally and at the bottom of sea ice (schematic on the left in Fig. 1.4). They depend on the albedo, i.e. the fraction of incident solar energy reflected by a surface. Sea ice covered by snow has an albedo of 0.85, bare ice of 0.65, melt ponds of 0.2-0.4 and dark ocean of 0.07 [Perovich and Richter-Menge, 2009]. If the sum of the energy fluxes is negative sea ice cools and grows, if it is positive sea ice warms and melts. Convergence and divergence of sea ice cause changes in sea ice thickness creating open water areas and ridges. The acceleration of sea ice is due to the wind, ocean and internal sea ice stresses (schematic on the right in Fig. 1.4). Wind stress can move sea ice up to tens of kilometers per day [Perovich and Richter-Menge, 2009]. Furthermore, the presence of sea ice modifies the wind stress on the surface of the ocean creating a buffer between air and water.

Sea ice can also be classified into land-fast ice and pack ice. Land-fast ice is sea ice that forms in shallow waters, anchored to land or ice shelves, almost immobile. Pack ice is sea ice that freezes offshore, in open waters, and is free to drift with winds and oceanic currents.

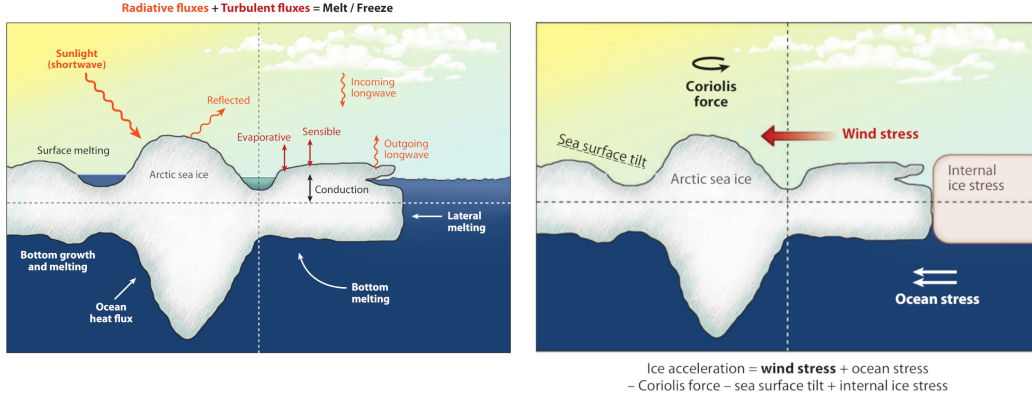


Figure 1.4: Schematic of heat budget (left) and momentum balance (right) of sea ice. Figures adapted from *Perovich and Richter-Menge* [2009].

### 1.3.1 Sea ice dynamics and thermodynamics

The sea ice dynamics is well described by the viscous-plastic model proposed by Hibler in 1979 who considered sea ice as a continuous media, and in particular as a non linear viscous compressible fluid [Hibler, 1979]. The momentum balance includes air and water stresses, Coriolis force, internal ice stress, inertial forces and ocean tilt:

$$m \frac{D\mathbf{u}}{Dt} = -mf \mathbf{k} \times \mathbf{u} + \boldsymbol{\tau}_{air} + \boldsymbol{\tau}_{ocean} - m\nabla\phi + \mathbf{F} \quad (1.2)$$

written in the plane of motion of sea ice (i.e. vertically averaged momentum equation).  $D/Dt = \partial/\partial t + \mathbf{u} \cdot \nabla$  is the material derivative,  $\mathbf{u}$  is the ice velocity,  $\mathbf{k}$  a unit vector normal to the surface,  $m$  the ice mass per unit area,  $\phi$  the sea surface height potential and  $\mathbf{F}$  the internal force, which is given by a constitutive law for sea ice. Air and ocean stresses,  $\boldsymbol{\tau}_{air}$  and  $\boldsymbol{\tau}_{ocean}$ , computed with the boundary layer theories, can be scaled with the square of the friction velocities for air and ocean boundary layers,  $\tau \propto \rho u^{*2}$ .

Sea ice thermodynamics is interested in studying the evolution of sea ice volume given the heat fluxes that seasonally freeze and melt sea ice. Obviously, sea ice thermodynamics and dynamics are not uncorrelated one each other. But, accordingly to the time scale of the problem one wants to study, some approximation can be made. Supposing to know the solution of (1.2), i.e. the sea ice velocity, the evolution of sea ice volume per unit area,  $V$ , i.e. of sea ice thickness, is given by:

$$\frac{\partial V}{\partial t} + \mathbf{u} \cdot \nabla V = F_T \quad (1.3)$$

where the first term is the rate of change of sea ice volume, the second term is the

advection of sea ice volume due to sea ice motions  $\mathbf{u}$ , and  $F_T$  is the rate of change of sea ice volume due to thermodynamics forcing

$$F_T \sim \frac{Q_{net}}{\rho_{ice} L_f} \quad (1.4)$$

where  $Q_{net}$  is the net heating ( $Q_{net} > 0$ ) or cooling ( $Q_{net} < 0$ ) per unit area ( $\text{W/m}^2$ ),  $L_f$  is the latent heat of freezing, which is the energy released when freezing a unit mass of ice at freezing point ( $\text{J/kg}$ ), without changing temperature. In the upper bound free drift motion regime, the sea ice velocity in (1.3) can be approximated with the friction velocity of sea ice  $\mathbf{u}_{ice}^*$  and thus scaled with  $\sqrt{\tau/\rho_{ice}}$  with  $\tau$  representing the combined effect of air and ocean stresses. Equation (1.3) expresses the rate of change of sea ice volume due to both dynamics and thermodynamics forcing. Although the sea ice evolution is due to the coupling of dynamics and thermodynamics, a dimensionless parameter can be defined as the ratio between thermodynamics forcing versus dynamics forcing and helps in distinguishing the two limits:

$$\Sigma = \frac{F_T}{\mathbf{u} \cdot \nabla V} \sim \frac{Q_{net}}{L_f \sqrt{\tau \rho_{ice}}} \frac{L}{V_0} \quad (1.5)$$

where  $L$  is the typical length scale of sea ice motion and  $\mathbf{u}_{ice}^* \sim \sqrt{\tau/\rho_{ice}}$  has been used to scale the sea ice velocity. Accordingly to the magnitude of  $\Sigma$ , two regimes can be defined:

$$|\Sigma| \ll 1 \quad F_T \ll \mathbf{u} \cdot \nabla V \quad \text{Dynamics regime} \quad (1.6)$$

$$|\Sigma| \gg 1 \quad F_T \gg \mathbf{u} \cdot \nabla V \quad \text{Thermodynamics regime} \quad (1.7)$$

The thermodynamics regime can be split into two regimes: the melting regime  $Q_{net} > 0$  and the freezing regime  $Q_{net} < 0$ . Many studies focus on the dynamics regime [*Richter-Menge and Elder, 1998; Häkkinen, Sirpa, 1986; Manucharyan and Thompson, 2017*]. Other studies, instead, focus on the melting regime [*Horvat et al., 2016; Horvat and Tziperman, 2018*]. Finally, also the freezing condition, the importance of which will be explained in next sections, has been long studied [*Matsumura and Hasumi, 2008; Bush and Woods, 1999, 2000; Smith IV and Morison, 1998; Skyllingstad and Denbo, 2001; Smith IV et al., 2002*], but still some open questions remain.

The purpose of this work is to study the ocean response at a sea-ice edge during wintertime Arctic conditions, and the  $\Sigma \ll -1$  regime is considered, with  $Q_{net} < 0$  and sea ice thermodynamics dominant over sea ice dynamics.

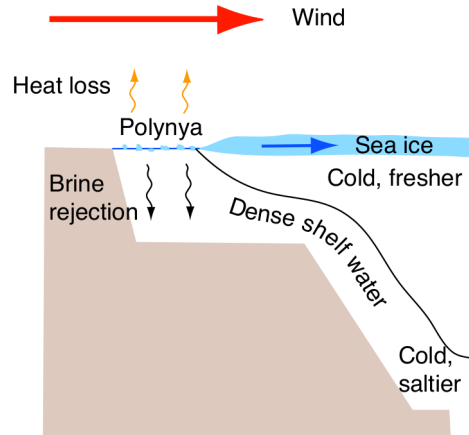


Figure 1.5: Schematics of polynya formation. Figure from *Talley* [2011].

### 1.3.2 Polynyas and leads

Due to its insulating property, sea ice cover creates a buffer between the ocean and the atmosphere through a gradient of temperature inside the sea ice layer, affecting interactions of heat, mass and momentum transport between ocean and atmosphere. However, sea ice can crack creating fractures and openings within the ice cover and expose the ocean to the cold temperature of the atmosphere. Indeed, these openings and fractures are typical features of the winter Arctic sea ice that exhibits recurring shapes, such as polynyas and leads.

Polynyas are areas of open water surrounded by sea ice that form almost always in the same places each year near the coast or the land-fast ice, due to the action of winds [*IPCC*, 2019] (Fig. 1.5). They represent an essential habitat for mammals and birds, being corridors for migration of marine animals [*Stirling*, 1997; *Smith et al.*, 1990].

Leads, that occupy the majority of opening fraction, are near linear elongated fractures in the sea ice crust (Fig. 1.6). Leads can form from dynamical stresses that impress divergence of sea ice. Their length can vary from few hundreds of meters to hundreds of kilometers and with more than 50 meters width [*Schulson*, 2004; *Willmes and Heinemann*, 2016].

In winter openings, due to the large temperature difference between the ocean and the atmosphere, which reaches 20-40°C [*Smith et al.*, 1990], large heat fluxes out of the ocean toward the atmosphere are established and the surface of the ocean starts to freeze. Under cooling conditions, a negative feedback is maintained: the



Figure 1.6: Sun glint off a sea ice lead in an otherwise heavily ridged ice pack, Canada Basin (Arctic Ocean). Image Credit: NASA/Sinead Farrell.

creation of open water areas implies an increasing sea ice growth [Zhang *et al.*, 2000]. This sea ice growth stabilizing feedback opposes to the so called ice-albedo feedback. However, the former is active in wintertime, while the latter in summertime [Pegau and Paulson, 2001]. Wintertime leads can lose 200-500 W/m<sup>2</sup> of heat to the atmosphere [Talley, 2011], which is a great amount if compared to the incoming solar radiation at the top of the atmosphere of about 314 W/m<sup>2</sup>, and account for almost one half of the total oceanic heat loss, even though they occupy less than 10% of the surface area. As already mentioned, freezing is considered as the high latitude equivalent of evaporation. Several meters of ice are typically annually formed in the polar regions with a distillation rate compared to the evaporation rate in the highly evaporative Red Sea, about 2 meters per year [Aagaard and Carmack, 1989].

Leads are subject of study for geophysicists interested in understanding their formation from deformation of sea ice cover and their density distribution. Leads have been observed using satellite imagery [Miles and Barry, 1998; Willmes and Heinemann, 2016] and algorithms for processing such linear kinematic features as leads and ridges have been developed [Hutter *et al.*, 2019]. Due to their big amount of heat exchange, leads exert important role in the Arctic climate, atmosphere and ocean. It is estimated that they account for turbulent heat transfer to the atmosphere causing changes in the air temperature. But they also cause an ocean response which is the focus of this work. Indeed, openings in sea ice cover exert

important role in ventilating the ocean, releasing dense plumes of brine during the formation of new sea ice [Wettlaufer *et al.*, 1997; Barber *et al.*, 2015] causing instabilities and overturning. Current climate models have spatial and temporal resolution too coarse to simulate leads and their small scale generated turbulence instability explicitly. Thus, high resolution models can be used to investigate the small scale processes and guide toward the developing of parametrizations, which can be integrated in general climate models (GCMs).

### 1.3.3 Brine rejection phenomenon

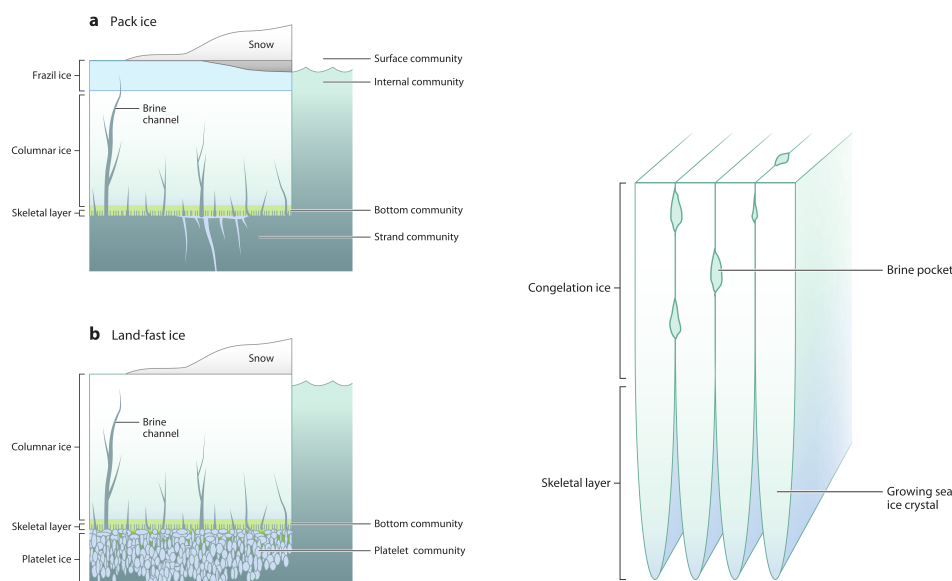


Figure 1.7: Schematic diagrams of brine channels and brine pockets in pack ice and land-fast ice (left) and their cross sections (right). Figures from *Arrigo* [2014].

New sea ice formation under cooling conditions happens with the formation of a porous matrix, a mushy layer, consisting of pure ice crystals and trapped brine pockets of high concentrated salty water.

Many laboratory experiments have been conducted to study brine rejection [Wettlaufer *et al.*, 1997]. When a binary liquid mixture, such as a solution of salt in water, is cooled, the ice grows in crystals, rejecting salty enriched liquid forming brine pockets. Brine pockets can have salinity that exceeds 150 psu. With such a high density they can overcome the resistance of the solid crystals forming brine channels downward toward the bottom of the layer. In this way, dense plumes are

rejected into the water below causing the distillation of freshwater.

Sea ice can reach a thickness of 15 cm in the first 24 hours of growth and when the thickness overcomes 20 cm the brine rejection rate is lowered. Turbulence conditions such as strong winds or currents lead to thicker layer [Arrigo, 2014]. The maximum brine flux from a single lead occurs within 6 hours of its formation [Wettlaufer *et al.*, 1997]. Although this process has a very short time scale compared to seasonal time scale, it influences the large scale circulation. In coastal polynyas brine rejection causes the cascade of dense water from the shelf into the deep sea entering the Arctic circulation. However, due to the strong stratification of the Arctic this water remains confined above 400 m [Ivanov and Golovin, 2007]. The same limitation of dense water penetration in the interior ocean happens in leads.

## 1.4 Observations in the Arctic Ocean

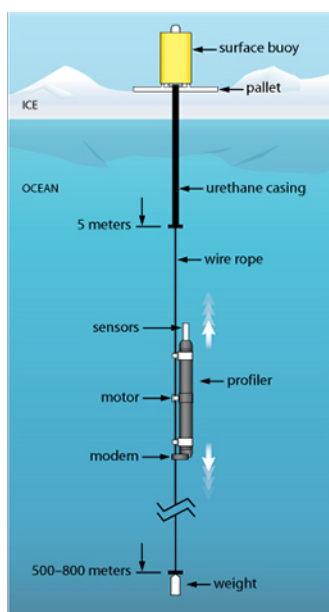


Figure 1.8: Schematic of the WHOI Ice-Tethered Profiler (ITP) system. Figure taken from *Toole et al.* [2011].

Measuring sea ice in the Arctic Ocean is possible through laser and radar altimeters, field measurements and nuclear submarine which mapped the under side of the ice for operational purposes since 1950s. However, the Arctic Ocean properties are more difficult to measure because of the presence of sea ice cover. Satellite

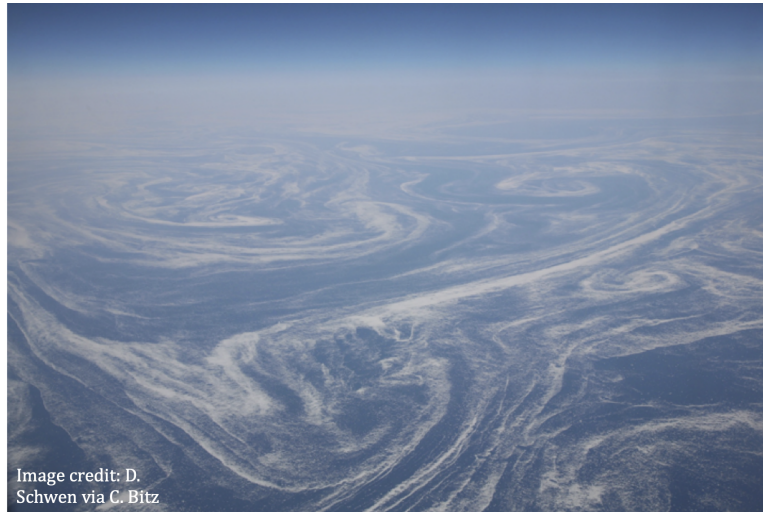


Figure 1.9: Oceanic eddies formed in the Arctic Ocean. Sea ice structures follow oceanic eddies. The image credit is to D. Schwen.

observations are limited to the boundary regions of the Arctic Ocean [IPCC, 2019] and Argo profilers can not return position information when they come at the surface. High resolution measurements are possible using moored sensors, which are located deeper than the bottom ice interface in order not to be damaged by sea ice, and using sea ice as a platform from where temperature and salinity profilers can be tethered. These profilers, known as ice-tethered profilers (ITPs), go up and down in the ocean from below the ice-ocean interface to 750-1000 m depth (Fig. 1.8). The idea of using sea ice as a platform is at the base of the Autonomous and Lagrangian Platforms and Sensors (ALPS) program [Rudnick *et al.*, eds. 2018] which coordinates an observing system of the Arctic of small portable devices set over sea ice platforms from which monitor atmospheric, snow and sea ice and ocean properties.

Like the other oceans on Earth, the Arctic Ocean is full of vortical coherent structures known as eddies. They span from small to large scales, with the larger scale eddies that are more easily detectable, such as mesoscale eddies. An image of Arctic Ocean eddies is shown in Fig. 1.9.

Arctic mesoscale eddies were first observed in the '70s [Hunkins, 1974; Wadhams *et al.*, 1979]. More recently they have been observed at all depths and in every regions in the Arctic Ocean through field campaigns [D'Asaro, 1988; Hunkins, 1974], ice-tethered profiles [Timmermans *et al.*, 2006; Zhao *et al.*, 2016, 2014], moorings [Pnyushkov *et al.*, 2018; Carpenter and Timmermans, 2012; Zhao

and Timmermans, 2015] and satellite images in ice-free surface, such as the high-resolution spaceborne synthetic aperture radar (SAR) measurements [Kozlov *et al.*, 2019]. In the Canada Basin they occupy up to 1/4 of the area of the Beaufort Sea [Manley and Hunkins, 1985] and they are located at depths between 500 m and 2000 m [Carpenter and Timmermans, 2012]. Mesoscale eddies can originate from many mechanisms, among which baroclinic instabilities of the mean flow [D’Asaro, 1988], wind driven gyres and surface fronts [Manucharyan and Timmermans, 2013].

Smaller eddies, such as submesoscale eddies, have been observed in the Arctic Ocean through drifters measurements in the Beaufort Sea [Mensa *et al.*, 2018; Timmermans *et al.*, 2012]. In the Arctic Ocean, submesoscale eddies can form due to input and output of salt that creates ice-covered regions beside open-water regions. They can form both in summertime floes melting and in wintertime leads, where brine rejection establishes strong horizontal density gradient at the ice-edges, or at marginal ice zones (MIZs). The interaction between floe size, ocean circulation and melting has been studied by Horvat *et al.* [2016]: submesoscale eddies, spreading from the floe ice-edge, mix heat horizontally and enhance sea ice melting. Submesoscale eddies energized by brine rejection are the focus of this thesis.

## 1.5 Global climate models

Governing equations for fluids are non linear equations, where the non linearity lies in the advection terms. Thus, perturbations of the mean flow imply interactions among different scales. This is clearly visible when decomposing each variable in the equations into a mean and a perturbation part ( $\phi = \bar{\phi} + \phi'$ ), so that the advection terms would give rise to the so called eddy flux terms, of the forms  $\partial/\partial x_j(\overline{\phi'_i u'_j})$  (here the Boussinesq incompressible flow approximation is made). For particularly turbulent flows, the eddy fluxes  $\overline{\phi'_i u'_j}$  are comparable to the mean fluxes, and including their effect into the mean flow becomes necessary. Indeed, rotating structures such as mesoscale and submesoscale eddies, of typical length scale of 100 km and 1 km, respectively, originate from instabilities that are enhanced and grow toward bigger scales, by subtracting the kinetic energy from the mean flow.

Coarse resolution oceanic models, with a horizontal resolution of 10 km, don’t have the resolution needed to resolve these kinds of subgridscale features and need subgridscale parametrizations or turbulent closures. Fig. 1.10 shows that submesoscale processes are not likely to be resolved for the end of the century,

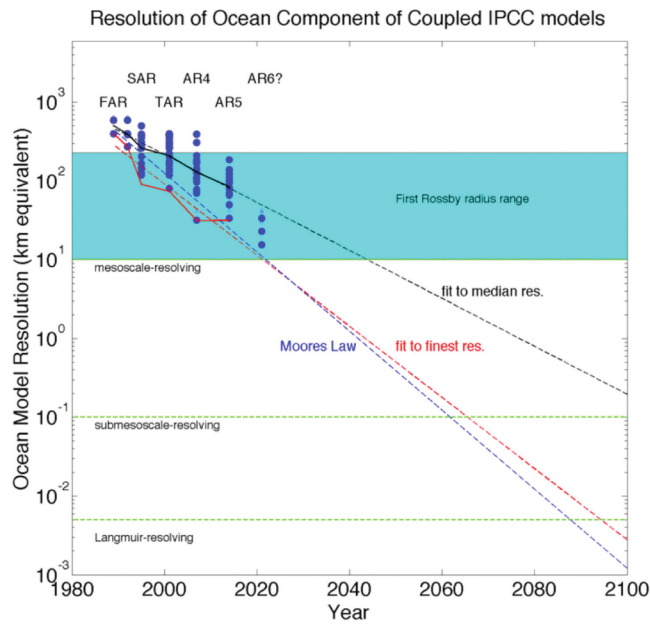


Figure 1.10: Estimate of the effective nominal horizontal resolution of ocean model components for primary baseline and climate change scenarios as reported in the IPCC reports by year of publication. Exponential fits to the median, finest-resolution, and a Moore’s (1965) law estimate are shown; the doubling of resolution occurs every 10.2, 6.9, and 6 years, respectively. From *Fox-Kemper et al.* [2014].

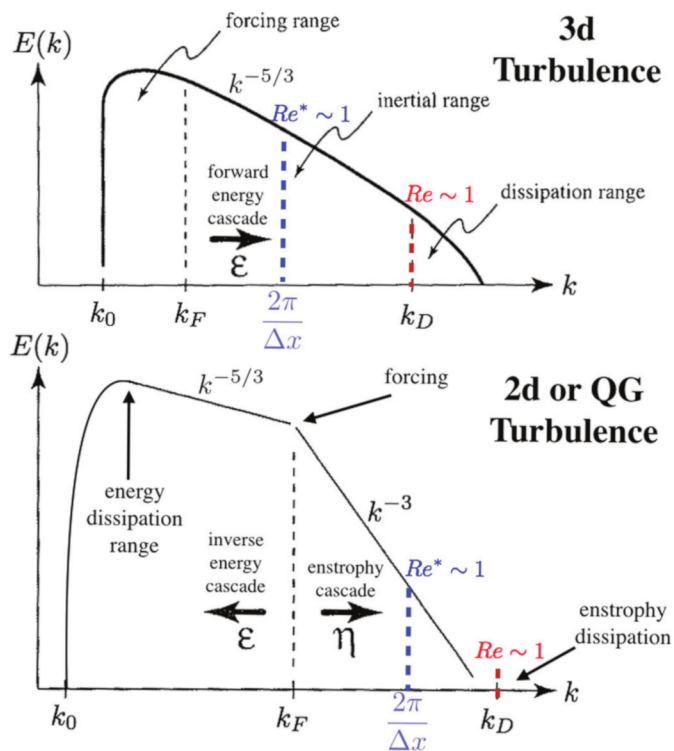


Figure 1.11: Schematic of inertial range theories for 3D turbulence and 2D turbulence. From *Fox-Kemper et al.* [2014].

and underlines the necessity of developing parametrizations. This applies also to fine resolution models and eddy-resolving models, such as large eddy simulations (LES), since they are not able to directly resolve all the scales toward the dissipation. Only direct numerical simulations (DNS) explicitly solve the non linearity in the equations, but they are computational expensive and, therefore, used only in small regional areas of the planet.

There are many ways to parametrize subgridscale motions, depending on the smaller scale resolved by the model. Usually, they are based on eddy diffusivity or eddy viscosity parametrizations, which are based on the idea of treating the turbulent fluxes as molecular diffusion or molecular viscosity. Indeed, eddies' role is to enhance molecular diffusion. This parametrization gives  $-\partial/\partial x_j(\overline{\phi'_i u'_j}) \approx K \nabla^2 \overline{\phi}$  where  $K$  is the eddy diffusivity ( $K \gg k$ , with  $k$  molecular diffusivity). An analogous form holds for the eddy momentum fluxes  $\overline{u'_i u'_j}$  with the turbulent viscosity  $\nu_t$  instead of  $K$ . In these closures theories,  $K$  and  $\nu_t$  are fixed constant.

However, usually, large eddy simulations (LES), which resolve explicitly the larger eddies and parametrize the smaller eddies, use different parametrizations to take into account just the non resolved part of the energy spectrum and the spatial variability of turbulent viscosity and diffusivity, building non linear viscosities and diffusivities based on the cascade theory for turbulence (Fig. 1.11). The first kind of this parametrization was developed by Smagorinsky in 1963 [*Smagorinsky, 1963; Fox-Kemper and Menemenlis, 2008*] and is valid for 3D turbulence, while an analogous scheme for 2D turbulence was developed by Leith in 1996 [*Fox-Kemper and Menemenlis, 2008*]. They are to be used accordingly to the turbulent cascade feature of the process resolved. Usually, the Leith viscosity is more accurate for MOLES (mesoscale ocean large eddy simulations), which have a grid resolution of 5-50 km; while the Smagorinsky viscosity can be used without introducing big errors in the SMOLES (submesoscale ocean LES), which have a grid resolution from 100 m to 1 km. In fact, although submesoscale eddies obey the turbulent inverse energy cascade typical of 2D turbulence, they usually can't reach large horizontal sizes, maintaining a more 3D isotropic structure.

Mesoscale and submesoscale eddies activities are important also in the Arctic Ocean. There, the complexity of the interactions between ocean-air-sea-ice, which is not fully understood, makes it difficult for ocean general circulation models to represent temperature and salinity profiles [*Steiner et al., 2004*]. The necessity of understanding the subgridscale processes in the Arctic leads to the development of idealized numerical models that can be helpful for developing accurate parametrizations of the small scale processes.

The importance of including Arctic Ocean submesoscale eddies effect in global climate models was first understood when *Fox-Kemper et al.* [2011] introduced a parametrization for submesoscale eddies, known as MLE parametrization, and further explained in Sec. 1.6.5. When used in global climate models (GCMs), it simulates better the global ocean mixed-layer depth. This is particularly enhanced in the Arctic Ocean where GCMs without the MLE parametrization overestimate the mixed-layer depth [*Fox-Kemper et al.*, 2011]. Mixed-layer depth modification implies a redistribution of sea ice thickness, since the surface layer heat capacity is reduced when the parametrization is used. *Horvat et al.* [2016], through idealized ocean model experiments, show that floe size and thickness distribution (FSTD) need to be included into GCMs, because the heat exchanged between open water and sea ice is not instantaneously mixed throughout the mixed-layer but fronts and eddies form. Fronts and eddies form also in wintertime leads and the use of high-resolution idealized ocean model simulations can help to understand the effects of submesoscale instability in the energy pathways. This, indeed, is the goal of this work.

Also process models, like climate models, use turbulence closures. In this work, which studies submesoscale eddies, the Smagorinsky closure is adopted.

### 1.5.1 Smagorinsky viscosity

The Smagorinsky eddy viscosity usefully represents the subgrid scale energy transfer when the gridscale lies in the energy inertial range of the energy spectrum for 3D turbulence developed by Kolmogorov, i.e. between the large scale forcing range, where the injection of energy happens, and the small scale dissipation range, where molecular viscosity dissipates energy.

The general energy equation, which can be obtained by dotting the momentum equation into the velocity, written in wavenumber space  $k$ , is given by

$$\frac{\partial \mathcal{E}(k)}{\partial t} = -\frac{\partial F_E}{\partial k} - \nu k^2 \mathcal{E}(k) + S_E(k, t) \quad (1.8)$$

where  $\mathcal{E}(k)$  is the energy per unit  $k$ ,  $F_E$  is the flux of energy between wavenumbers,  $S_E$  represents sources or sinks and the  $\nu$  term is the viscous term. For small wavenumbers (big scales) the forcing term is dominant, for big wavenumbers (small scales) the viscous dissipation is dominant. But for wavenumbers in the middle range between these two limits, known as the inertial range, these terms are negligible and only the inertial terms given by  $F_E$  is dominant. Moreover, in the steady state, (1.8) gives  $\frac{\partial F_E}{\partial k} = 0$  which establishes a constant flux rate  $\epsilon$  at

every wavenumber. Finally, Kolmogorov theory, based on dimensional analysis, estimates the energy spectrum  $\mathcal{E}(k)$  in the inertial range:

$$\mathcal{E}(k) \propto \epsilon^{-2/3} k^{-5/3} \quad (1.9)$$

establishes the forward cascade of energy, from the forcing range toward the dissipation range at the Kolmogorov wavenumber

$$k_d = \epsilon^{1/4} \nu^{-3/4} \quad (1.10)$$

which is a  $O(1 \text{ cm})$  length scale. Obviously, the dissipation length scale is bigger for bigger viscosity and for smaller energy flux.

In a DNS model, the gridscale is small enough to resolve the viscous dissipation scale, so that the energy spectrum is completely resolved. Otherwise, if the gridscale is bigger than the viscous scale, parametrizations need to be used. Smagorinsky's approach was developed for LES simulations, where big eddies are resolved, so that the gridscale wavenumber  $k_*$  is inside the inertial range. His idea is to find the spatial and time variable viscosity such that the dissipation happens at the gridscale,  $k_d \propto k_* = 2\pi/\Delta x$ :

$$\nu_* = \left(\frac{\gamma\Delta x}{\pi}\right)^2 \sqrt{\left(\frac{\partial u_*}{\partial x} - \frac{\partial v_*}{\partial y}\right)^2 + \left(\frac{\partial u_*}{\partial y} + \frac{\partial v_*}{\partial x}\right)^2} \quad (1.11)$$

written for the hydrostatic case, where  $w$  is negligible and the predominant viscosity is horizontal.  $u_*$  and  $v_*$  are the velocities at the smaller resolved scale. The eddy viscosity in the Smagorinsky scheme is adjusted at every time scale for every grid cell given the smallest resolved flow and  $\epsilon$ .

Smagorinsky, also, supposes that eddies diffuse momentum and tracers at the same rate, and uses the same eddy viscosity for both viscosity and diffusivity.

The implementation of the Smagorinsky viscosity will be further discussed in Sec. 2.1.5. Here it is important to notice that the fact that the Smagorinsky viscosity is only used for the horizontal momentum closure is limiting the bias introduced when treating the submesoscale turbulence as a 3D forward energy cascading turbulence.

## 1.6 Submesoscale eddies

Oceanic eddies, such as mesoscale and submesoscale eddies, are key features of the Arctic Ocean, transporting water masses and properties, such as salt, nutrients, contaminants, heat and momentum, and thus affecting the large scale flow

and the biogeochemical cycles including phytoplankton blooms.

Submesoscale eddies, which are the focus of this work, develop at the surface oceanic mixed-layer, as will be seen in Sec. 1.6.1, and are mainly formed near oceanic fronts. Indeed, they drive restratification of the mixed-layer, as will be seen in Sec. 1.6.2. This process is particularly active in mid-latitude oceans, but it is expected to be important also in polar regions [*Fox-Kemper et al.*, 2011], where submesoscale eddies can impact sea ice, primary production, lateral transport of properties and the upper ocean heat budget.

The ocean mixed-layer (ML) is the surface upper ocean layer in contact with the atmosphere. It is usually well mixed in the vertical, with a small stratification, but not always well mixed in the horizontal direction, since there could be horizontal density gradients. The vertical mixing of the mixed layer is established by mixing and stirring processes in the ocean which compete with restratification processes. Mixing is caused by convection (due to heat or salt fluxes from the atmosphere to the ocean, such as warming or, at high latitudes, freshening) and shear mechanisms. Restratification is due to gravitational overturning and submesoscale eddies. The spatially variable ocean-atmosphere fluxes create fronts in the ocean surface layer characterized by vertical isopycnals and strong horizontal density gradients. Gravity slumps the vertical isopycnals and more lighter water sits above denser water increasing the stratification of the mixed layer. However, the Earth rotation limits the frontal slumping establishing a balance between geostrophy and gravity, the so called geostrophic adjustment [*Tandon and Garrett*, 1994, 1995], which leaves the isopycnals tilted, as will be seen in Sec. 1.6.3. This front, finally, can be baroclinically unstable and give rise to submesoscale eddies which move properties laterally and tend to restratify the fluid [*Boccaletti et al.*, 2007; *Fox-Kemper et al.*, 2008]. The complex process by which the initially vertical front tilts is known as frontal spin-down process, and it will be studied deeply in Sec. 1.6.2. Due to this complex balance between mixing and restratification processes, the mixed-layer undergoes a seasonal cycle, deepening when mixing is dominant and getting shallower when stratification is more important.

### 1.6.1 Mesoscale and submesoscale baroclinic instability

Mesoscale and submesoscale eddies originate from baroclinic instabilities that can develop from the release of available potential energy in the ocean interior and in the ocean mixed-layer respectively.

Perturbations of the mean flow in certain conditions of stably stratified rotating fluids can give rise to baroclinic instability, which converts the potential energy

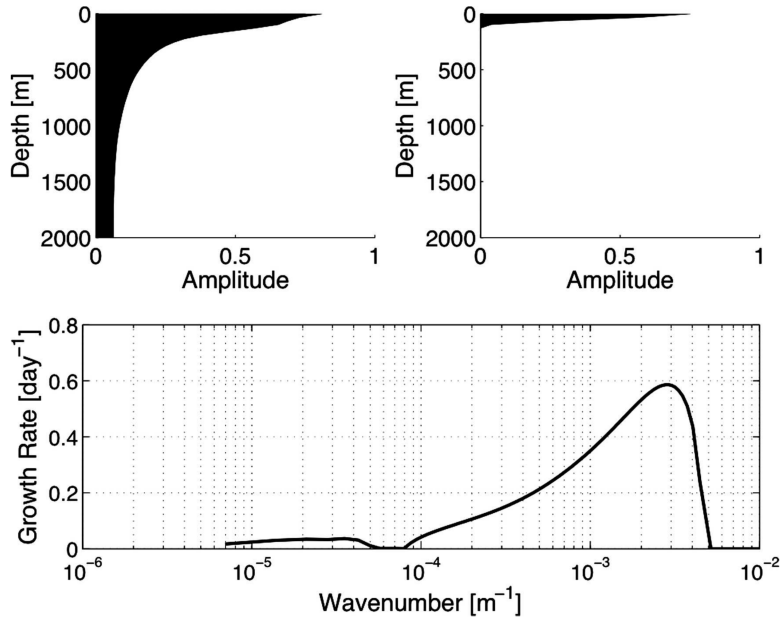


Figure 1.12: Oceanic baroclinic instability modes separation into mesoscale and submesoscale (bottom) and their respective vertical distributions (top), from measurements of North Pacific Ocean. Figure from *Boccaletti et al.* [2007].

stored in the tilted isopycnals into kinetic energy of the perturbation. Baroclinic instability differs from barotropic instability, in which the absence of the Earth rotation leaves the isopycnals flat and, due to shear in the horizontal flow, perturbation can grow as gravity waves. Instead, baroclinic instability naturally emerges in rotating fluids, where, due to the thermal wind relation

$$\frac{\partial b}{\partial y} = -f \frac{\partial u}{\partial z} \quad (1.12)$$

isopycnals are tilted and store potential energy. For initial times the perturbation has small amplitudes and can be treated linearly with the instability theory. However, soon, turbulence is enhanced from growing and interacting modes, for the non-linear nature of fluid motions, and vortical coherent structures like eddies can form at later times.

Mesoscale and submesoscale eddies differ for their size and their growth rate. Their differences are noticeable through the quasi-geostrophic (QG) stability analysis on a background state [*Boccaletti et al.*, 2007]: two separate classes of baroclinic instabilities appear (Fig. 1.12), one generating the mesoscale eddy field and one generating a smaller and faster mode, known as submesoscale. The mesoscale

affects the entire depth of the ocean, with horizontal size of the order of 100 km and a time scale of the order of 1 month; the submesoscale affects a shallow region of the ocean, the surface mixed-layer, with smaller size of the order of 1 km and a short time scale of about 1 day.

Due to their length scale, mesoscale and submesoscale have different Rossby numbers. The Rossby number expresses the ratio between the inertial force or the rate of change of momentum and the Coriolis force

$$Ro = \frac{U}{fL} \quad (1.13)$$

where  $f$  is the Coriolis parameter, which is related to the Earth rotation period through  $T_{rot} = 2\pi/f$ .  $f^{-1}$  is called the inertial timescale, which is about 3 hours at mid-latitudes and 2 hours at 80 °N.  $Ro$  is small if the relative motion of the flow considered is slower than the Earth rotation, or, equivalently, if the characteristic horizontal length scale of motion is large compared to the distance traveled by a parcel at velocity  $U$  in a rotational period  $T_{rot}$ . In other words,  $Ro$  is small if the Earth rotation governs the motion of the fluid.

At the mesoscale, the large scale makes  $Ro \ll 1$ , and the quasi-geostrophic theory is valid. At the submesoscale, instead, due to the small mixed-layer vertical depth in which submesoscale eddies develop, the Rossby number is bigger  $Ro \sim 1$  and the flow deviates from the quasi-geostrophic theory with an important ageostrophic component. For this reason, the mesoscale is also called geostrophic baroclinic instability and the submesoscale ageostrophic baroclinic instability.

Another important dimensionless parameter can be introduced to express the ratio between vertical stratification and vertical shear, i.e. mixing: the bulk Richardson number

$$Ri = \frac{\frac{\partial b}{\partial z}}{\left|\frac{\partial \mathbf{u}}{\partial z}\right|^2} = \frac{N^2}{\left|\frac{\partial \mathbf{u}}{\partial z}\right|^2} = \frac{N^2 H^2}{U^2} \quad (1.14)$$

where  $H$  is the length scale of vertical motion and

$$N^2 = \frac{\partial b}{\partial z} \quad (1.15)$$

is the frequency at which a parcel would oscillate when subjects to a vertical displacement, and expresses the stratification of the water. For strongly stratified fluid, such as the ocean interior,  $Ri \gg 1$ ; for weakly stratified fluid, such as the oceanic mixed-layer,  $Ri \sim 1$ .

In the baroclinic instability theory Rossby number and Richardson number are related one each other through the deformation radius

$$L_d = \frac{NH}{f} \quad (1.16)$$

which is, as will be seen in Sec. 1.6.3, the natural instability length scale. Posing  $L \sim L_d$  it follows  $NH/fL \sim 1$  and

$$Ro^2 Ri \sim 1 \quad (1.17)$$

Thus, for the strongly stratified ocean interior, (1.17) confirms  $Ro \ll 1$ , with a time scale bigger than the rotational period  $T \gg f^{-1}$ , and a bigger length scale  $L \gg U/f$ . For the weakly stratified ocean mixed-layer, both  $Ro$  and  $Ri$  are order 1, and the typical time scale and length scale are faster and smaller, respectively:  $T \sim f^{-1}$  and  $L \sim U/f$ . Table 1.1 summaries the main features of mesoscale and submesoscale.

Mesoscale	Submesoscale
deep (entire depth)	shallow (mixed-layer)
$L = 100$ km	$L = 1$ km
$\tau = 1$ month	$\tau = 1$ day
$O(1 \text{ month}^{-1})$ short growth rate	$O(1 \text{ day}^{-1})$ fast growth rate
$Ro \ll 1$	$Ro = O(1)$
$Ri \gg 1$	$Ri = O(1)$
geostrophic baroclinic instability	ageostrophic baroclinic instability

Table 1.1: Mesoscale and submesoscale baroclinic instabilities features.

Mesoscale eddies impact the ocean interior through diapycnal mixing and lateral transport, being an important link between the ocean basin boundaries and the ocean interior. Submesoscale eddies, also called mixed-layer eddies (MLEs) [Fox-Kemper *et al.*, 2008], are energized by frontal slumping and play an important role in determining the ocean surface layer properties. Mesoscale and submesoscale eddies are connected one each other: MLEs emerge naturally from mesoscale eddies by a downscale transfer of energy. Simulations allowing the development of mesoscale and submesoscale eddies show that mesoscale and submesoscale eddies have comparable horizontal velocities but, due to the ageostrophic nature of submesoscale eddies, MLEs have important vertical velocity [Fox-Kemper *et al.*, 2008]. From that, vertical and horizontal eddy buoyancy fluxes have different magnitude in mesoscale and submesoscale:

- $w'b'$ : only MLEs have big  $Ro$  and, thus, vertical velocity;
- $u'b', v'b'$ : from mixing length theory bigger horizontal transport corresponds to bigger eddies.

To sum up, while horizontal fluxes are due to the mesoscale eddy field, vertical fluxes are typical fluxes of submesoscale eddies. Moreover,  $\overline{w'b'} > 0$ , indicating a tendency to restratify the mixed-layer.

### 1.6.2 Mixed-layer eddies in the frontal spin-down problem

Fronts can be defined as large density (or other tracers) gradient in one horizontal direction and weak gradients in the perpendicular horizontal direction [McWilliams, 2021]. They are common in the ocean, especially at the surface, the bottom and near the shore, with horizontal widths from meters to kilometers. Most of the oceanic fronts are transient events with their own life time. Oceanic surface fronts play important roles in the energy pathways between ocean scales, giving rise, during the frontogenesis process, to an ageostrophic overturning circulation in the across-front direction and instabilities which spread laterally water properties through small scale coherent vortical structures.

Submesoscale baroclinic instabilities are a typical instability that develops at an oceanic surface front in the along-front direction. They can grow in a quiescent front where lateral density gradients are formed through surface fluxes or mesoscale straining. Once a front is formed, gravity starts to slump it, leading to restratification, and reducing the potential energy to the minimum value. However, the Earth rotation constraints the restratification process through the geostrophic adjustment process. Baroclinic instabilities can, then, develop and sustain an ageostrophic flow that enhances submesoscale eddies. Submesoscale eddy size grows in time, reaching rapidly finite amplitude and spreading away as the isopycnals tilt further. Indeed, they extract the potential energy stored in the front by further slumping the front. Submesoscale eddies, due to their vertical velocity, move up and down along isopycnals, and, as the front falls, they can move horizontally, spreading easily laterally away and increasing their horizontal size. This can happen until a mixing forcing appears. Indeed, the presence of a diurnal cycle prevents the eddies to become bigger and bigger and propagate laterally. However, due to their rapid growth time scale compared to mesoscale, submesoscale eddies are efficiently to restratify the ML between mixing events. Submesoscale eddies are the main drivers of ML restratification [Boccaletti *et al.*, 2007].

The frontal spindown problem has been long studied. First, *Csanady* [1982], *Ou* [1984], *Tandon and Garrett* [1994, 1995] studied the geostrophic adjustment process (Sec. 1.6.3); secondarily *Boccaletti et al.* [2007] introduced the effects of baroclinic instability; finally, *Fox-Kemper et al.* [2008] developed a parametrization for the restratification driven by finite-amplitude baroclinic instabilities of the ML (MLEs) in terms of an overturning streamfunction that tilts the isopycnals, based on the phenomenology of the MLEs (Sec. 1.6.4 and 1.6.5).

### 1.6.3 Geostrophic adjustment

Geostrophic adjustment is the process by which an initial anomaly in the pressure field adjusts to a geostrophic balance state in a rotating fluid.

In a rotating fluid, the initial anomaly splits into a geostrophic part and an ageostrophic part. The ageostrophic flow is rapidly propagated away as a gravity wave, leaving behind only the geostrophic adjusted state. It is the presence of the Earth rotation that allows this process to exist in the ocean. With no rotation, in fact, all the initial perturbation propagates away at the gravity wave speed  $\sqrt{gH}$ , leaving no pressure gradients inside the domain of study. For rotating fluids, part of this pressure field balances with the Coriolis force, creating a geostrophic adjusted state. In simple cases in which potential vorticity is conserved, that is inviscid and adiabatic flow, the final steady state solution is easily found [Vallis, 2006]. A natural length scale appears in the problem, the Rossby radius of deformation

$$L_d = \frac{\sqrt{gH}}{f} \quad (1.18)$$

which sets the distance by which the flow is in geostrophic balance. The geostrophic adjustment appears when the length scale of the initial anomaly is larger than the deformation radius; or, equivalently, when the frequency of the anomaly is slower than the rotational frequency  $f$ . Indeed, in order to have geostrophic balance the Rossby number  $Ro = U/(fL)$  should be small.

An example of geostrophic adjustment is in the presence of oceanic fronts [Csanady, 1982]. A front, with its horizontal density gradient, creates a pressure gradient force, which forces the fluid to move in the along density gradient direction, developing two opposite velocities at the surface and at the base, acting to slump the front and converting potential energy into kinetic energy. If rotation is important, a transverse circulation develops, with velocities in the perpendicular direction, i.e. along the front. Again, they are opposite at the surface and at the bottom. The equilibrium state is reached when the across front velocity stops and the left velocity is in the perpendicular direction. Thus, the difference between

non rotating and rotating fluids is that only in rotating fluids the front is not completely flattened but the isopycnals are tilted in order to be in geostrophic balance.

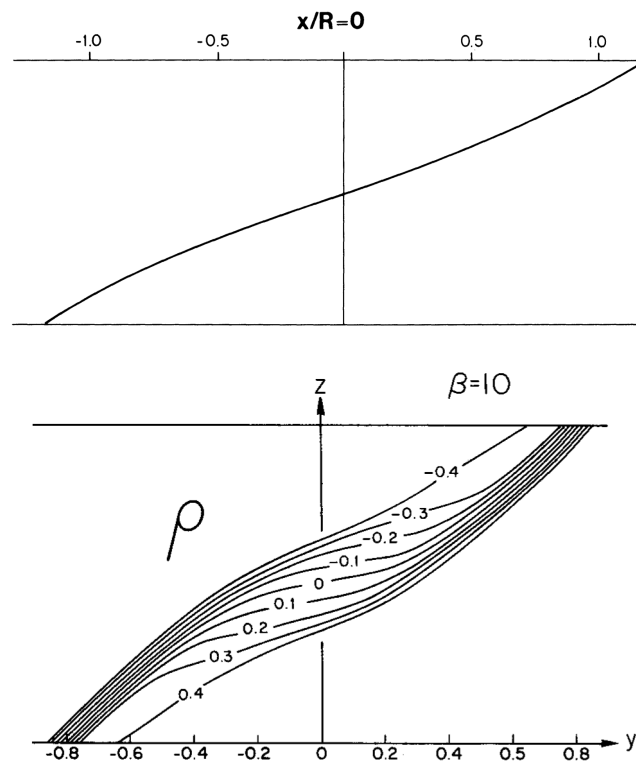


Figure 1.13: On the top: density interface shape after geostrophic adjustment in Csanady study [Csanady, 1982]. On the bottom: realistic visualization of density field in the model developed by Ou [1984].

Fig. 1.13 on the top shows the geostrophically balanced interface in the two layers study by Csanady [1982]. The S-shaped interface becomes more complex when continuous stratification is used [Ou, 1984], with density gradients greatest near the top and the bottom and smaller inside, with isopycnals flattened (bottom figure in Fig. 1.13). Tandon and Garrett [1994, 1995] study the restratification of the mixed-layer due to horizontal density gradients and find a scaling for the stratification  $N^2$ , introducing the equivalent of the vertical stratification in the horizontal across front direction

$$M^2 = \frac{\partial b}{\partial y} \quad (1.19)$$

where the front is considered along the x-direction so that the buoyancy gradient is in the y-direction, and using the relations between Rossby and Richardson numbers

in (1.17) with  $Ro$  and  $Ri$  values as in the mixed-layer,  $\sim 1$ .  $M^2/N^2$  is scaled as  $H/L$  and, finally, the new restratification due to geostrophic adjustment is

$$N^2 = \frac{M^4}{f^2} \quad (1.20)$$

Since the geostrophic adjustment timescale is the inertial timescale  $f^{-1}$ , it can appear between two mixing events with typical timescale  $\tau > f^{-1}$ , such as the diurnal cycle or less frequent storms. Mesoscale instabilities can not develop between two mixing events because of their bigger time scale  $T \gg \tau > f^{-1}$ , while submesoscale instabilities have smaller time scale such that  $\tau > T \approx f^{-1}$ . It is therefore important to consider also the restratification effects of MLEs beyond geostrophic adjustment.

#### 1.6.4 Mixed-layer eddy phenomenology

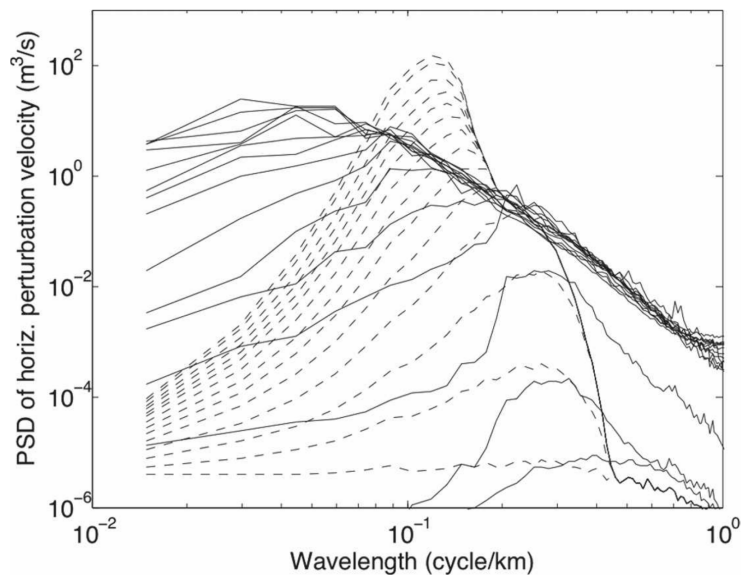


Figure 1.14: Simulated (solid lines) EKE power spectral density at 2-day intervals compared with the linear theory prediction (dashed lines). For increasing times the spectrum deviates from the linear theory establishing a turbulent inverse energy cascade toward larger scales. Figure taken from *Fox-Kemper et al.* [2008].

Simulations of frontal slump [*Fox-Kemper et al.*, 2008] show that the flow reaches finite amplitude instabilities in few days, passing by inertial oscillations

about the Rossby adjusted state at earlier times if not already in thermal wind balance. In real oceans however the finite amplitude is reached even earlier [Boccaletti *et al.*, 2007].

The frontal spindown problem goes beyond the linear theory, which is useful to describe the initial behaviour of the instability development and sets the important length scales involved and the growth rate. After few days, when the instability reaches finite amplitude, eddies merge and transfer energy to larger scales following the inverse energy cascade, as visible in the power density spectrum of eddy kinetic energy (EKE), Fig. 1.14: for initial times the kinetic energy spectrum is centered about high wavenumbers, corresponding to small length scale,  $l = 2\pi/k$ , with a clear peak meaning that the different instability modes do not exchange energy and the linear theory of non interacting modes applies well; over times, the kinetic energy spectrum shifts toward bigger scales and, at the same time, deviates from the linear theory, assuming the familiar slope of two-dimensional turbulence spectrum characterized by inverse energy cascade from the smaller scales toward the bigger scales. Indeed, when submesoscale eddies can become larger and larger, they assume the typical elongated structure of two-dimensional turbulence, since their vertical length scale is constrained by the ML depth but no such a constraint exists in the horizontal direction. Thus, submesoscale eddies can grow indefinitely, at least if no more mixing opposes.

MLEs vary in size according to the strength of the front. The vertical excursion scale  $\zeta = \frac{\sqrt{b'^2}}{N^2}$  is a measure of how much eddies mix up and down in the vertical. Simulations show that it saturates at  $\zeta \approx 0.2H$  when finite amplitude is reached [Fox-Kemper *et al.*, 2008].

The frontal slump happens without spreading much:  $M^2$  decreases only 10% to 20% while  $N^2$  increases by orders of magnitude. It has already been said that vertical eddy buoyancy fluxes arise in submesoscale eddies with  $\overline{w'b'} > 0$  in order to extract the potential energy stored in the front. Simulations show that the eddy buoyancy flux direction is more horizontal than the isopycnal slope [Fox-Kemper *et al.*, 2008]: at finite amplitude, eddy buoyancy fluxes slope is  $\approx 1/2$  of the frontal slope.

Simulations show also that the EKE grows exponentially during the linear phase and then saturates at the initial value of the mean geostrophic kinetic energy of the front, when looking only at the average over the center of the front, while it continues to grow, when looking at the basin average beyond the initial frontal width.

### 1.6.5 Mixed-layer eddy parametrization

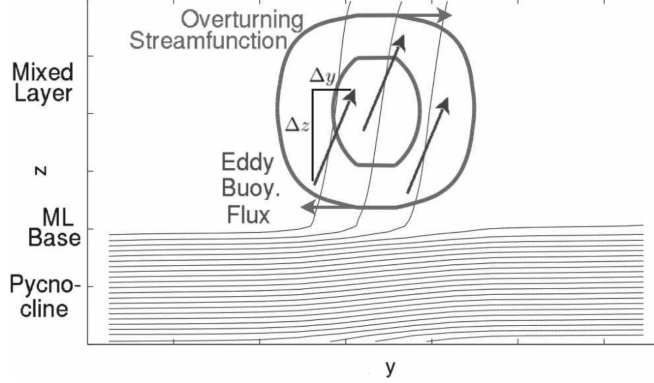


Figure 1.15: Schematic of the ML restratification. Straight arrows represent eddy buoyancy fluxes, while circular arrows indicate the overturning streamfunction. Figure from *Fox-Kemper et al.* [2008].

The MLE parametrization theory for the ML restratification [*Fox-Kemper et al.*, 2008] is very similar to the Gent and McWilliams (GM) parametrization [*Gent and McWilliams*, 1990; *Gent et al.*, 1995] for the mesoscale restratification. Indeed, both processes originate from baroclinic instabilities that subtract potential energy stored in the tilted isopycnals, and the eddy-induced advective velocities can be represented in terms of an overturning streamfunction. Only buoyancy fluxes need to be parametrized, since momentum fluxes are negligible compared to the Coriolis force. However, differences are due to the vertical size, which is fixed by the mixed-layer depth in MLEs, and the fact that  $N^2$  is smaller in sub-mesoscale, where, in general,  $N^2$  and  $M^2$  are uniform in depth in the ML.

Thus, key parameters in the MLEs problem are the ML depth, the strength of the front (i.e.  $\nabla_H \bar{b}$ ), the Coriolis parameter  $f$ ; while not important parameters are the stratification  $N^2$  and the width of basin, at least for short times so that the eddies do not affect the boundaries.

The parametrization is built from the relation between the variation of the potential energy and the increased vertical eddy buoyancy flux  $\overline{w'b'}$ . Using the phenomenology aspects of the MLEs it is possible to parametrize the eddy fluxes with the horizontal buoyancy gradient. Finally, an overturning streamfunction

$$\Psi \propto \frac{H^2}{|f|} \nabla \bar{b} \times \hat{z} \quad (1.21)$$

that tilts the isopycnals, with its related Bolus velocity

$$\mathbf{u}^* = \nabla \times \Psi \quad (1.22)$$

parametrizes the eddy buoyancy fluxes, and thus the potential energy extraction,

$$\overline{\mathbf{u}'b'} \equiv \Psi \times \nabla \bar{b} \quad (1.23)$$

or equivalently

$$\begin{aligned} \overline{v'b'} &= -\Psi \bar{b}_z \\ \overline{w'b'} &= \Psi \bar{b}_y \end{aligned} \quad (1.24)$$

where the indices stand for partial derivative in the given direction. The full parametrization is derived in Appendix A.

Due to the increase effect of restratification when the MLE parametrization is used, without the implementation of the MLE parametrization GCMs simulations give deep ML bias. This bias is largest in polar winter regions: sea ice is sensitive to the MLE parametrization [Fox-Kemper *et al.*, 2011].

## 1.7 Previous studies in the Arctic

Refreezing Arctic Ocean leads have been studied using both laboratory experiments and high resolution numerical model simulations, in order to capture the eddy variability. The eddy behaviour has been observed in the experimental tank of rotating fluid by *Bush and Woods* [1999, 2000]. Both sea ice dynamics and thermodynamics have been coupled to ocean dynamics in numerical models in order to study brine rejection.

A remarkable study has been conducted by *Matsumura and Hasumi* [2008]. They setup different numerical experiments in order to perform sensitivity analysis to different parameters such as air temperature, rotational effects, mixed-layer depth, strength of the halocline, width of the lead and time duration of the lead's opening. They treat the ice cover as an ideal insulator, and set to zero the brine rejection under sea ice. They artificially close the opening after a fixed time, so that there is no salt flux for long time scales. They show the frontal formation and eddy generation from baroclinic instability. Anticyclonic eddies are located at the base of the mixed-layer. Finally, they suggest a scaling for the triangular form of dense water intrusion at the base of the mixed-layer, starting from the geostrophic adjustment natural length scale, the deformation radius  $L_d$  (Fig. 1.16):

$$L_d = \frac{NH}{f} \approx \frac{\sqrt{\Delta b H}}{f} \quad (1.25)$$

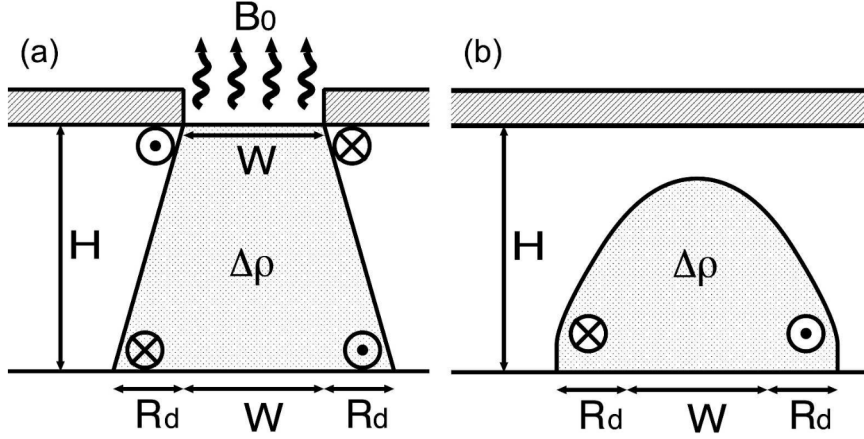


Figure 1.16: Schematic view of refreezing lead in *Matsumura and Hasumi* [2008].

where the approximation is valid in the limit in which the buoyancy in the two regions of the front is homogeneous. In fact, in the vertical buoyancy gradient  $\partial_z b = \Delta b/H$ ,  $\Delta b$  is the difference of buoyancy in the two regions of the front, which, in case of homogeneity, is the same if computed horizontally. Indeed, the deformation radius is fixed by the injection of negative buoyancy in the open ocean area, which creates the geostrophically adjusted front.

The negative buoyancy injection at the opening's surface is equal to the total buoyancy change in the domain:

$$WB_0 t_s = (W + L_d)H\Delta b = (W + L_d)L_d^2 f^2 \quad (1.26)$$

where  $W$  is the width of the lead,  $B_0$  is the buoyancy flux ( $\text{m}^2\text{s}^{-3}$ ), and  $t_s$  the opening time. Dependently on the characteristics of the configuration,  $L_d$  can be bigger or smaller than  $W$  and three solutions are possible:

$$L_d = \frac{\sqrt{B_0 t_s}}{f} \quad \text{if } L_d \ll W \quad (1.27)$$

$$L_d = \left(\frac{WB_0 t_s}{f^2}\right)^{1/3} \quad \text{if } L_d \gg W \quad (1.28)$$

$$L_d = \frac{\sqrt{B_0 t_s}}{f\sqrt{2}} = \left(\frac{WB_0 t_s}{2f^2}\right)^{1/3} \quad \text{if } L_d \sim W \quad (1.29)$$

The deformation radius expresses the lateral buoyancy transfer under geostrophic adjustment and it should evolve in time as proportional to  $t_s^{1/2}$  or  $t_s^{1/3}$ .

Here, it is important to notice that they are not suggesting a scaling for the intrusion of dense water at the base of the mixed-layer for the eddy formation case. Indeed, the deformation radius appears as natural scale in geostrophic adjustment problems. Submesoscale eddies drive ageostrophic currents and deviates from the prediction for classical geostrophic adjustment.

From the deformation radius the size of submesoscale eddies can be obtained. Many studies suggest scaling for the radius of eddies over time. Here, since this work is not interested in providing methods and measurements of eddy sizes, these scaling are not shown.

The non-hydrostatic effects of convection under the lead has been studied by [*Smith IV and Morison, 1998*]. They perform two-dimensional non-hydrostatic simulations and find that non-hydrostatic effects are dominant for depths below 100 meters, which is almost never realized in the Arctic Ocean, due to the presence of the strong halocline. They conclude that the dynamics of the realistic Arctic Ocean under brine rejection is mainly hydrostatic.

## 1.8 Motivations and objectives

The work presented in this thesis is motivated by the lack of deep understanding of the realistic oceanic response to a brine-driven Arctic Ocean refreezing lead, and aims to build powerful diagnostics tools to be used in the forthcoming more complex studies leading toward the development of a parametrization.

Addressed questions are: does the typical length of lateral density transfer scale with the deformation radius proposed by *Matsumura and Hasumi* [2008]? and, does the system reach equilibrium state with a saturated kinetic energy value?

Previous idealized numerical studies focus on the eddy size time evolution and the effect of brine rejection in the mixed-layer depth, proposing a scaling for the eddy size and for the deformation radius. In doing so, *Matsumura and Hasumi* [2008] treat sea ice as an ideal insulator, posing to zero the heat fluxes between the atmosphere and the ice-covered-ocean, which is not undergoing brine rejection. They are supposing initial equilibrium condition between sea ice, ocean and atmosphere with zero fluxes. Moreover, they artificially close the lead in order to study the spatial distribution of buoyancy and understanding the long-term effects on the halocline strength.

This thesis proposes to understand the diagnostics of the restratification mech-

anism driven by realistic heat fluxes at a single refreezing sea ice edge, intended as one large-width lead edge. In particular, single restratifying processes, such as classical gravitational overturning, geostrophic adjustment and mixed-layer eddies (MLEs), are studied separately. Then, the importance of the external forcing is investigated in order to find a relationship between air temperature and rate of change of restratification. Furthermore, new diagnostics tools such as the overturning streamfunction, will be used. Finally, the whole study is carried out separating the flow into mean and eddy energy components.

The choice of developing, first, a single ice-edge system allows to study the strength of the lateral spread of MLEs over time and will be of help in future studies of lead, intended as two interacting sea ice edges that undergo opposite slumping and generate currents in opposite directions. The ocean response regime will be determined by the ratio between the width of the lead and the mixed-layer depth, which enters also the deformation radius. This work, therefore, is intended to be at the basis of the development of a parametrization for refreezing leads.

# Chapter 2

## Numerical model configuration and Diagnostics

In this work, the Massachusetts Institute of Technology general circulation model (MITgcm) [*Marshall et al.*, 1997] in the hydrostatic form with the thermodynamic sea ice package is used for investigating the oceanic response to the forcing at the winter sea ice edge.

The MITgcm model is suited to model a wide range of phenomena, from the small scale of meters to the large global scale phenomena. It has been widely used in idealized configurations for studying the effect of mesoscale and submesoscale interactions [*Boccaletti et al.*, 2007; *Fox-Kemper et al.*, 2008] and the eddy formation in the Arctic Ocean [*Horvat et al.*, 2016; *Horvat and Tziperman*, 2018; *Manucharyan and Timmermans*, 2013; *Mensa and Timmermans*, 2017]. Baroclinic instabilities and ocean eddies can be, in fact, directly resolved by high-resolution MITgcm model simulations.

In this chapter, the numerical model characteristics are presented in Sec. 2.1 together with the thermodynamic sea ice package and the Smagorinsky eddy viscosity setup. Numerical model configurations used in this work are presented in Sec. 2.2. Finally, diagnostics tools and functions that will be used in Chapter 3 are defined in Sec. 2.3.

### 2.1 MITgcm model

The Massachusetts Institute of Technology general circulation model (MITgcm) [*Marshall et al.*, 1997] is the ocean model used in this work.

It has a single dynamical kernel that can drive forward either oceanic or atmospheric simulations, using the z-p isomorphism. This is made possible by interpreting the generic vertical coordinate  $r$  as pressure  $p$  when modeling the atmosphere and as height  $z$  when modeling the ocean.

In general, the MITgcm model solves the Navier-Stokes equations in the Boussinesq approximation, using the finite volume techniques and the Arakawa C grid discretization. It can be hydrostatic or non-hydrostatic dependently on the desired dynamics one wants to study. In this work, the hydrostatic version is used.

The model is equipped by a set of packages that can be set to run a variety of simulations. Among them, parametrizations of subgrid scale variability, such as GM parametrization [*Gent and McWilliams, 1990; Gent et al., 1995*], are implemented.

The state of the fluid at any time is characterized by the distribution of the velocity field  $\mathbf{v}$ , the potential temperature  $\theta$ , the salinity (or specific humidity for the atmosphere)  $S$ , the pressure potential (or geopotential for the atmosphere) field  $\phi$  and the density  $\rho = \rho(\theta, S, p)$ . The Boussinesq equations that govern the evolution of these fields are:

$$\begin{aligned}
\frac{D\mathbf{v}_h}{Dt} + (2\boldsymbol{\Omega} \times \mathbf{v})_h + \nabla_h \phi &= \mathcal{F}_h \\
\frac{D\dot{r}}{Dt} + \hat{\mathbf{k}} \cdot (2\boldsymbol{\Omega} \times \mathbf{v}) + \frac{\partial \phi}{\partial r} - b &= \mathcal{F}_v \\
\nabla_h \cdot \mathbf{v}_h + \frac{\partial \dot{r}}{\partial r} &= 0 \\
b &= b(\theta, S, r) \\
\frac{D\theta}{Dt} &= \mathcal{Q}_\theta \\
\frac{DS}{Dt} &= \mathcal{Q}_S
\end{aligned} \tag{2.1}$$

where  $\mathcal{F}_h$  and  $\mathcal{F}_v$  and  $\mathcal{Q}_\theta$  and  $\mathcal{Q}_S$  are forcing and dissipation terms in the horizontal and vertical momentum equations and tracers equations, respectively, set by the forcing packages in the model.

For the ocean  $r = z$ ,  $\dot{r} = \frac{Dz}{Dt} = w$  is the vertical velocity,  $\phi = p/\rho_c$  is the pressure potential, with  $\rho_c$  fixed reference density of water, and  $b(\theta, S, z) = -g \frac{\rho(\theta, S, z) - \rho_c}{\rho_c}$  is the buoyancy. The general set of equations for the ocean in the tangent-plane

Boussinesq approximation written in z-coordinates are:

$$\begin{aligned}
\frac{D\mathbf{v}_h}{Dt} + f\hat{\mathbf{k}} \times \mathbf{v}_h + \nabla_h \phi' &= \mathcal{F}_h \\
\epsilon_{nh} \frac{Dw}{Dt} + \frac{\partial \phi'}{\partial z} + g \frac{\rho'}{\rho_0} &= \epsilon_{nh} \mathcal{F}_v \\
\nabla_h \cdot \mathbf{v}_h + \frac{\partial w}{\partial z} &= 0 \\
\rho' &= \rho - \rho_0 \\
\frac{D\theta}{Dt} &= \mathcal{Q}_\theta \\
\frac{DS}{Dt} &= \mathcal{Q}_S
\end{aligned} \tag{2.2}$$

with boundary conditions

$$\begin{aligned}
w = 0 \quad \text{at} \quad z = -H(x, y) \quad \text{ocean bottom} \\
w = \frac{D\eta}{Dt} \quad \text{at} \quad z = \eta \quad \text{ocean surface}
\end{aligned} \tag{2.3}$$

with  $\eta$  displacement of the free surface and  $\epsilon_{nh}$  non-hydrostatic parameter, set to 0 in the hydrostatic form and 1 in the non-hydrostatic form. Note that the Boussinesq equations (2.2) are written for the perturbation fields, indicated with a prime, and also called anomalies from the reference resting fluid or simply anomalies. These equations are obtained by subtracting from the general equations the equations for the reference state. In fact, the density is split into  $\rho = \rho_0 + \rho'$  with  $\rho_0 = \rho_c$  the reference constant density of water equal to  $999.8 \text{ kg m}^{-3}$ , so that

$$b = -g \frac{\rho'}{\rho_0} = -g \frac{\rho - \rho_0}{\rho_0} \tag{2.4}$$

is the buoyancy written in terms of the density anomaly  $\rho'$ . The basic state has  $\rho_0$  constant and zeros velocities. Thus, the velocity field is written as  $\mathbf{v} = \mathbf{v}_0 + \mathbf{v}' = \mathbf{v}'$  and the prime has been dropped.

Once the output files are generated, the state variables and other diagnostics variables are written in NetCDF (Network Common Data Form) files. NetCDF is a self-describing scientific data format, with metadata that describe each data array, so that variables, dimensions and attributes are given. They can be accessed to through many different utilities, browsers or software, such as the ncdump utility to read NetCDF binaries data into ASCIItext files, the nview visual browser to quickly visualize and plot NetCDF data, and MATLAB.

### 2.1.1 Hydrostatic form

The MITgcm model can be hydrostatic, quasi-hydrostatic, quasi-nonhydrostatic and non-hydrostatic. First, the pressure potential is separated into a surface pressure potential  $\phi_s(x, y)$ , a hydrostatic part  $\phi_{hyd}(x, y, r)$  and a non-hydrostatic term  $\phi_{nh}(x, y, r)$ :

$$\phi(x, y, r) = \phi_s(x, y) + \phi_{hyd}(x, y, r) + \phi_{nh}(x, y, r) \quad (2.5)$$

In this work the hydrostatic form of the MITgcm model is used, with  $\epsilon_{nh} = 0$  and  $\phi_{nh} = 0$ .

The pressure terms in the Boussinesq equations (2.2) contain the potential pressure anomaly  $\phi' = \phi - \phi_0$  where  $\phi_0 = p_0/\rho_0$  and  $p_0(z)$  the hydrostatic pressure of the fluid at rest:

$$\frac{\partial p_0(z)}{\partial z} = -g\rho_0 \quad (2.6)$$

Once integrated, it gives

$$p_0(z) = \int_z^0 g\rho_0 dz' = -g\rho_0 z \quad (2.7)$$

where the atmospheric pressure has been neglected  $p_0(0) = p_{atm} \approx 0$ . The model, however, allows to add a loading pressure term to take into account the effect of the pressure at the surface of the ocean.

The total hydrostatic pressure  $p$  is computed by integrating

$$\frac{dp}{dz} = -g\rho \quad (2.8)$$

which gives

$$p(x, y, z, t) = \int_z^\eta g\rho(x, y, z, t) dz' \quad (2.9)$$

where, again, the atmospheric pressure has been neglected  $p(z = \eta) = p_{atm} \approx 0$ . By dividing per  $\rho_0$ , the pressure potential can be computed. After manipulating the integral as

$$\begin{aligned} \phi(x, y, z, t) &= \frac{p}{\rho_0} = \int_z^\eta g \frac{\rho - \rho_0}{\rho_0} dz' + \int_z^\eta g dz' \\ &= - \int_z^\eta b dz' + g(\eta - z) \end{aligned} \quad (2.10)$$

and subtracting by the reference  $p_0/\rho_0$  given by (2.7), the pressure potential anomaly is given by

$$\begin{aligned}\phi'(x, y, z, t) &= \phi(x, y, z, t) - \phi_0(z) \\ &= g\eta(x, y, t) - \int_z^\eta b(x, y, z, t) dz'\end{aligned}\tag{2.11}$$

Thus, at a given depth the pressure potential in the hydrostatic limit is due to the buoyancy of the water above and the displacement of the free surface. The surface and hydrostatic pressure potential anomalies are therefore

$$\begin{aligned}\phi'_s &= g\eta \\ \phi'_{hyd} &= - \int_z^\eta b dz\end{aligned}\tag{2.12}$$

They appear in the Boussinesq equations (2.2) through their gradient. The third momentum equation in the hydrostatic approximation gives

$$\frac{\partial \phi'_{hyd}}{\partial z} = b\tag{2.13}$$

Hereinafter, the prime will be dropped where not needed.

The solution method is different for the hydrostatic or non-hydrostatic forms of the equations, since a combination of the momentum equations and the continuity equation is needed to compute  $\phi_{nh}$ . In the hydrostatic form, instead, the surface pressure and the hydrostatic pressure at any level are computed from the weight of the fluid above, then, the horizontal momentum equations are stepped forward and, finally,  $w$  is obtained diagnostically from the continuity equation  $w = - \int_0^z \nabla_h \cdot \mathbf{v}_h dz'$ .

## 2.1.2 Model discretization and algorithm

### 2.1.2.1 Time stepping

The MITgcm model in the hydrostatic form integrates four prognostic equations for the horizontal flow, temperature and salinity ( $u, v, \theta, S$ ) and solves, through the constraints imposed by the diagnostic equations, three diagnostic equations for vertical flow, density or buoyancy, and pressure potential ( $w, \rho, \phi_{hyd}$ ). In addition, the surface pressure or height may be described by either a prognostic or diagnostic equation.

The algorithm is based on the pressure method for the hydrostatic equations with a rigid-lid or with an implicit linear free surface, with variables co-located in time and with Adams-Bashforth time-stepping method.

The pressure method ensures the non-divergenceness of the flow. In fact, the horizontal momentum equations can not be integrated explicitly from the variables at the previous time step, due to the presence of the unknown pressure term. So, the algorithm, first, finds the intermediate and temporary solution  $(u^*, v^*)$  at time  $n + 1$  given the solution at time  $n$  and  $n + 1/2$ , neglecting the pressure term. In this way, however, the flow can be divergent, and the pressure field at time  $n + 1$  is found to keep the flow non-divergent, as established by the continuity equation. The solution  $(u^{n+1}, v^{n+1})$  is, then, found from  $(u^*, v^*)$  and  $\phi^{n+1}$ .

The rigid-lid condition is the simple surface boundary condition that implies no normal flow at the boundary  $w = 0$  at  $z = \eta$ . It simply gives a vertical integrated continuity equation that doesn't contain  $D\eta/Dt$ . With the assumption of a linear free-surface the vertically integrated continuity equation gives  $\partial_x \int u dz + \partial_y \int v dz = -\partial_t \eta + F$  with  $F$  freshwater term. In this case, the algorithm first finds the intermediate and temporary  $\eta^*$  from the continuity equation given  $\eta^n$  and then  $\eta^{n+1}$  given  $\eta^*$ . In the model a switch-like parameter  $\epsilon_{fs}$  can be set to select between rigid-lid  $\epsilon_{fs} = 0$  and free-surface  $\epsilon_{fs} = 1$ . In this work,  $\epsilon_{fs} = 1$ .

### 2.1.2.2 Spatial discretization

The spatial discretization uses the finite volume method. In the finite volume method, a partial differential equation (PDE), like the advection-diffusion equation for a tracer concentration  $c$ ,

$$\frac{\partial c}{\partial t} + \mathbf{v} \cdot \nabla c = k \nabla^2 c \quad (2.14)$$

in the incompressible Boussinesq approximation, can be written as

$$\frac{\partial c}{\partial t} + \nabla \cdot (\mathbf{v}c - k \nabla c) = \frac{\partial c}{\partial t} + \nabla \cdot \mathbf{F} = 0 \quad (2.15)$$

with  $\mathbf{F} = \mathbf{v}c - k \nabla c$  flux. It can be integrated in discretized cell volumes

$$\int_{V_i} \frac{\partial c}{\partial t} dV + \int_{V_i} \nabla \cdot \mathbf{F} dV = 0 \quad (2.16)$$

and, using the divergence theorem to the flux term, gives

$$V_i \frac{\partial \bar{c}_i}{\partial t} + \int_{S_i} \mathbf{F} \cdot \hat{\mathbf{n}} dS = 0 \quad (2.17)$$

where  $\bar{c} = (1/V_i) \int_{V_i} c_i dV$  is the average value of the concentration  $c$  in the cell  $i$ . Thus, in the finite volume method, the divergence terms in PDEs are converted into fluxes at the surfaces of each finite volume, giving the exact expression for the average value over volumes. Since the flux entering a given volume is identical to that leaving the adjacent volume, this is a conservative method in which one cell's loss is another cell's gain, making it widely used in computational fluid dynamics models compared to finite difference methods.

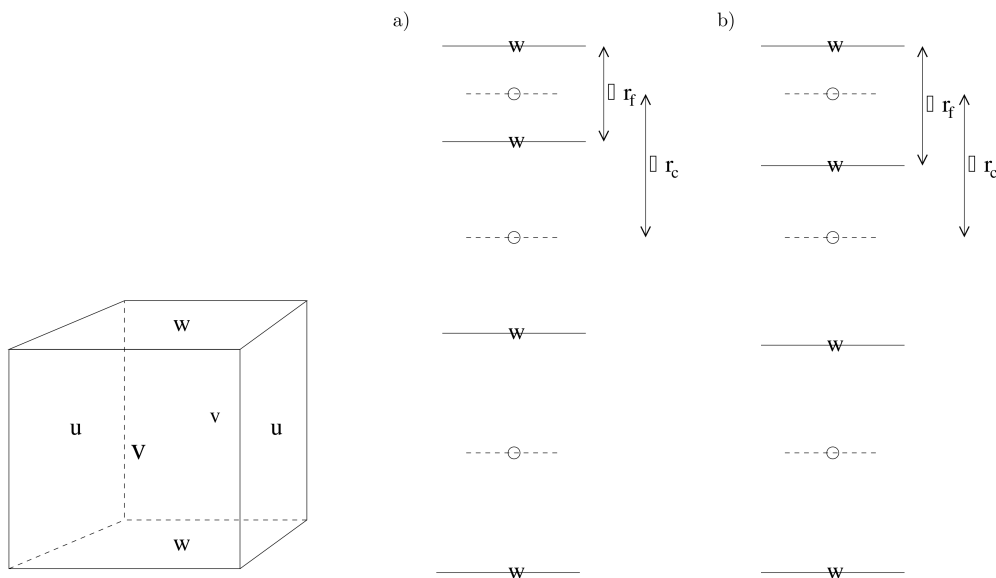


Figure 2.1: On the left: the Arakawa C grid. On the right: cell-centered approach (a) and interface-centered approach (b). Figures taken from MITgcm manual.

The MITgcm model uses the Arakawa C grid discretization (Fig 2.1). Scalar variables are located at mass points and vectors are staggered and located at cell faces. In particular, the component of the flow ( $u, v, w$ ) are staggered in space such that each component falls on the interface between continuity cells in its direction. The continuity cell is also called the tracer cell.

The vertical and horizontal grids are treated separately. There are two versions of the vertical grid: the cell-centered approach and interface-centered approach. In the cell centered approach the interface depths are specified and the tracer points are at cell centers, i.e. centered in between the interfaces. In the interface centered approach tracer levels are specified and the  $w$ -interfaces are centered in between. In this work the horizontal Cartesian coordinates and the cell centered vertical grid are used.

### 2.1.2.3 Continuity equation

The Arakawa C grid discretization is introduced naturally to ensure mass conservation. In the incompressible Boussinesq equations the continuity equation

$$\frac{\partial u}{\partial x} + \frac{\partial v}{\partial y} + \frac{\partial w}{\partial z} = 0 \quad (2.18)$$

can be discretized as

$$\frac{1}{\Delta x} \delta_i u + \frac{1}{\Delta y} \delta_j v + \frac{1}{\Delta z} \delta_k w = 0 \quad (2.19)$$

where  $\delta_i u = u_{i+1/2} - u_{i-1/2}$  with  $i, j, k$  indices for x,y,z directions and  $\Delta x$  the grid spacing in the x-direction. The derivation operator naturally staggers the variables in the three directions. By choosing the C grid discretization the velocities are staggered to ensure the mass conservation inside each cell.

### 2.1.2.4 Energy conservation

The C grid discretization guarantees the energy conservation as the sum of kinetic energy and potential energy.

The kinetic energy per unit mass is defined as

$$KE = \frac{1}{2} (\overline{u^2} + \overline{v^2} + \epsilon_{nh} \overline{w^2}) \quad (2.20)$$

so that it involves only the horizontal velocity components in the hydrostatic version. Due to the staggered grid,  $\overline{(\ )}^i$  stands for the average value of adjacent cell edges in the x-direction ( $\overline{u}^i = (u_{i+1/2} + u_{i-1/2})/2$ ), and gives the average value of the cell which can be considered as located at the cell center. In this way, the kinetic energy is the mean kinetic energy of the cell.

The potential energy can be computed from the buoyancy, a scalar located at cell centers. The potential energy per unit area is

$$\begin{aligned} PE &= \frac{1}{A} \int_A \int_{-H}^{\eta} \rho g z \, dx dy dz \\ &= \frac{1}{A} \int_A \left[ \int_{-H}^{\eta} \rho_0 g z dz - \int_{-H}^{\eta} \rho_0 b z dz \right] dx dy \\ &= \frac{1}{A} \int_A \rho_0 \left[ \frac{1}{2} g (\eta^2 - H^2) - \int_{-H}^{\eta} b z dz \right] dx dy \end{aligned} \quad (2.21)$$

and subtracting the initial value and dividing per  $\rho_0$  gives

$$PE = \frac{1}{A} \int_A \left[ - \int_{-H}^{\eta} b z dz + \frac{1}{2} g \eta^2 \right] dx dy \quad (2.22)$$

Thus, the potential energy is a quantity of each cell, located at the cell centers.

Energy is conserved in the whole domain volume, due to the staggered C grid.

### 2.1.2.5 Hydrostatic balance

The discretized vertical momentum equation can be written as

$$\epsilon_{nh} \frac{\partial w}{\partial t} + g \frac{\bar{\rho}'^k}{\rho_0} + \frac{1}{\Delta z} \delta_k \phi' = \dots \quad (2.23)$$

by putting the non linear terms and forcing and dissipation terms to the RHS. This equation is built consistently with the momentum equation meaning, that is to solve the equation for the velocity. The discretized form of the third momentum equation finds the solution  $w$  located at cell faces in z-direction in the Arakawa C grid. Thus, all the terms in the momentum equation has to be consistently located at vertical cell faces. The buoyancy term needs to be computed as its mean value in z-direction: the average of the density anomaly is indicated as  $\bar{\rho}'^k$ . The pressure term, even though located at mass points, instead, doesn't need to be averaged, since here its vertical derivative staggers its location to the cell vertical faces.

A consideration about buoyancy needs to be make here. Apparently, once discretized, the diagnostic definition of the buoyancy from density anomaly (2.4) is inconsistent with the dynamical definition one can get from the hydrostatic balance (2.13). The diagnostic definition  $b = -g\rho'/\rho_0$  represents the cell-average buoyancy;  $\rho$ , indeed, is located at cell centers, as  $S$  and  $\theta$  scalars, in order to guarantee tracer and mass conservations. Beside the pressure potential located at cell centers  $\phi_C$ , so far called simply  $\phi$ , the MITgcm introduces another pressure potential located at cell faces in the vertical  $\phi_F$ . They are related one each other and compute in the CALC\_PHI\_HYD subroutine as PhiHydC and PhiHydF variables.  $\phi_F$  can be computed from  $\phi_C$ , using as boundary condition at the surface the displacement of the free surface.  $\phi_C$  enters the third momentum equation, while  $\phi_F$  gives the right buoyancy meaning, identical to the buoyancy definition:

$$\frac{1}{\Delta z} \delta_k \phi'_F = b_C = b \quad (2.24)$$

The buoyancy in the hydrostatic balance, is, instead, located at cell faces:

$$\frac{1}{\Delta z} \delta_k \phi'_C = b_F \quad (2.25)$$

As a result  $b_F$  and  $b_C$  and linearly related.  $b_C$  is the buoyancy cell-average value.

### 2.1.3 Thermodynamic sea ice package

Sea ice is simulated using the thermodynamic sea ice package of the MITgcm model, THSICE. It is based on the 3-layer sea ice model introduced by *Winton* [2000] and the energy conserving thermodynamic model of sea ice by *Bitz and Lipscomb* [1999]. The model only treats the thermodynamics of sea ice, neglecting the dynamics, which is, instead, set by the SEAICE package of the MITgcm model, based on the viscous plastic model [*Hibler*, 1979].

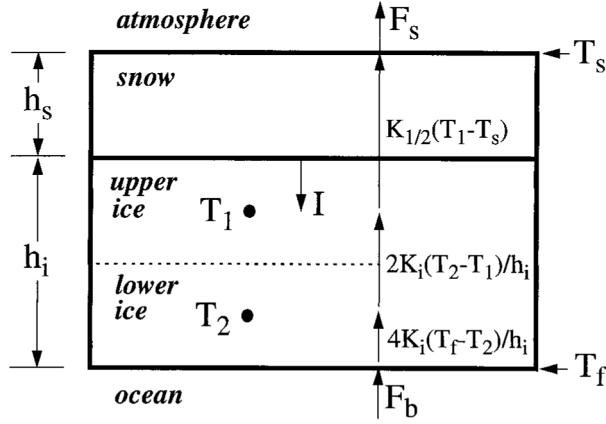


Figure 2.2: Schematic of the three-layer model for sea ice. From *Winton* [2000].

In the THSICE package, sea ice is represented with 3 layers: 2 layers of sea ice, of equal thickness,  $h_i$ , and 1 layer of snow above the sea ice, with thickness  $h_s$ . The lower sea ice layer has fixed heat capacity, while the upper sea ice layer has variable heat capacity to represent brine pockets effect. In fact, the presence of salt in seawater creates brine pockets within the sea ice structure, lowering the heat capacity with the brine content. The snow layer has, instead, zero heat capacity. The model has four prognostic variables:  $h_s$ ,  $h_i$ ,  $T_1$ , and  $T_2$ , upper and lower sea ice layers temperature, respectively. Heat fluxes at the top and bottom surfaces determine sea ice temperature and sea ice and snow thicknesses. Grid cells are the same of the ocean model and the ocean surface layer grid cell can be fully covered by sea ice or open water.

First, the model evaluates the freezing potential for the upper ocean layer at each cell:

$$frzmlt = (T_f - SST) \frac{c_{sw} \rho_{sw} \Delta z}{\Delta t} \quad (2.26)$$

where  $\Delta z$  is the ocean upper layer thickness,  $\Delta t$  is the model timestep,  $c_{sw}$  is the seawater heat capacity,  $\rho_{sw}$  the seawater density,  $T_f = \mu S$  is the freezing temper-

ature of seawater (it depends on the salinity and  $\mu$  is an empirical constant) and  $SST$  is the sea surface temperature. Accordingly to  $SST$ ,  $frzmlt$  can be positive or negative. If  $SST < T_f$ ,  $frzmlt > 0$ , leading to freezing and salinity within brine is released, otherwise if  $SST > T_f$ ,  $frzmlt < 0$  and sea ice melts where present.

Then, the thermodynamics of sea ice computes the sea ice surface temperature, the two layer sea ice temperatures and the sea ice and snow thicknesses. It uses the energy balance at the surface (where the albedo is computed with the Los Alamos National Laboratory sea ice model, LANL CICE) and the heat conduction through the snow and ice. Among the output of the thermodynamic package of sea ice, there are the heat flux out of the ocean, the fresh-water flux out of the ocean, the salt flux out of the ocean, that are used to model the ocean response.

In this work the thermodynamic sea ice package of the MITgcm model with only 2 layers of sea ice and without the snow cover for the absence of precipitation is used. Moreover, in this formulation of the model, the pressure exerted by sea ice is not added at the surface of the ocean, since the pressure of the ocean is assumed to be the pressure of ocean water and sea ice melted:  $\eta$  is the level of the free surface when all the ice is melt.

#### 2.1.4 CheapAML package

The MITgcm model is provided with an atmospheric package, the Cheap Atmospheric Mixed Layer (CheapAML) model, that performs atmospheric temperature and humidity in the atmospheric boundary layer. It is a fully coupled ocean-atmosphere model developed for ocean-only modeling in order to better represent air-sea exchanges. Here, atmospheric temperature is specified and air-sea fluxes are computed through parametrizations.

#### 2.1.5 Eddy viscosity and diffusivity

In this work, the eddy viscosity is parametrized by the Smagorinsky scheme. The Smagorinsky approach for the turbulent closure of the equations (Sec. 1.5.1) is already implemented in the MITgcm model. It can be set by the user through the parameter `viscC2Smag`, which estimates the energy flux at every grid point and adjusts the viscosity accordingly. However, only the horizontal viscosity is implemented in the MITgcm model, so there is no vertical viscosity. Moreover, although Smagorinsky set the eddy diffusivity to be equal to the eddy viscosity, in this work the diffusion is not explicitly parametrized, and only numerical diffusion is allowed, following the upwinding/advection scheme. Vertical mixing, instead,

is realized through convective adjustment of buoyancy, which is the numerical procedure that immediately adjusts the buoyancy to the  $N^2 = 0$  profile in order to prevent unstable stratification.

## 2.2 Numerical model configuration

The model domain is a square ocean channel of 50 km x 50 km with 75 m depth. The depth of the ocean doesn't affect the solution since, as will be seen, the relevant ocean dynamics concerns only the upper layers of the ocean. The horizontal resolution is 50 m with 1000 grid cells in each horizontal directions; the vertical resolution is 2.5 m with 30 vertical levels. The use of high resolution allows to resolve the submesoscale eddies from their initial development as small instabilities in the along edge direction. The model solves the Boussinesq equations in the tangent f-plane approximation, which establishes isotropy in the horizontal directions. The axis can be, therefore, oriented as preferred. Here, the sea ice edge is positioned at the center of the channel and it is zonally oriented, with the origin of the y-axis  $y = 0$  at the sea ice-edge, so that, in the limit of two interacting sea ice edge, the axis of the lead is oriented in the x-direction. The left and right regions of the ocean domain with respect to the ice-edge are an ice-free region and an ice covered region, respectively. The boundaries are taken as rigid wall at  $y = -25$  km and  $y = 25$  km and open periodic boundaries at  $x = 0$  km and  $x = 50$  km. The symmetry in the along-edge direction simplifies the configuration that, as will be seen, under certain circumstances, can be considered as two-dimensional.

### 2.2.1 Initial ocean state

The initial atmospheric and oceanic conditions are the typical conditions of the winter Arctic region. The ocean has a constant temperature at freezing point and is highly stratified by salt, with a strong halocline located at -25 m depth (Fig. 2.3). The salinity jump at the halocline is  $0.0033 \text{ ms}^{-2}$ . The halocline separates the water column into a mixed-layer (ML) surface ocean and an interior ocean. The depth of the mixed-layer is chosen of 25 m, which resembles the real winter Arctic Ocean ML depth. Furthermore, the ocean ML depth is not interesting in its absolute value, but it becomes relevant when compared to the width of the lead, which is not subject of the single sea-ice edge system, but will be studied in a following work. The ocean is initially at rest. There are no solar forcing, resembling the winter polar night, and precipitation. Wind stress, also, is not considered. The initial atmospheric temperature is  $-20^\circ\text{C}$ . Sea ice is initialized in the ice covered domain as grid cell with 100% ice concentration and ice thickness of 2 m.

The simulation runs for 30 days from the initial state, to let baroclinic instabilities evolve and submesoscale eddies grow. The numerical model time step is taken to be 60 seconds or 30 seconds, in order to have convergent solutions. The Coriolis parameter is set to  $f = 1.4 \times 10^{-4} \text{ s}^{-1}$ , which corresponds to a latitude of  $73.7308^\circ \text{N}$ . This simulation is referred to as Standard simulation.

Two possible initial conditions with the same salinity jump at the mixed layer base but different interior stratifications are compared in Fig. 2.3: in the High stratification case the salinity profile below the ML is increased by 0.2 at each vertical level with respect to the Low stratification case. The ocean response is evident in Fig. 2.4. In the left figure, in the High stratification case the density anomaly with respect to the initial state affects only the mixed layer without propagating into the deep ocean, while, in the Low stratification case, after 12 days, some part of the high ML density is lost in the deep ocean, reducing the strength of the ML front. The right figure in Fig. 2.4, for which a full explanation is given in Sec. 3.7, shows the kinetic energy ratio between three and two-dimensional configurations for the High and Low stratification simulations. The important thing to be noted, here, is that the Low stratification case reaches an energy saturation level after 10 days, while the High stratification run increases its energy in time. Hereafter, since the goal is to study the dynamics of the mixed layer affected by brine rejection, the High resolution stratification initial condition is used.

Moreover, the dynamics of the ML depends on the forces that play role in the system, such as the strength of the brine rejection phenomenon, the Coriolis force, the presence of baroclinic instabilities. The effect of different forcing is studied separately, by building ad hoc idealized numerical experiments.

### 2.2.2 External atmospheric forcing

The Standard simulation is initialized with atmospheric temperature of  $-20^\circ \text{C}$ . In order to study the role of atmospheric forcing in determining the strength of the front, the intensity of the eddy field and the rate of change of the restratification process, two other simulations with higher and lower external forcing, respectively, are performed. They are referred to as T0 ( $T_{air} = 0^\circ \text{C}$ ) and T40 ( $T_{air} = -40^\circ \text{C}$ ) simulations, and they have the same initial ocean state as the Standard simulation.

### 2.2.3 Two and three-dimensional configurations

It has already been mentioned that the special symmetry along the ice-edge can simplify the study from a three-dimensional to a two-dimensional dynamics. Simpler two-dimensional configurations, with only one grid cell in the along-edge

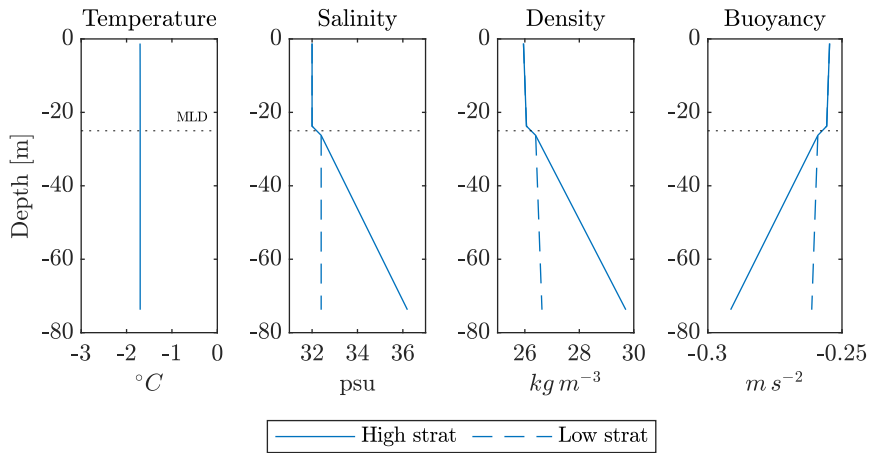


Figure 2.3: Initial ocean state for High stratification case (solid lines) and Low stratification case (dashed lines). The dotted line represents the mixed-layer depth at -25 m.

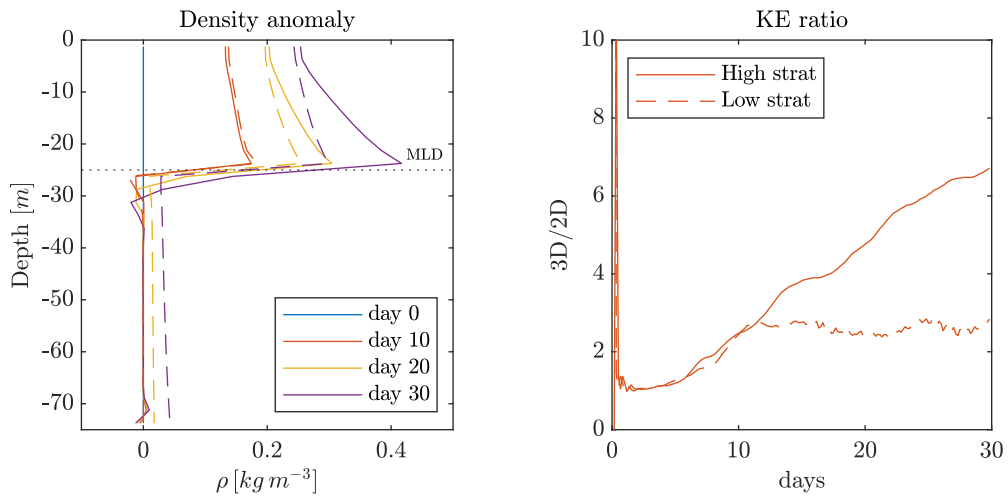


Figure 2.4: Comparison between High stratification case (solid lines) and Low stratification case (dashed lines). On the left: density anomaly with respect to initial state for solutions at different days. On the right: time evolution of kinetic energy ratio between three and two-dimensional configurations.

direction, are built in order to study the differences between the symmetric three-dimensional and the pure two-dimensional configurations.

The two-dimensional configuration is to be intended as the limit case of the three-dimensional configuration where the variability of the variables in the zonal direction is null, or, in other words, the two-dimensional variables have the same values for all the zonal three-dimensional cells, equal to the zonal average values. In two-dimensional configurations, in fact, the perturbation of the mean flow in the along-edge direction is  $u' = u - \bar{u} = u - \int_0^{L_x} u dx = U - \int_0^{L_x} U dx = U - U = 0$ , where  $\bar{(\ )} = \int_0^{L_x} (\ ) dx$  is the average in the zonal direction and  $U(y, x, t)$  is the zonal average velocity. As a consequence of geometry, in the two-dimensional configurations the instabilities in the along-edge direction can not develop.

The comparison of two and three-dimensional configurations would help to quantify the effect of the submesoscale instability in the restratification mechanism. Thus, two-dimensional simulations are performed for each external atmospheric forcing condition, and are referred to as 2D simulations.

#### 2.2.4 Coriolis parameter

Another simulation experiment is run in the absence of the Coriolis force, and it is therefore called Nof simulation. In the  $f = 0$  case, the geostrophic adjustment problem doesn't show an equilibrium where the horizontal density gradients are maintained. In fact, no net velocity develops in the along-edge direction. For the absence of the Earth rotation, the small random distributed instabilities in the zonal direction can not strengthen, making the three-dimensional configuration very similar to the two-dimensional one. For this reason, here, only two-dimensional Nof simulation is performed.

#### 2.2.5 Covered and open ocean configurations

Two tests simulations are run as limiting cases of the Standard simulation, one in which all the domain is covered by sea ice (100% sea ice concentration at every grid cell) and one that is totally ice-free (0% sea ice concentration everywhere). Since in these limiting configurations fronts can not evolve, for simplicity they are run only in the two-dimensional configuration.

All the run experiments are summarized in Table 2.1. They have the same initial ocean state, corresponding to the High stratification case in Fig. 2.3.

Experiment	Dimension	$T_{air}$	Sea ice cover	Coriolis parameter
Standard	2D-3D	$-20\text{ }^{\circ}\text{C}$	50%	$f = 1.4 \times 10^{-4} \text{ s}^{-1}$
T0	2D-3D	$0\text{ }^{\circ}\text{C}$	50%	$f = 1.4 \times 10^{-4} \text{ s}^{-1}$
T40	2D-3D	$-40\text{ }^{\circ}\text{C}$	50%	$f = 1.4 \times 10^{-4} \text{ s}^{-1}$
Nof	2D	$-20\text{ }^{\circ}\text{C}$	50%	$f = 0$
Covered	2D	$-20\text{ }^{\circ}\text{C}$	100%	$f = 1.4 \times 10^{-4} \text{ s}^{-1}$
Open	2D	$-20\text{ }^{\circ}\text{C}$	0%	$f = 1.4 \times 10^{-4} \text{ s}^{-1}$

Table 2.1: Experimental runs characteristics.

## 2.3 Diagnostics

The frozen atmospheric temperature tend to freeze the ice-free ocean surface which rejects brine into the ocean. As a consequence, the density of the mixed layer ocean in the ice-free domain increases, while the other ocean region has roughly unaltered properties due to insulation of sea ice cover. The real insulation effect of sea ice will be investigated by looking at heat fluxes. The density increase in the open ocean region is due only to salt fluxes, since cooling doesn't affect the ocean temperature that is already at freezing point. Due to strong horizontal density gradients, a front develops along the ice-edge. As will be studied, density gradients, here, are continually enforced due to the persistent brine rejection in the open ocean region, even after a very thin layer of sea ice has formed.

The goal of this work is to study and quantify the restratification process of the Arctic Ocean mixed-layer driven by brine rejection. The different experiments would help in separating the single mechanisms that play role in the system. In the non rotating frame the restratification brings the new formed dense water below the light water; in a rotating frame the restratification is blocked by the geostrophic adjustment which leaves the front slightly tilted in geostrophic balance; finally, if instabilities develop and grow to submesoscale eddies, the restratification is enhanced.

In this section, methods and tools for diagnosing the output of the model experiments are shown. Important diagnostic physical quantities, such as buoyancy, overturning streamfunction, potential vorticity, potential and kinetic energy, are defined here, while results are shown in the Chapter 3.

### 2.3.1 Anomalies from initial state

Since the ocean is initially at rest, it is interesting to look at the variability of a given physical quantity during the period of time of the experiment. For these

reason, many diagnosed variables, such as density, buoyancy, potential vorticity, potential energy, are interesting for their anomalies from their values at the initial condition. The anomalies from initial condition will be often referred simply to as anomalies, indicated with  $()'$ .

As an example, the density anomaly from initial condition is the density anomaly (with respect to the fixed reference density of water  $\rho_0 = 999.8 \text{ kg m}^{-3}$ ) variability from the initial density anomaly, or, equivalently, the density variability from the initial density:

$$\rho'(t) = (\rho(t) - \rho_0) - (\rho(t=0) - \rho_0) = \rho(t) - \rho(t=0) \quad (2.27)$$

### 2.3.2 The along ice-edge average

As mentioned above, the particular zonal symmetric geometry provides a method of study that simplifies the analysis and can be widely used for every run experiments: the zonal average.

Each variable can be written using the Reynolds decomposition rule into a mean value and a fluctuation. For example for flow field

$$\mathbf{u} = \mathbf{U} + \mathbf{u}' \quad (2.28)$$

where  $\mathbf{U} \equiv \bar{\mathbf{u}} = \int_0^{L_x} \mathbf{u} dx$  is the average in the along ice-edge direction, or, equivalently, also called the zonal average, and  $\mathbf{u}' = \mathbf{u} - \mathbf{U}$  is the zonal mean perturbation. In the two-dimensional simulations,  $\mathbf{u} = \mathbf{U}$  and  $\mathbf{u}' = 0$ , since there is only one grid cell in the along ice-edge direction.

In the absence of the Earth rotation,  $\mathbf{U} = 0$ , since the only velocity that grows is across the ice-edge, i.e. along the density gradients, and only  $\mathbf{u}'$  develops as random fluctuation and can not grow through coupling with the mean flow,  $\mathbf{u}' \approx 0$ . Thus, the two-dimensional limit of  $f = 0$ , with  $\mathbf{U} = 0$  and  $\mathbf{u}' = 0$ , leads to almost the same results. The same holds for the Covered and Open set-ups, where no horizontal gradients form and the absence of a flow in the y-direction doesn't allow the formation of the perpendicular x-flow, despite the existence of the Coriolis force.

Only the combination of Earth's rotation and three-dimensionality can lead to enhanced along ice-edge instabilities that grow in time and affect the mean flow and the energy of the system. The comparison between two and three-dimensional configurations would quantify the effect of submesoscale eddies in the restratification process.

A diagnostic tool useful for visualizing the time evolution of a zonally average quantity is the Hovmöller diagram, which shows the rate of change of a quantity in the across edge direction, i.e. placing time versus  $y$ -axis. Indeed, the  $x$ -axis in the Hovmöller diagram is taken to be the distance from the ice-edge. The quantity diagnosed in the Hovmöller diagrams is considered at a certain depth or is an average of many vertical levels, such as the whole water column average or the mixed-layer average. Density and buoyancy are typical properties that are investigated through Hovmöller diagrams. They are useful to visualize the rate of change of the spread of density from the denser region toward the lighter region.

### 2.3.3 Buoyancy budget

The buoyancy equation in the Boussinesq system ( $\nabla \cdot \mathbf{u} = 0$ ) is

$$\frac{Db}{Dt} = \frac{\partial b}{\partial t} + \nabla \cdot (\mathbf{u}b) = \mathcal{D} \quad (2.29)$$

where  $\mathcal{D}$  is the diabatic forcing, which here represents the surface flux of buoyancy due to brine rejection. When the along-ice-edge average is taken, the time evolution of the mean buoyancy is governed by

$$\frac{\partial \bar{b}}{\partial t} = -\frac{\partial}{\partial y}(\bar{v}\bar{b}) - \frac{\partial}{\partial z}(\bar{w}\bar{b}) - \frac{\partial}{\partial y}(\overline{v'b'}) - \frac{\partial}{\partial z}(\overline{w'b'}) + \bar{\mathcal{D}} \quad (2.30)$$

Note that the average does not depend on the  $x$ -derivatives and the flow in the  $x$  direction. The mean buoyancy is advected not only by the mean flow but it is also affected by the advection by the perturbed eddy flow.  $\overline{v'b'}$  and  $\overline{w'b'}$  are called eddy fluxes of buoyancy and their convergence/divergence changes locally the mean buoyancy.

In the two-dimensional configurations, there are zero perturbations in the along ice edge direction, and the buoyancy budget in (2.30) only depends on the average quantities. This is not the case for three-dimensional configurations.

### 2.3.4 Potential vorticity budget

An important quantity that is often used as a constraint on rotational fluids due to its conservation property is the potential vorticity. In the Boussinesq system of equations the potential vorticity (PV) has the form of the Ertel PV, which links the absolute vorticity to the gradient of buoyancy:

$$Q = (\boldsymbol{\omega} + \mathbf{f}) \cdot \nabla b \quad (2.31)$$

where  $\boldsymbol{\omega} = \nabla \times \mathbf{u}$  is the relative vorticity of the fluid,  $\mathbf{f}$  is the planetary vorticity, and their sum is the absolute vorticity.

The Ertel PV equation, which is fully derived from the Boussinesq equations in Appendix B, is:

$$\frac{DQ}{Dt} = (\nabla \times \mathcal{F}) \cdot \nabla b + (\boldsymbol{\omega} + \mathbf{f}) \cdot \nabla \mathcal{D} \quad (2.32)$$

where the terms in the R.H.S. are non conservative terms due to frictional and diabatic forcing. In this study of submesoscale eddies due to brine rejection, PV dynamics is due to surface buoyancy injection, which is expressed by  $Db/Dt = \mathcal{D}$ , and internal friction  $\mathcal{F}$ . In particular, the rejection of brine injects negative buoyancy and, with it, negative PV, (2.32). Apart from injection of new PV and internal stresses, PV is also redistributed in the domain due to the advection term.

Explicitly the Boussinesq Ertel PV is:

$$Q = (v_x - u_y)b_z + (w_y - v_z)b_x + (u_z - w_x)b_y + fb_z \quad (2.33)$$

where x, y, z indices represents partial derivatives ( $u_y = \partial u / \partial y$ ). Again, due to the presence of a symmetric axis, it is interesting to look at the along-ice-edge average PV:

$$\bar{Q} = Q_{mean} + Q_{eddy} \quad (2.34)$$

after decomposing each variable as  $a = \bar{a} + a'$  with  $\bar{(\ )}$  denoting the zonal average such that  $\bar{(\ )}' = 0$ , where

$$\begin{aligned} Q_{mean} &\equiv (f - \bar{u}_y)\bar{b}_z + \bar{u}_z\bar{b}_y = fN^2 - U_yN^2 + U_zM^2 \\ Q_{eddy} &\equiv \bar{Q} - Q_{mean} = \overline{v'_xb'_z} - \overline{u'_yb'_z} - \overline{v'_zb'_x} + \overline{u'_zb'_y} \end{aligned} \quad (2.35)$$

where capital letters are used for the zonal average,  $w'$  has been approximated to zero and

$$\begin{aligned} N^2 &= \frac{\partial \bar{b}}{\partial z} \\ M^2 &= \frac{\partial \bar{b}}{\partial y} \end{aligned} \quad (2.36)$$

are the vertical stratification and the analogous for the horizontal direction along the buoyancy gradient.

### 2.3.5 Energy budget

How does the energy of the system evolve? It has been said that fronts store potential energy in the horizontal density gradients. This potential energy is converted into kinetic energy by the gravitational force that slumps the fronts in order to subtract its potential energy, reducing the horizontal density gradient. If no other forces are present, the balance is reached when pressure potential gradients are opposite to gravity, that is when the front is completely tilted and horizontal density gradients are converted into vertical density gradients. In this case, the fluid is restratified and light water sits above dense water and the potential energy has been totally converted into kinetic energy, which finally stops all the motions. However, many forces can interact with each other and change the equilibrium state. For example, when the Earth rotation is present, a balance between horizontal pressure gradients and Coriolis force is established, known as the geostrophic balance. Geostrophic adjustment prevents the complete slump of the front, leaving it tilted with an important amount of potential energy still stored in it. Eventually, this potential energy can be used to create baroclinic instability that can grow to finite amplitude into eddies. Eddies subtract more potential energy tilting the front and transfer this energy into kinetic energy. Furthermore, here, a final equilibrium state is never reached in the period of time considered. Thus, the study of the energetics of this system is useful in quantifying the efficiency of transfer of energy under different forcing.

First, the potential energy is computed as in Sec. 2.1.2.4. The vertically integrated potential energy anomaly from initial condition per unit mass is

$$PE = \frac{1}{A} \int_A \left[ - \int_{-H}^{\eta} bz dz + \frac{1}{2} g \eta^2 \right] dx dy \quad (2.37)$$

Sec. 2.1.2.4 also computes the kinetic energy for every grid cell. The kinetic energy per unit mass is computed from the velocities in the three direction as

$$KE = \frac{1}{2} (u^2 + v^2 + w^2) \quad (2.38)$$

which can be simply written with indices contraction following the Einstein rule as  $KE = \frac{1}{2} u_i^2$ . Again, since the goal is to study the along-ice-edge average quantities, also the zonal kinetic energy, as the zonal PV, results from the sum of two different terms, the kinetic energy of the the mean flow and the kinetic energy of the eddy flow:

$$\begin{aligned} \overline{KE} &= \frac{1}{2} \overline{u_i^2} = \frac{1}{2} \overline{u_i^2} + \frac{1}{2} \overline{(u')_i^2} \\ &\equiv MKE + EKE \end{aligned} \quad (2.39)$$

In order to compare the kinetic energy with the potential energy, they should have consistent units, and the kinetic energy in (2.39) is, thus, vertically integrated.

In fully non-linear problems, such as where instabilities can grow into big eddies, the EKE is not negligible with respect to the MKE, but it drives, instead, the total kinetic energy by subtracting energy from the mean flow. This is clearly visible when writing the energy budget. Since the average kinetic energy can be divided into two terms as in (2.39), two energy budgets for the two components can be build (see Appendix C for derivation):

$$\frac{D^M}{Dt}(MKE) = -\frac{\partial}{\partial x_i} U_i \bar{\phi} + W \bar{b} - \frac{\partial}{\partial x_j} (\overline{u'_i u'_j U_i}) + \overline{u'_i u'_j} \frac{\partial U_i}{\partial x_j} \quad (2.40)$$

$$\frac{D^M}{Dt}(EKE) = -\frac{\partial}{\partial x_j} \left( \frac{1}{2} \overline{(u'_i)^2 u'_j} \right) - \underbrace{\frac{\partial}{\partial x_i} \overline{u'_i \phi'}}_{PW} + \underbrace{\overline{b' w'}}_{BP} - \underbrace{\overline{u'_i u'_j} \frac{\partial U_i}{\partial x_j}}_{SP} \quad (2.41)$$

where  $\frac{D^M}{Dt} = \frac{\partial}{\partial t} + U_j \frac{\partial}{\partial x_j}$  is the material derivative with respect to the mean flow. The Coriolis term has been ignored, since it is not constituting a source term but it moves energy, due to its linear form.

The shear production term appears in both MKE and EKE equations with an opposite sign, indicating a transfer of energy between the mean and the eddy flow. Shear production SP, buoyancy production BP, pressure work PW, can be positive or negative depending on stratification, mean shear flow and pressure. If  $N^2 < 0$ , the buoyancy production term is positive and creates EKE by pushing lighter water above denser water, because, if the parcel deviates toward the surface,  $w' > 0$ , it would create  $b' > 0$ , giving  $\overline{w' b'} > 0$ .

The averages in (2.40) and (2.41) is here intended as the zonal average. Thus, in this work, after canceling out the zero terms, the shear production term is made by:

$$\begin{aligned} SP &\equiv \overline{u'_i u'_j} \frac{\partial U_i}{\partial x_j} = \overline{u' v'} U_y + \overline{u' w'} U_z + \overline{v' w'} V_z + \overline{v' w'} W_y \\ &\approx \underbrace{\overline{u' v'} U_y}_{HSP} + \underbrace{\overline{u' w'} U_z + \overline{v' w'} V_z}_{VSP} \end{aligned} \quad (2.42)$$

where the  $W_y$  term is negligible since  $W \approx 0$ ; HSP stands for horizontal shear production and VSP for vertical shear production.

### 2.3.6 Overturning streamfunction

For the geometry of the frontal spindown system, velocities develop and act to slump the front. This mechanism of frontal tilting can be explained through the introduction of an overturning streamfunction that tilts the isopycnals in the mixed-layer from the vertical toward the horizontal.

The existence of the overturning streamfunction lies in the divergenceless of the along-edge averaged velocity in the  $y$ - $z$  plane. In fact, averaging the continuity equation gives

$$\frac{\partial \bar{v}}{\partial y} + \frac{\partial \bar{w}}{\partial z} = 0 \quad (2.43)$$

where  $\partial_x \bar{u} = 0$ . Thus, a streamfunction can be defined such that

$$\begin{aligned} \bar{v} &= \frac{\partial \Psi_E}{\partial z} \\ \bar{w} &= -\frac{\partial \Psi_E}{\partial y} \end{aligned} \quad (2.44)$$

Note that this streamfunction is only considering the mean velocity, and perfectly represents the frontal overturning when eddies don't affect the restratification process of the ML. However, submesoscale eddies enhance the overturning circulation and the streamfunction defined in (2.44) is not sufficient.

An eddy overturning streamfunction needs to be introduced to account for the eddy effect:

$$\begin{aligned} \overline{v'b'} &= -\Psi^* \bar{b}_z \\ \overline{w'b'} &= \Psi^* \bar{b}_y \end{aligned} \quad (2.45)$$

In this way, the buoyancy eddy fluxes are written in terms of the eddy overturning streamfunction  $\Psi^*$ , different from the Eulerian overturning streamfunction  $\Psi_E$  defined in (2.44) and obtained from the Eulerian velocities  $\bar{v}$  and  $\bar{w}$ . A parametrization of the eddy fluxes can be built by writing the eddy overturning streamfunction  $\Psi^*$  in terms of the gradient of the mean buoyancy field [*Fox-Kemper et al.*, 2008] (see Appendix A). However, here, since there were built eddy-resolving simulations, the eddy fluxes can be directly computed and the eddy overturning streamfunction can be directly compared to the Eulerian overturning streamfunction. The Eulerian overturning streamfunction, from (2.44), is computed as

$$\Psi_E = \int_{-H}^z \bar{v} dz \quad (2.46)$$

where the bottom  $z = -H$  is chosen as reference, so that  $\Psi_E(z = -H) = 0$ .  $\bar{w}$  is not used here since it is smaller than  $\bar{v}$ . The eddy overturning streamfunction is, instead,

$$\begin{aligned}\Psi^* &= -\frac{\overline{v'b'}}{\bar{b}_z} \\ \Psi^* &= \frac{\overline{w'b'}}{\bar{b}_y}\end{aligned}\tag{2.47}$$

Note that  $\Psi^*$  is positive when the overturning circulation slumps the isopycnals, i.e.  $\overline{w'b'}$  and  $\bar{b}_y$  both positive. The use of both the two expressions in (2.47) will be further discussed in Chapter 3.

Finally, the eddy overturning streamfunction produces eddy induced velocity, known as Bolus velocity,

$$\mathbf{u}^* = \nabla \times \Psi\tag{2.48}$$

which, explicitly, are

$$\begin{aligned}v^* &= \frac{\partial \Psi^*}{\partial z} \\ w^* &= -\frac{\partial \Psi^*}{\partial y}\end{aligned}\tag{2.49}$$

They can be further used to compare with the Eulerian velocity (2.44).

The two overturning streamfunctions,  $\Psi_E$  and  $\Psi^*$ , contribute together to the overall circulation. The residual circulation is defined as

$$\Psi_{res} = \Psi_E + \Psi^*\tag{2.50}$$

and it produces a residual overturning velocity

$$v_{res} = \bar{v} + v^*\tag{2.51}$$

# Chapter 3

## Results and Discussion

In this chapter numerical model results of the configuration experiments of a single sea ice edge system driven by brine rejection under atmospheric cooling (Table 2.1, Sec. 2.2) are investigated and discussed, using the tools described in Sec. 2.3.

### 3.1 Surface forcing

Atmosphere and ocean are coupled together through surface fluxes of heat, temperature and salinity. The presence of surface fluxes drives the ocean response under variable sea ice cover. Surface fluxes act both in the open ocean region and in the ice-covered region of the experimental domain, with different magnitudes due to the insulating properties of sea ice.

Heat fluxes from the ocean to the atmosphere are highest in magnitude in the open ocean region though, although small, they are present in the ice-covered region, where the sea ice still loses a small amount of heat to the atmosphere. The central upper panel in Fig. 3.1 shows the along-edge surface heat flux (positive = cooling) in the across-edge direction, with positive sign for fluxes from the ocean out toward the atmosphere. The initial net surface cooling in the ice-free region is  $208 \text{ Wm}^{-2}$ , while it is  $55 \text{ Wm}^{-2}$  in the ice-covered region. This cooling in the open ocean area leads to sea ice formation and brine rejection. The presence of surface cooling in the ice-covered area implies some sea ice growth and brine rejection in the covered region. Over time, the surface cooling attenuates in both regions as new sea ice forms but it never reaches zero during the simulation.

Heat fluxes imply temperature and salinity fluxes. Temperature fluxes are approximately zero in both regions since the ocean temperature is already near

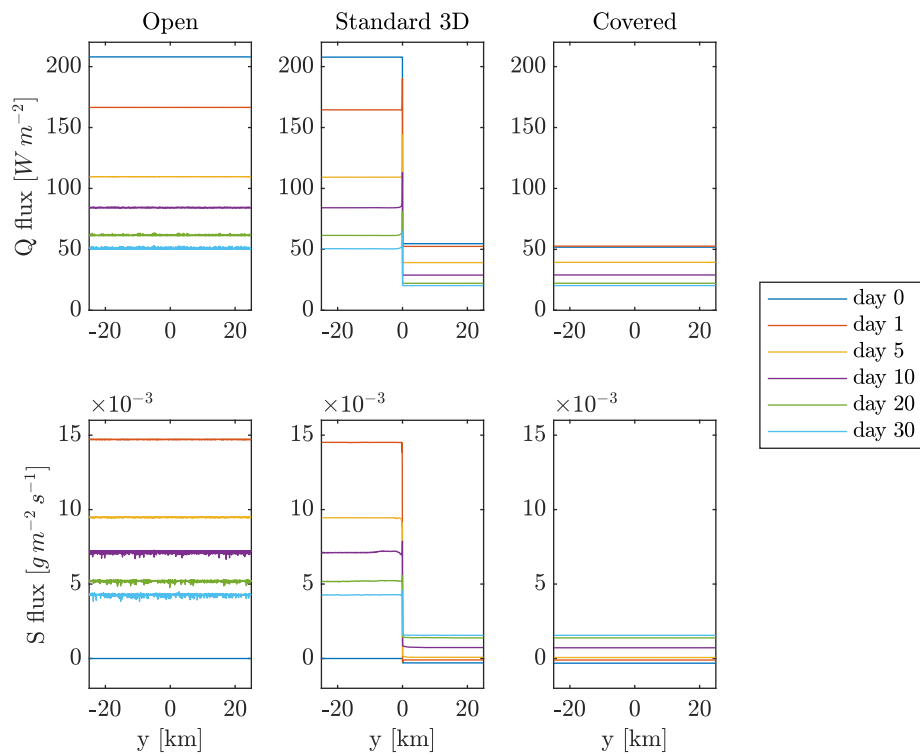


Figure 3.1: Heat and salinity fluxes evolution in the across-edge direction for Open (left), Centered (right) and Standard 3D (center) simulations. For the Standard 3D simulation, average along the sea ice edge direction is taken.

freezing. The surface salinity forcing drives the ocean dynamics as a consequence of cooling. Salinity fluxes are initialized to be zero and immediately established in balance with the latent heat loss to the atmosphere. In the open ocean region, salinity fluxes decrease over time as new sea ice forms, though they increase in time in the ice-covered region (central lower panel in Fig. 3.1). This can be explained by the initial temperature of sea ice which is not in balance with air temperature. Heat fluxes start to remove energy from the upper layer of sea ice, without influencing the ocean below. Only later, when sea ice is in balance with the atmosphere, the oceanic upper layer starts to be cooled and freezes, rejecting brine through positive salinity fluxes into the ocean. Sea ice thickness grows and never reaches equilibrium in the time scale of these simulations. In the open ocean region, as cooling is persistent over all times, also the salinity fluxes never reaches zero. This means that brine rejection is expected to continue, altering the balance and preventing to reach an equilibrium state.

Surface fluxes for both Open and Covered simulations are plotted in Fig. 3.1. The small variability in the y-direction that is present in the two-dimensional simulations is not visible in the Standard 3D case, since in the latter the along ice-edge average of the fluxes is taken, removing the random perturbation. Fluxes for the Standard 3D simulation in the two regions are the same as for the Open and Covered simulations. Thus, Open and Covered experiments reflect the dynamics of the two regions far away from the sea ice edge.

## 3.2 Sea ice thermodynamics

The evolution of sea ice over time is studied in Fig. 3.2. Sea ice concentration is defined as the areal fraction of a grid cell covered by sea ice. Sea ice concentration is initialized to 0 in the open ocean region and 1 in the ice-covered region of the domain. The Hovmöller diagram of sea ice concentration shows the along-edge sea ice concentration average over time for the first 5 days (left figure in Fig. 3.2). The system takes few hours to start to form new sea ice in the open ocean region. Sea ice percentage concentration and sea ice thickness in the across edge direction are plotted for different days (center and right figures in Fig. 3.2). In the ice-free region, far from the ice-edge, sea ice concentration reaches almost 70% in 1 day and 90% in 10 days. The reduction in sea ice concentration along the ice edge can be explained by the interaction with the new sea ice formation in the covered region. Sea ice thickness is initially zero in the open ocean and 2 m in the ice-covered ocean. Then, it increases in open waters up to 7 cm in 1 day, 35 cm in 10 days and exceeds half a meter in 20 days. In the ice-covered region in 20 days sea ice grows slowly another 5 cm.

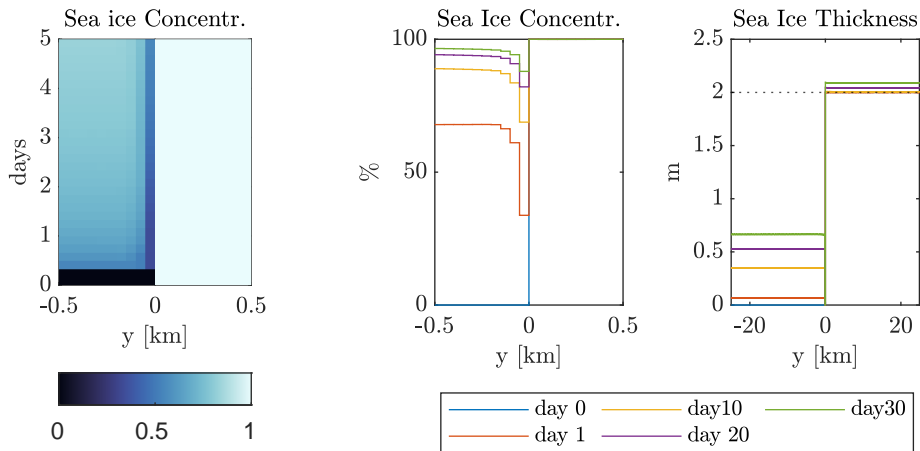


Figure 3.2: Sea ice cover evolution for Standard 3D simulation. Hovmöller diagram of sea ice concentration (left). Sea ice concentration percentage averaged over the along-edge direction (center). Zonal average sea ice thickness (right).

### 3.3 Characterization of the dynamics

When fronts form in the ocean, they can become unstable. In a mixed-layer front, this often leads to the genesis of submesoscale eddies. They are visible as vortical coherent structures that appear both at the surface and in the interior of the ocean mixed-layer (ML). These structures can transport tracer properties of the water masses, such as temperature, salinity, density, energy. In the brine driven winter Arctic Ocean, submesoscale eddies are energized and transport by salinity (and density) features. At the surface a front can be detected from the sea surface height, that is a consequence of horizontal density gradients and geostrophic currents. Over time, when instabilities grow, the sea surface height exhibits wave-like features that break up the linearity of the initial front.

#### 3.3.1 Eddy visualization

The horizontal view of sea surface height is plotted in Fig. 3.3 for Standard 3D experiment. When the dense brine rejected in the open ocean region convects in the water column, it leads to the formation of a front along the ice-edge direction. The two water masses in the two areas of the domain with different densities force a pressure gradient that is balanced by an associated change in sea surface height, as a response to geostrophic currents.

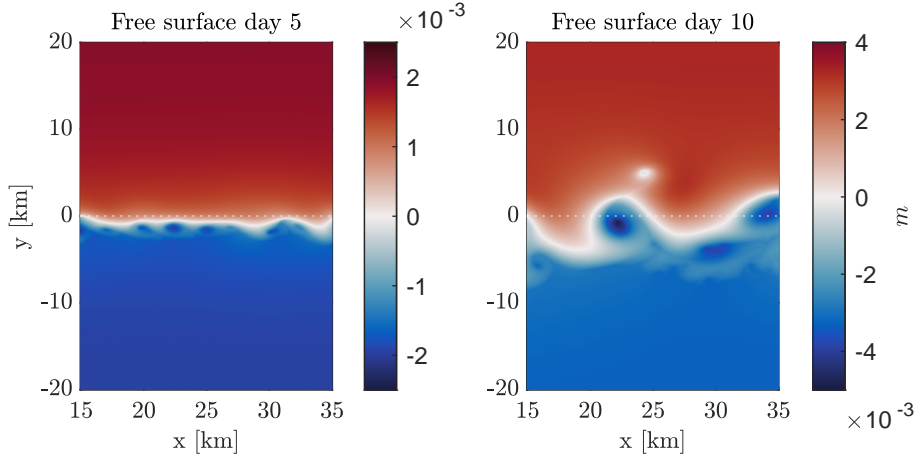


Figure 3.3: Horizontal view of the free surface displacement for the Standard 3D simulation at day 5 (left) and day 10 (right).

In the presence of sea ice,  $\eta$  is the level of the free-surface when all the sea ice is melt. The ocean surface pressure is equal to the pressure of both the sea surface height and the water mass from the melted ice. The equation that computes the potential pressure (2.11) sets the loading term only equal to the atmospheric pressure, that can be neglected, without considering the pressure exerted by sea ice in the ice-covered ocean, which is already counted as ocean pressure.

Initially, the free-surface is at rest, with zero displacement everywhere. It rapidly evolves to adjust to the horizontal density gradients, which create overturning currents and subsequent geostrophic currents, lowering the water in the ice-free region and lifting up the water in the ice-covered region. As the instabilities grow,  $\eta$  begins to meander (left in Fig. 3.3). Over time, density increases due to the continual brine rejection, increasing the buoyancy gradient, the associated sea surface height gradients, and the eddy energy (right figure). Coherent vortical structures become "finite amplitude" by 5 days. Note the different color bars in Fig. 3.3.

The salinity anomaly from the initial condition can also be used to track the formation and size of eddies in the domain. Fig. 3.4 shows the horizontal view of salinity at day 10 at -11.25 m depth (i.e. at cell level located at -10, -12.5 m) and at the mixed-layer base (vertical cell located at -22.5, -25 m). The color range values are taken to be the same for the two vertical layer considered, in order to compare the eddy strength with depths. At day 10, surface eddies (Fig. 3.3) and eddies at

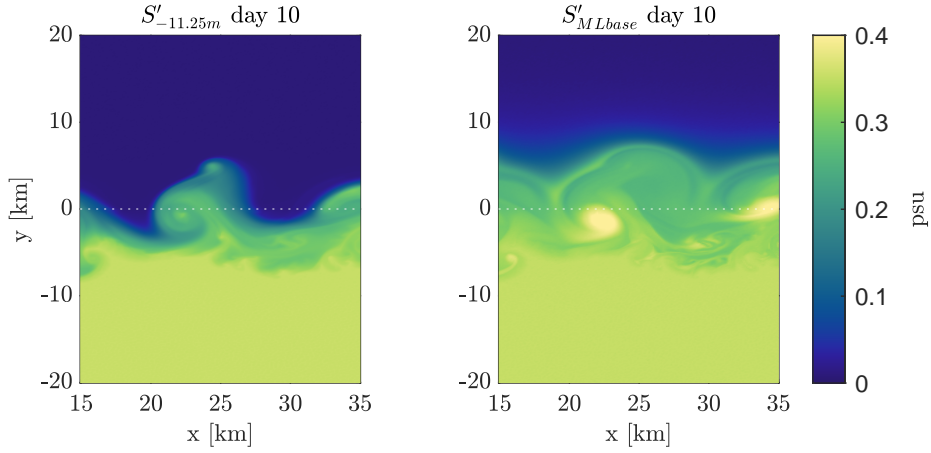


Figure 3.4: Horizontal view of salinity anomaly from initial condition for the Standard 3D simulation at two depths at day 10.

mid-depth in the ML (left in Fig. 3.4) have similar size. Eddies are bigger at the ML base (right in Fig. 3.4) where they are more effective in transporting saltier water to the ice-covered region. Their size reaches few kilometers in 10 days and keeps growing.

### 3.3.2 Surface velocity field

The ocean in the domain is initially at rest, but flows develop when the front is formed. It is interesting to look at the surface velocities that grow when density anomalies from the initial state are established. Fig. 3.5 shows the horizontal view of the surface velocities at day 5 and day 20 superimposed on the density field. Note that left and right figures have different axis and density ranges. Surface velocities act over a structured density field and move water parcels around bringing properties and giving shape to complex vortical structures.

Here, a consideration need to be made. Surface quantities are not perfectly quantities that are located at the surface considered as the interface between the ocean and the atmosphere. The displacement of the free-surface, in fact, changes the volume of water in the upper grid cells, that are taken as fixed. Thus, the surface properties of the upper grid cells do not always refer to the same volume of mass below the free-surface. But, since the free-surface elevation is negligible with respect to the cell thickness, this approximation can be made.

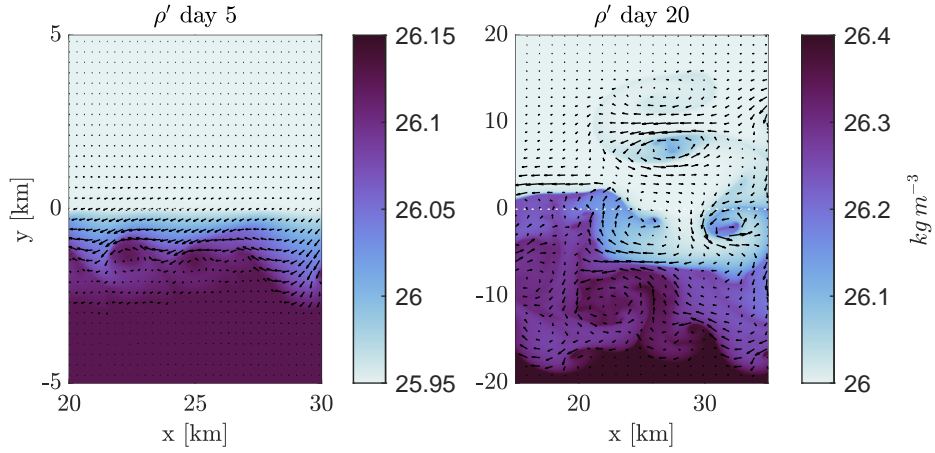


Figure 3.5: Horizontal view of surface velocities (arrows) superimposed on density anomalies (colors) at day 5 and at day 20 for the Standard 3D simulation.

At day 5 the surface density is higher in the ice-free region with a smooth gradient from the sea ice interface toward the far open ocean. As expected, the velocities are smaller far away from the ice-edge and are bigger in the open ocean region near the ice-edge. Although small, velocities in the ice-covered region are directed toward the negative  $y$ -direction, pushing the lighter water underneath sea ice above the denser water in the other region. This is exactly the behaviour of a gravitational slumping front, where light water flows above the dense water, in an attempt to restratify the ocean. Here, however, the Coriolis force is drifting the  $y$ -negative surface flow toward the negative  $x$ -direction. This is visible in the open ocean region close to the ice-edge. There, instabilities affect the surface flow which oscillates in the negative  $x$ -direction.

At day 20 eddies are present. The surface velocities are greater along eddies, and in fact, as will be seen later, the eddies bring more kinetic energy than the mean flow. It can be noted that the lighter water of the ice-covered surface region has not effectively moved into the open surface ocean. This is due to two mechanisms. First, the velocities are directed toward the negative  $x$ -direction in order to balance the pressure force, as established by the geostrophic adjustment, preventing the front to slump under gravity. Secondly, brine rejection is not stopped but continues to inject high density into the open ocean domain, canceling the lighter water coming from the right.

## 3.4 Effect of brine rejection

The ocean response to the surface cooling can be investigated by analyzing the paths of the high density intrusions into the ocean mixed-layer. Equivalently to density, the variable here studied is the buoyancy, since it directly enters the energy and potential vorticity equations. Apart from the magnitude and the dimensions, density can be immediately obtained from buoyancy, simply reverting the sign. As already mentioned, it is interesting to look at density and buoyancy anomalies from initial condition. Positive signs of buoyancy anomaly indicates density decrease, while negative signs density increase.

### 3.4.1 Buoyancy evolution

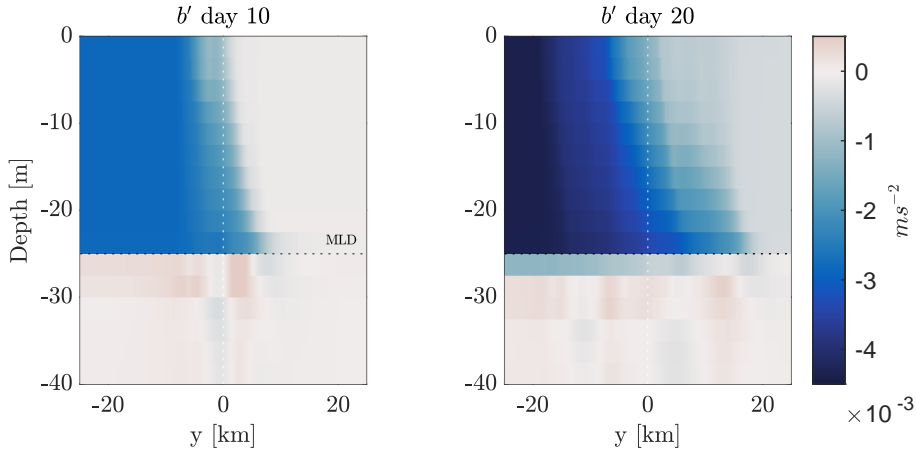


Figure 3.6: Buoyancy anomaly from its initial value for the Standard 3D simulation plotted as averaged in the along-edge direction at day 10 (left) and 20 (right).

First, the buoyancy anomaly evolution is visualized in Fig. 3.6 that shows the along ice-edge vertical distribution in the across-edge direction of the high density, which is injected mainly into the open ocean region and to a smaller extent into the ice-covered region, at days 10 and 20 for the Standard 3D simulation. The color range is the same for the left and right figures. In the ice-covered domain, brine rejection is much important for day 20 than day 10, as noted from the salinity surface fluxes in Fig. 3.1. In the open ocean region, although the salinity surface fluxes are lowering in time, high density is continually formed and added to the already formed high density, as visible in the far left region in the right figure. In the open ocean region close to the ice-edge the buoyancy is higher, for both the

presence of surface flows from the lighter region and the existence of submesoscale eddies. The initially well defined frontal interface rapidly evolves into higher complexity with many different horizontal gradients at different depths. Moreover, the geostrophic adjustment problem is complicated by the continuing supply of brine, that leads to an evolving triangular dense water structure propagating under the ice.

The mixed-layer base does not perfectly prevent the intrusion of high density water below it, especially when the density of the mixed-layer becomes higher and higher, as visible for 20 days run. This intrusion at day 20 is a consequence of the adjustment of the mixed-layer base to the water characteristics. Here, this happens with the widening of the pycnocline region. In the interior ocean bands of denser and lighter waters spread rapidly far away from the  $y = 0$  position and propagate down from the grid cell right below the halocline (day 10). However, almost all of the high density water remains in the mixed-layer. One can wonder how the ML base evolves in time. Although the halocline jump is deepening, the peak of the maximum density anomaly is always located at the grid cell right above the initial halocline, at -25 m. The net effect of entrainment of high density water below the ML is enlarging the pycnocline region. For this reason, in this work, the ML depth is kept constant and located at -25 m.

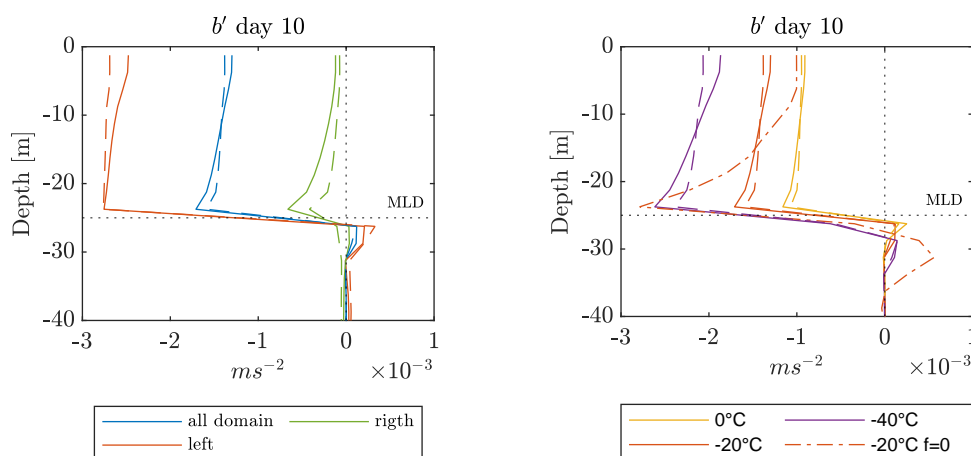


Figure 3.7: Vertical profiles of buoyancy anomaly from initial state at day 10. On the left, ice-free region (red) and ice-covered region (green) for Standard 3D buoyancy profiles. On the right, comparison between experiments:  $T_{air} = 0^\circ\text{C}$  (yellow),  $-20^\circ\text{C}$  (red),  $-40^\circ\text{C}$  (purple). Solid lines for 3D simulations, dashed lines for 2D simulations, and dash-dotted line for Nof simulation.

Differences in the ice-covered and ice-free regions are enhanced in Fig. 3.7 (solid lines in the left figure), where the vertical buoyancy anomaly profile at day 10 is divided into the left (ice-free) and the right (ice-covered) regions. Due to brine rejection, the ice-free region is subjected to a density increase, much larger than the one in the ice-covered region. Below the ML base, there is a small blob of lighter density anomaly only in the ice-free region. The ML buoyancy is vertically distributed to place denser water at the base of the mixed layer and lighter water near the surface.

The comparison between different run experiments is, first, examined through the buoyancy vertical profiles evolution for the different simulations, Fig. 3.7. On the left, solid lines refer to the Standard 3D experiment, while dashed lines to the Standard 2D experiment. In the two-dimensional case, the front is steeper and there is less propagation of dense water into the right region along the base of the mixed-layer. The difference between two and three-dimensional configurations is also visible in the figure on the right. There, different external atmospheric temperature simulations are also compared. Lower the air temperature, greater the cooling and the brine rejection. Moreover, greater the atmospheric forcing, faster the slump of the front. This may happen because when the potential energy stored in the front is bigger, more of this energy can be converted to slump the front, and, at the same time, more energetic submesoscale eddies form rapidly. The effect of the submesoscale eddies, in fact, can be seen by looking at the difference between the two and three-dimensional configurations. In the three-dimensional configuration, where submesoscale eddies are present, denser water is located at the base and lighter water above it, leading to a front that is more tilted, or, in other words, tending to restratify more effectively the ML. The Nof experiment, instead, shows a front more tilted at day 10. The absence of the Earth rotation rapidly slumps the front under the gravity force.

Another way to compare different experiments is through the Hovmöller diagrams. The upper panel in Fig. 3.8 shows the Hovmöller diagrams of the zonal mean ML average buoyancy anomaly for the Nof, Standard 2D and Standard 3D simulations with the same  $T_{air} = -20^{\circ}\text{C}$ . The ML average is here analyzed in order to study the whole behaviour of ML. It has to be said that the total vertical column average has, apart from the magnitude, almost the same Hovmöller diagram of the buoyancy anomaly, since, as already seen, the buoyancy changes in the interior ocean is roughly negligible. However, an interesting question may be what happen at different depths in the ML. Different vertical levels of the ML are not characterized by the same horizontal density gradients rate of change, as shown by Fig. 3.6. They would have slightly different Hovmöller diagrams, but

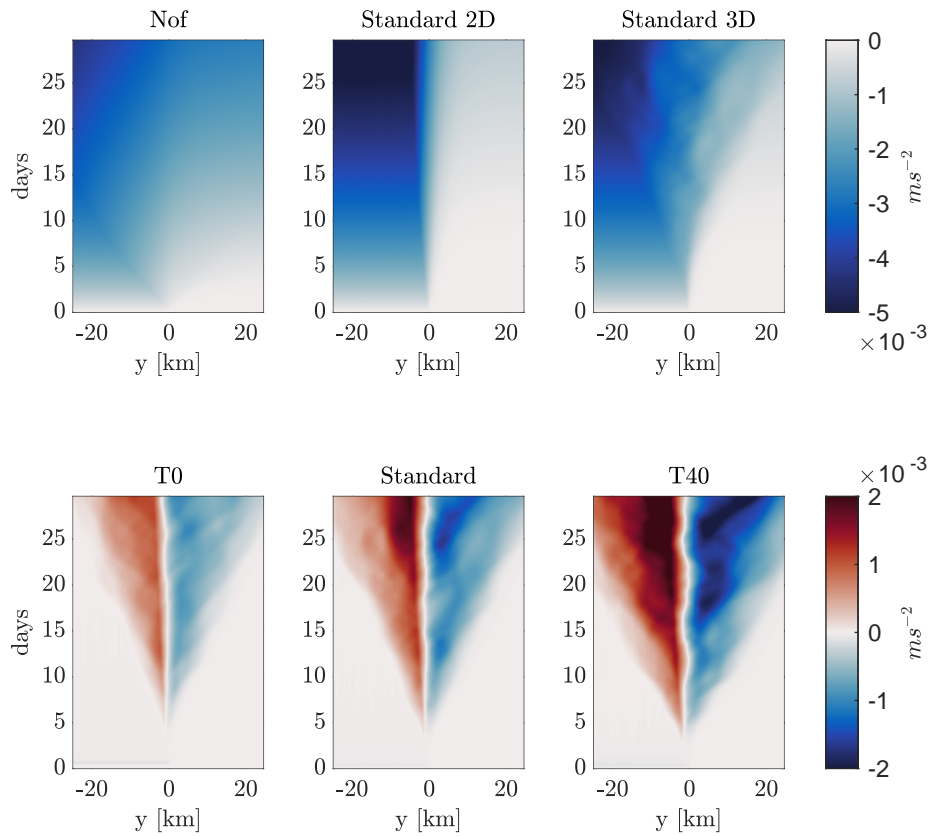


Figure 3.8: Hovmöller diagrams of ML average buoyancy anomaly from initial state averaged in the along-edge direction for simulations at same  $T_{air} = -20^\circ\text{C}$  (top panels). Hovmöller diagrams of ML buoyancy anomaly of 3D simulations against 2D simulations for different air temperatures (bottom panels).

the comparison between different forcing using different experiments would lead to the same conclusion. In general, the trend is to spread salinity from the denser part of the ocean, the left region, toward the lighter ocean, the right domain. The absence of the Earth rotation simply allows the gravitational slump of the front and restratifies rapidly the ML. The two-dimensional configuration presents a smooth intrusion of dense water to the right of the ice-edge, as more brine is rejected. Horizontal gradients become smooth, a sign of frontal slump that is in geostrophic balance. Until day 5, the three-dimensional configuration has almost the same distribution of buoyancy in the ML as the two-dimensional configuration. However, after 5 days, it becomes much different, with not a well defined interface between the two fluids and eddy-like blobs that transport properties from one region to the other. It is only far from the ice-edge that the buoyancy doesn't change from the two-dimensional case. The overall effect of submesoscale eddies is to slump the front more rapidly.

The difference between three and two-dimensional configurations is well represented by the lower panel in Fig. 3.8, which shows the 3D anomaly from the respective 2D experiment for different air temperatures. The 3D anomaly from 2D buoyancy highlights the effect of submesoscale eddies at a ML front. For the Standard simulation ( $T_{air} = -20^\circ\text{C}$ ), they start to develop from day 5, that is the time they need to reach finite amplitude instabilities, at the frontal interface, that is where baroclinic instability forms, and grow over time reaching bigger and bigger sizes. As they grow, they are more effective in moving properties of water masses around. In particular, they displace denser water from the ice-free region into the ice-covered region and do the opposite with lighter water. In this way, they enhance the restratification mechanism.

In general, higher the external atmospheric forcing, greater the horizontal density gradients, stronger the front, faster the slumping. This not only happens for the simple two-dimensional case, but it also helps the restratification process driven by submesoscale eddies. In fact, for  $T_{air} = -40^\circ\text{C}$ , eddies start to form earlier and grow to bigger size than in the  $T_{air} = -20^\circ\text{C}$  case.

The ML frontal slump is quantitatively studied in Fig. 3.9 (left). Solid lines represent Standard 3D experiment and dashed lines Standard 2D experiment. Over time, the front becomes more tilted, but the furthest regions from the sea ice edge maintain the same buoyancy as the two-dimensional case. Moreover, over time, also the ice-covered region is becoming denser, as can be noted by the lowering of the buoyancy in the right region. This is, again, a confirmation of the brine rejection phenomenon below the 2 meters-thick ice.

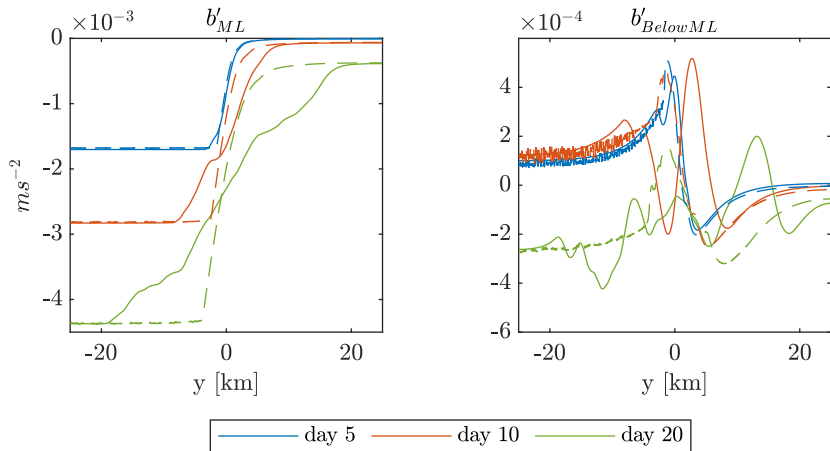


Figure 3.9: ML zonally averaged buoyancy anomaly evolution for Standard 3D (solid lines) and 2D (dashed lines) simulations (left). Same with buoyancy average below the ML.

On the right in Fig. 3.9, there is the zonal average buoyancy anomaly for three vertical layers right below the ML, from -32.5 to -25 m. The wave-like feature response is visible for both two-dimensional and three-dimensional configurations. Again, however, the magnitude of the buoyancy anomaly below the ML base is much smaller than above it.

### 3.4.2 Stratification

Mean buoyancy gradient  $\nabla b$  is here analyzed in its two components, the vertical stratification  $N^2 = \partial b / \partial z$  and the correspondent horizontal gradient  $M^2 = \partial b / \partial y$ . Their vertical mean average for Standard 3D simulation is plotted in Fig. 3.10 over time. The stratification  $N^2$  decreases in the open ocean region since denser water is injected at the oceanic surface and falls at the base of the ML. Brine is rejected also in the ice-covered region but with a slower rate. The across front horizontal buoyancy gradient is many orders of magnitude lower than the vertical stratification and is higher only in the frontal region. The vertical distribution of the anomaly of  $N^2$  from its initial value is represented in Fig. 3.11 for the Standard 3D simulation at day 1 and day 10.  $N^{2'}$  is negative, since  $N^2$  is decreasing, and  $|N^{2'}|$  increases in time at the base of the ML. The overall time evolution of  $N^{2'}$  for Standard 3D, Standard 2D and Nof experiments is compared in Fig. 3.12. The stratification is driven by the brine rejection rate which is the same for all the simulations considered, but it evolves in time accordingly to the strength of

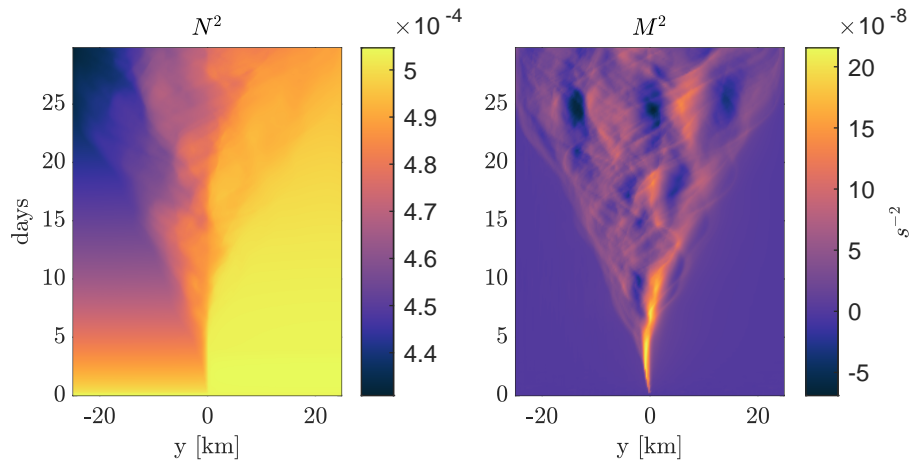


Figure 3.10: Hovmöller diagrams for vertically averaged  $N^2$  and  $M^2$  for the Standard 3D simulation.

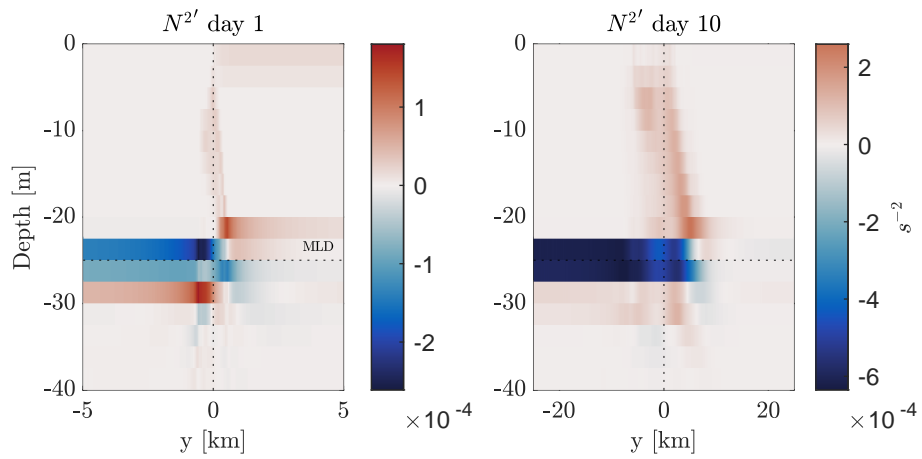


Figure 3.11: Anomaly of stratification for Standard 3D simulation at day 1 (left) and day 10 (right).

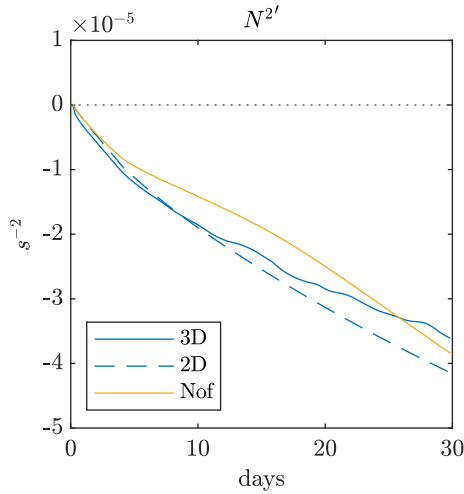


Figure 3.12: Comparison of mean stratification anomaly for Standard 3D, Standard 2D and Nof experiments.

the restratification process in the three experiments. Fig. 3.12 confirms that the two-dimensional configuration is less effective in restratifying the ML, MLEs that develops in three-dimensional configurations starts to restratify the ML after 10 days, and the Nof simulation restratifies more rapidly the mixed-layer.

### 3.5 Geostrophic currents

A current in the across-ice-edge direction is soon established to bring lighter water above denser water. This overturning current tends to restratify the ocean mixed-layer. However, as a response to the across-ice-edge velocity, a geostrophic current develops in the along-ice-edge direction and balance the horizontal gradient of the pressure potential. Of course, this happens only in the rotational case. When  $f = 0$ , no zonal currents develop and the across-ice-edge velocity is enhanced. The rotational and non rotational currents at day 1 are shown in Fig. 3.13. The Standard 2D case is very similar to the Standard 3D experiment, especially for earlier times when eddies are not formed yet. Over time, the zonal velocity overcomes the magnitude of the y-velocity.

The horizontal variability of U and V currents at day 1 is shown in Fig. 3.14, which is the result of the geostrophic adjustment. The y-velocity, V, is pushing lighter water above denser water. These currents, opposite at the surface and the bottom of the ML, trigger a current in the perpendicular direction, U. Also the

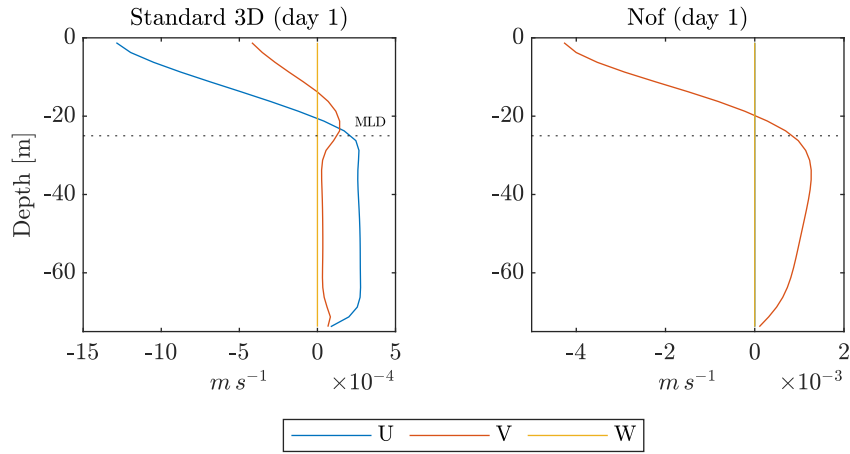


Figure 3.13: Zonal mean vertical profiles of velocities in the x, y and z direction (U, V, W) at day 1 for the Standard 3D simulation (left) and Nof simulation (right).

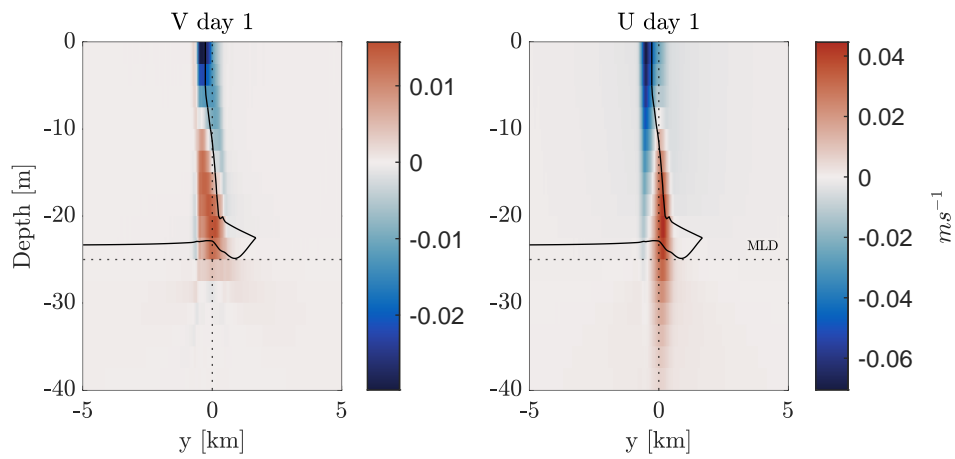


Figure 3.14: Zonal mean horizontal velocities at day 1 for the Standard 3D simulation. The black line is buoyancy anomaly contour  $b' = -2 \times 10^{-4} ms^{-2}$ .

U currents have opposite direction at the top and the bottom of the ML. They travel along the sea ice edge, reinforcing instabilities toward bigger size and, thus, eddies. Over time, as V moves far from the ice-edge, also the U velocity spatial distribution broadens. They increase magnitude in time and deepen below the mixed-layer.

### 3.6 Potential vorticity dynamics

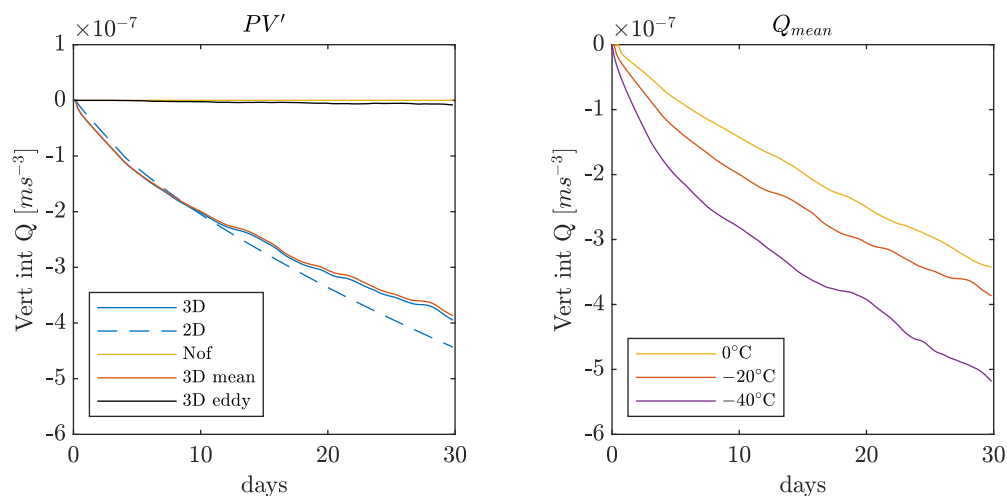


Figure 3.15: Vertically integrated horizontally average PV anomaly from initial condition.  $\bar{Q}$  and its terms  $Q_{mean}$  and  $Q_{eddy}$  for  $T_{air} = -20^\circ\text{C}$  (left). Comparison of  $Q_{mean}$  for different experiments (right).

Due to vorticity and buoyancy gradient correlation, the Ertel potential vorticity (PV) is a key quantity in frontal dynamics:

$$Q = (\boldsymbol{\omega} + \mathbf{f}) \cdot \nabla b \quad (3.1)$$

In the presence of a buoyancy source term, as during brine rejection, PV is not conserved (see Sec. 2.3.4 and equation (2.32)): negative buoyancy injection implies negative PV injection. This is clearly visible in Fig. 3.15 where the domain-averaged vertically integrated Ertel PV anomaly from initial condition is computed. For the non rotating experiment PV anomaly is zero, since, although there is injection of brine, the absence of both planetary and relative vorticity, for the absence of transverse velocity, sets to zero the PV (3.1). For  $f \neq 0$  PV decreases in time, for both three and two-dimensional configurations, in the same way  $N^{2'}$

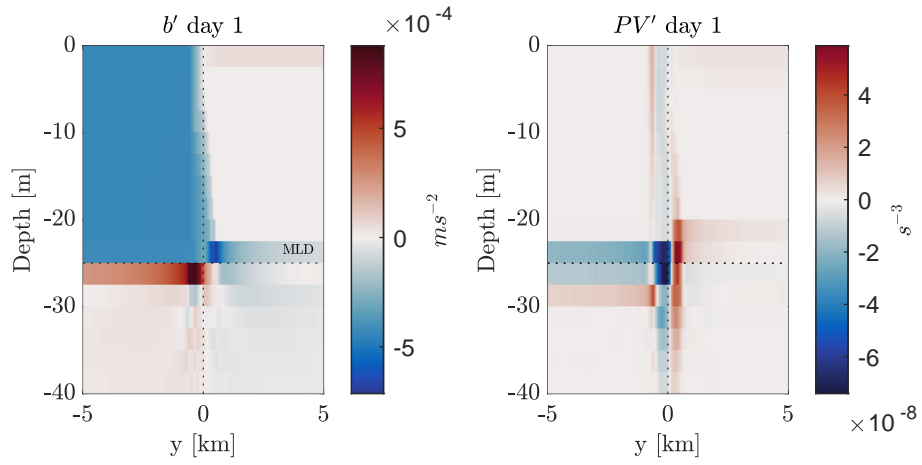


Figure 3.16: Zonally average buoyancy (left) and PV (right) anomalies from initial condition at day 1 for the Standard 3D simulation.

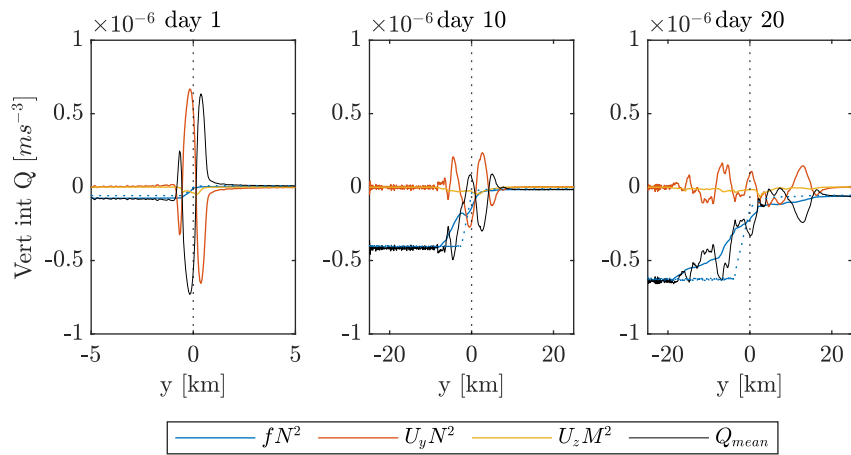


Figure 3.17: Vertically integrated zonally average  $Q_{mean}$  anomaly terms for Standard 3D (solid lines) and 2D ( $fN^2$ , dotted blue lines) at day 1, 10 and 20.

does. The difference between three and two-dimensional experiments, which appears after 10 days, is due to frictional stresses, since the injection of buoyancy is the same. Friction appears to be interesting in three-dimensional configurations, where eddies drive more restratification, increasing  $\nabla b$  in (2.32).

When dividing the zonally averaged PV terms into  $Q_{mean}$  and  $Q_{eddy}$ , the full non linear PV is well described just by the zonally averaged variables, with  $Q_{eddy}$  almost negligible:

$$\begin{aligned}\bar{Q} &\approx Q_{mean} = (f - \bar{u}_y)\bar{b}_z + \bar{u}_z\bar{b}_y \\ &= fN^2 - U_yN^2 + U_zM^2\end{aligned}\tag{3.2}$$

where  $N^2 = \bar{b}_z$  and  $M^2 = \bar{b}_y$  are vertical and horizontal buoyancy gradients. The main driver of PV is the stratification  $N^2$ , which is not affecting  $Q_{eddy}$ . This result simplifies the description of the problem: in order to predict the PV dynamics, only the mean quantities are necessary.

The injection of PV is governed by salinity fluxes, that are determined by the air temperature, Fig. 3.15 (right).

Fig. 3.16 shows buoyancy anomaly and PV anomaly distributions at day 1 for the Standard 3D simulation. PV is injected at the surface, but it is accumulated only at the base of the ML and at the interface between the two regions' fluids.

The vertically integrated PV anomaly at day 1 is plotted in the left panel in Fig. 3.17, which represents the mean terms of  $Q_{mean}$ , as in (3.2), for the Standard 3D simulation. The dotted blue line represents the  $fN^2$  term for the Standard 2D case; the other components for the two-dimensional experiment are not plotted, since they are not interestingly different from the three-dimensional ones and their fluctuations would only cover the three-dimensional lines.

First, the  $U_zM^2$  term is almost zero, meaning that the horizontal buoyancy gradients don't affect PV, and the bigger component of buoyancy gradient and relative vorticity in (3.1) are in the vertical direction. The planetary vorticity is effective only in the open ocean region at the base of the ML, where vertical gradients of buoyancy are bigger and locally there is unstable stratification  $N^2 < 0$ . The relative vorticity is active starting from the interface  $y = 0$ , where the slump of the front creates vertical buoyancy gradients. Initially, the planetary vorticity effect in the PV is smaller than the high relative vorticity originating at the interface, since the small amount of buoyancy injected in 1 day doesn't create strong gradient at the ML base.

Over time (Fig. 3.17), the negative buoyancy accumulated in the ML grows, and, with it, the buoyancy gradient at the ML base in the open ocean region strengthens, decreasing  $fN^2$ .

Again, the difference between two and three-dimensional experiments is enhanced after 10 days, once eddies are big. Indeed, the three-dimensional stratification (solid blue line) in the left region is more effectively spread away from the ice-edge position  $y = 0$  than the two-dimensional one (dotted blue line). At the same time,  $U_y N^2$  lowers its magnitude as spreading away from the interface, being effective mostly in the ice-covered region, and  $U_z M^2$  is always negligible. For long time scales, the injection of PV released from brine rejection is mainly governed by

$$\bar{Q} \approx Q_{mean} \approx fN^2 \quad (3.3)$$

and it is the presence of submesoscale eddies that spreads away PV along the ML base toward the left, a signal of frontal slumping.

To conclude,  $|PV|$  increases mainly in the open water region and travels away from the ice-edge due to  $fN^2$ ; while a smaller blob of PV, due to  $U_y N^2$ , travels in the covered ML region.

### 3.7 Energetics

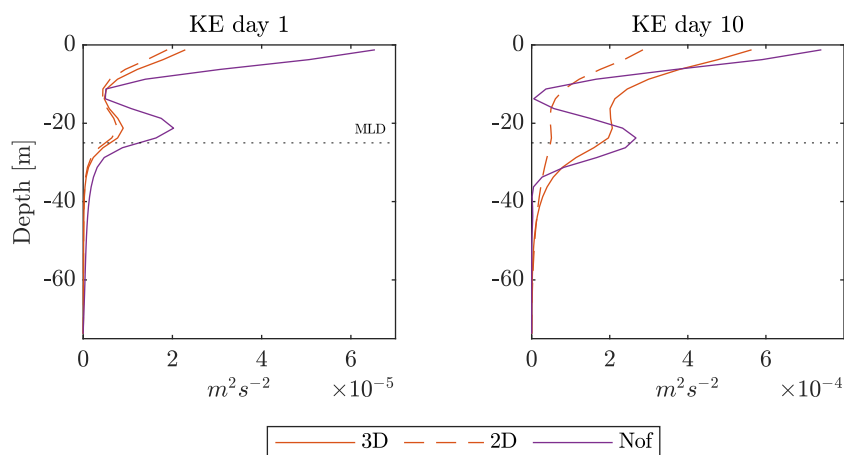


Figure 3.18: Horizontally averaged kinetic energy profiles at day 1 and day 10 for Standard 3D (solid red lines), Standard 2D (dashed red lines), Nof (purple lines).

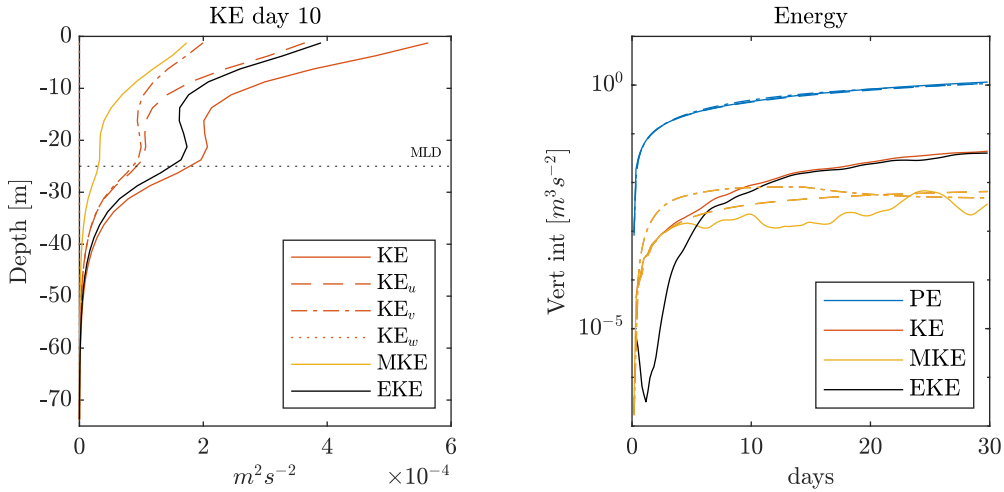


Figure 3.19: On the left: horizontally averaged kinetic energy profiles at day 10 for Standard 3D experiment divided into the different components. On the right: time evolution of vertically integrated horizontally averaged potential and kinetic energy terms for Standard 3D experiment (solid lines), Standard 2D experiment (dashed lines) and Nof case (dash-dot lines).

Vertical profiles of horizontally average kinetic energy for  $T_{air} = -20^\circ\text{C}$  at day 1 and day 10 are plotted in Fig. 3.18. Notably, the kinetic energy has two peaks, one at the surface and one at the ML base, which correspond to the layers of maximum velocities. Indeed, the light water is pushed from the ice-covered region toward the denser region above the dense water that moves in the opposite direction at the base of the ML. Even when geostrophic currents are generated, they are enhanced at the same depths of the currents in the across-ice-edge direction. Initially, three and two-dimensional configurations have almost the same kinetic energy. When eddies form, the EKE departs from the MKE, deviating the total kinetic energy from the two-dimensional configuration. Eddies, also, over time, become more energetic than the simple gravitational frontal slump in the absence of the Earth rotation.

Vertical profile of kinetic energy at day 10 for the Standard 3D simulation is deeply analyzed in the left panel of Fig. 3.19. The kinetic energy is first divided into its x, y and z components. The vertical component of kinetic energy is, as expected, negligible; there is no convection due to vertical velocity, just parametrized convective adjustment, which doesn't affect the resolved vertical velocity. Then, the kinetic energy is separated into mean kinetic energy (MKE) and eddy kinetic energy (EKE) terms. At day 10 EKE is bigger than MKE, driving, as already

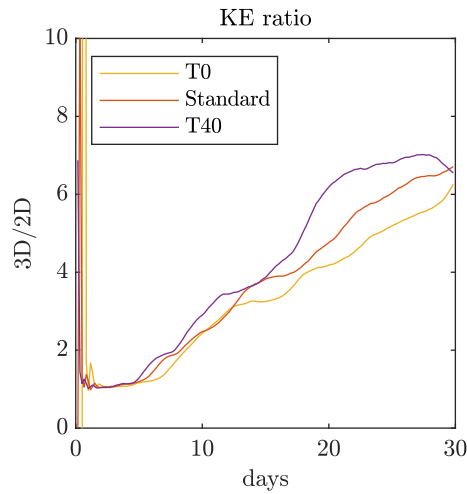
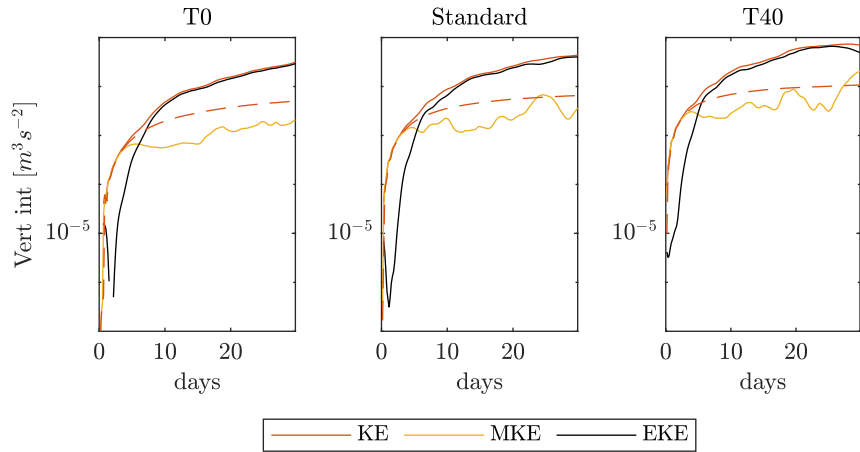


Figure 3.20: An the top: time evolution of total kinetic energy for T0, Standard and T40 simulations. Solid lines refer to 3D simulations; dashed lines to 2D simulations. An the bottom: total kinetic energy ratio between 3D and 2D experiments versus time for T0, Standard and T40 experiments.

said, the departure from the two-dimensional configuration.

The time evolution of the energy terms is studied through Fig. 3.19 and 3.20. The right panel in Fig. 3.19 shows the time evolution for the total potential energy (blue line), the total vertically integrated and horizontally averaged kinetic energy and its MKE and EKE components, of the system driven by  $T_{air} = -20^\circ\text{C}$ . Solid lines refer to the Standard 3D experiment, dashed lines to the Standard 2D experiment and the dash-dot lines to the Nof experiment. The potential energy is the same for the three experiments, since it depends only on the total negative buoyancy injected into the system, which is governed by surface fluxes. It grows as brine is rejected. MKE matches KE for two-dimensional configurations, since there are no eddies driving the EKE. The kinetic energy is more effectively extracted from the front in the  $f = 0$  case, where the more tilt in the front transfers energy to currents. In the Nof experiment, however, currents are, then, soon calmed, when the front has already slumped. Finally, the three-dimensional case is even different. When eddies grow, they create EKE that grows in time. Moreover, the EKE grows at the expense of the MKE, which in fact is lowered than the two-dimensional one. At about 10 days the total kinetic energy is only due to submesoscale eddies.

The upper panel in Fig. 3.20 compares the time evolution of kinetic energy terms for different external temperatures. The behaviour is very similar; however, the magnitude of kinetic energy depends on the external forcing, which also controls the rate at which EKE is created. It can be noted that at increases in MKE corresponds decreases of EKE, since the two are related through the shear production terms that have opposite sign in the two energy budgets (see equations (2.40) and (2.41); this will be further discussed later in this section).

In order to study the overall effect of eddies in the energetics of the brine driven system and the role of external forcing, the ratio between three-dimensional and two-dimensional total kinetic energy versus time is plotted in the lower box in Fig. 3.20. First, the kinetic energy ratio increases in time during the experiment run period, confirming that the High stratification chosen as initial condition prevents sinks of energy into the ocean interior. Secondly, the differences between external forcing effects are enhanced as time grows. At day 10 the 3D kinetic energy has reached twice the kinetic energy of the 2D experiment. At day 20 the ratio reaches 4 and it overcomes 6 in 30 days.

The EKE budget in (2.41) is studied by analyzing the buoyancy production

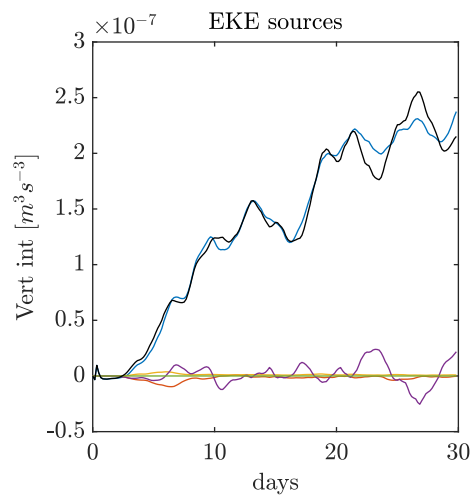
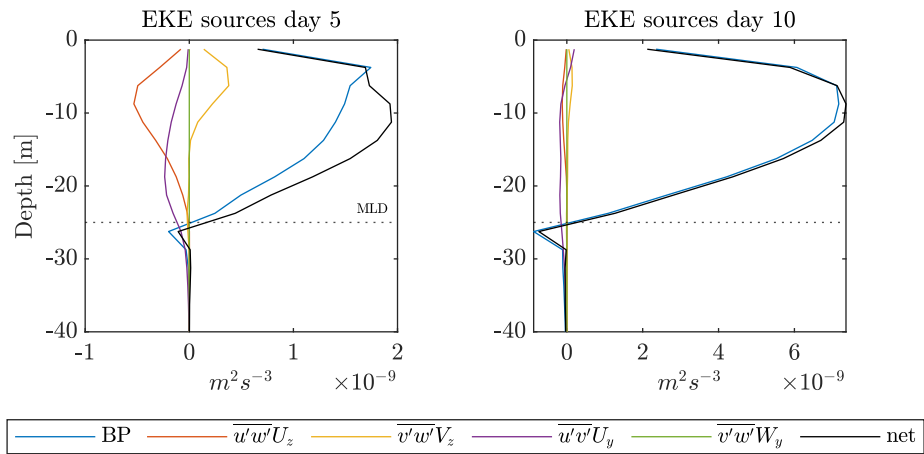


Figure 3.21: EKE buoyancy production (BP), shear production source terms and their net effect for the Standard 3D experiment.

and the shear production terms separately:

$$BP = \overline{w'b'} \quad (3.4)$$

$$SP = \overline{u'v'} U_y + \overline{u'w'} U_z + \overline{v'w'} V_z + \overline{v'w'} W_y \quad (3.5)$$

Fig. 3.21 shows the vertical profiles and the vertically integrated time evolution of these terms and their net effect, counting them with their relative signs. Notably, the buoyancy production drives the EKE formation. In baroclinic instability problems, most of the energy comes from the conversion of potential energy into eddy kinetic energy and eddy potential energy (see equation (A.4)). BP has a positive sign in the ML, where submesoscale eddies act to restratify the ML; it has a negative sign below the ML where the water is locally stable. While BP increases in time, shear production terms are always present with almost the same magnitude over time. However, among them, the  $W_y$  term is negligible, while, on average over time, the bigger one is  $\overline{u'v'} U_y$ . This term oscillates in time, causing, due to its negative effect (see equation (2.41)), an opposite oscillation in the net source terms of EKE. This, exactly, confirms and explains why the upper plots in Fig. 3.20 have an oscillating MKE opposite to EKE: the two energy budget equations are related through the shear production term which is alternately bringing energy from the mean flow to the eddy flow and viceversa.

### 3.8 Eulerian and eddy overturning streamfunctions

Here, the overturning streamfunction introduced in Sec. 2.3.6 is studied. The overturning circulation is due both to the mean circulation and the eddy circulation, which act to tilt the front.

The eddy overturning streamfunction (2.47) can be computed from the eddy buoyancy fluxes. The Eulerian and eddy overturning streamfunctions,  $\Psi_E$  and  $\Psi^*$ , at days 5 and 10, are plotted in Fig. 3.22.  $\Psi_E$  is computed integrating the zonally average  $V$  velocity:

$$\Psi_E = \int_{-H}^z \bar{v} dz \quad (3.6)$$

where the bottom  $z = -H$  is chosen as reference, so that  $\Psi_E(z = -H) = 0$ .  $\Psi^*$ , which is due to eddy buoyancy fluxes and mean buoyancy gradient, is computed using the horizontal buoyancy fluxes

$$\Psi^* = -\frac{\overline{v'b'}}{\bar{b}_z} \quad (3.7)$$

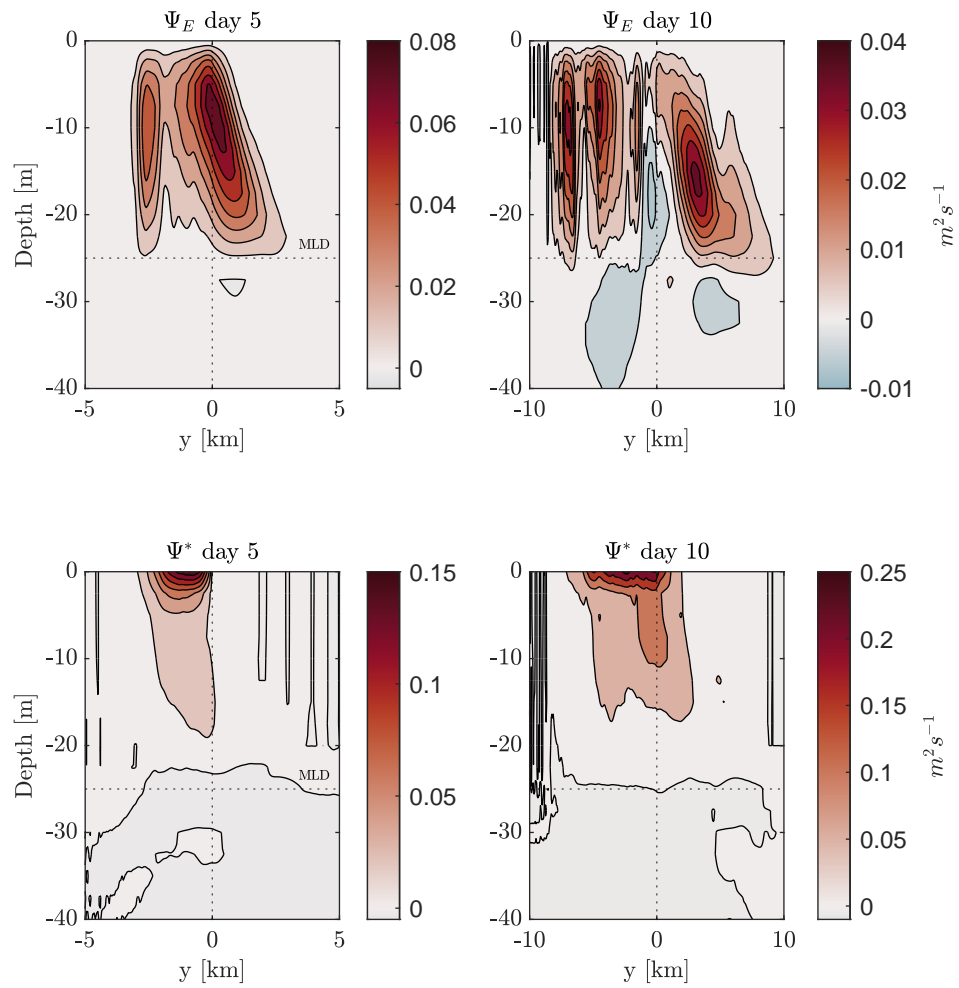


Figure 3.22: Eulerian overturning streamfunction (upper figures) and eddy overturning streamfunction (lower figures) at days 5 and 10 for the Standard 3D simulation.

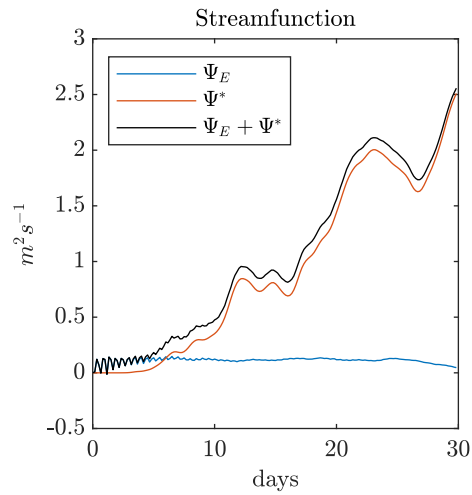


Figure 3.23: Domain average Eulerian, eddy and residual overturning streamfunctions versus time for the Standard 3D simulation.

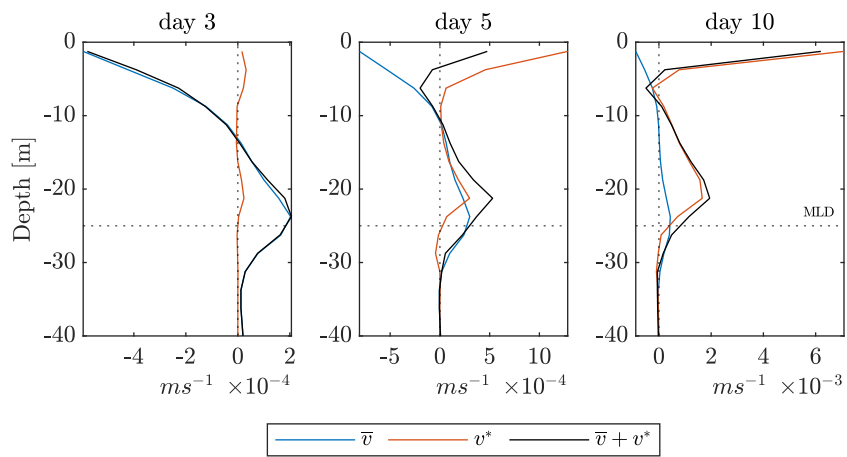


Figure 3.24: Vertical profiles of Eulerian, Bolus and residual meridional velocities at days 3, 5 and 10 for the Standard 3D simulation.

This is because the horizontal buoyancy gradient  $\bar{b}_y$  is so small compared to  $\overline{w'b'}$  in the open ocean region, leading to blowup in the streamfunction computation. Both the two streamfunctions are predominately positive, indicating that the two circulations act in the same direction and work together to flat the isopycnals. However, the magnitude of the streamfunction is very different: initially, the Eulerian streamfunction is higher than the eddy one; later, when eddies become important they become the main driver of the residual overturning circulation.

This is also visible in Fig. 3.23 which shows the average streamfunction value in the domain for the two circulation and their sum. Clearly, initially, the residual streamfunction  $\Psi_{res} = \Psi_E + \Psi^*$  is only given by  $\Psi_E$ , but, as soon as submesoscale eddies form, it is mainly given by  $\Psi^*$ . Moreover, the eddy overturning streamfunction increases in time, with a rate of change that doubles in 10 days.

Finally, from the eddy overturning streamfunction the Bolus velocity can be computed as

$$v^* = \frac{\partial \Psi^*}{\partial z} \quad (3.8)$$

and compared to the zonally averaged across-edge velocity  $\bar{v}$ . Again, initially the residual velocity  $v_{res} = \bar{v} + v^*$  coincides with the Eulerian velocity, while it starts to deviate at day 5 and it is completely overlapping the Bolus velocity at day 10.

### 3.9 Lateral density transfer scale analysis

In theories of frontal adjustment the lateral density transfer length scale is an important parameter that is related to and predicts the eddy size length scale. Here the scaling proposed by *Matsumura and Hasumi* [2008] for the refreezing lead is analyzed in a single sea ice edge system and compared to the observed length scale of lateral density transfer. The typical length scale in geostrophic adjustment processes is the Rossby deformation radius

$$L_d = \frac{NH}{f} = \frac{\sqrt{\Delta b H}}{f} \quad (3.9)$$

where  $H$  is the mixed-layer depth and  $\Delta b$  is the buoyancy difference between the two sides of the front. As already said in Sec. 1.7, *Matsumura and Hasumi* [2008] suggest a scaling for the deformation radius based on buoyancy conservation in the domain, and find a length scale  $\propto t^{1/2}$  or  $t^{1/3}$  accordingly to the ratio between  $L_d$  and the opening width (1.27). When applied to this study, it is found that the

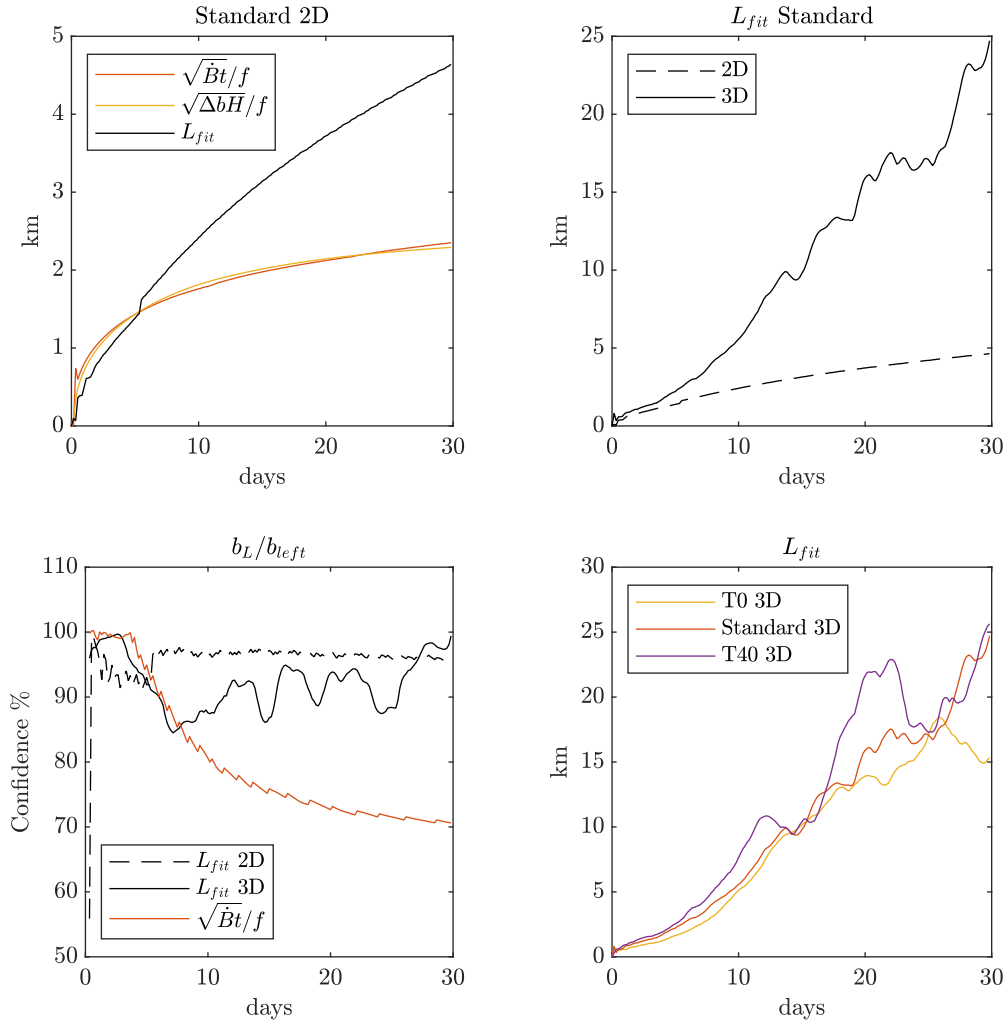


Figure 3.25: Upper left: deformation radius using *Matsumura and Hasumi* [2008] (red line), common definition (yellow line) and the measured lateral density transfer distance  $L_{fit}$  (black line) for Standard 2D experiment. Upper right:  $L_{fit}$  for Standard 2D and 3D cases. Bottom left:  $b_L/b_{left}$  as a measure of confidence level. Bottom right:  $L_{fit}$  for Standard, T0, T40 simulations.

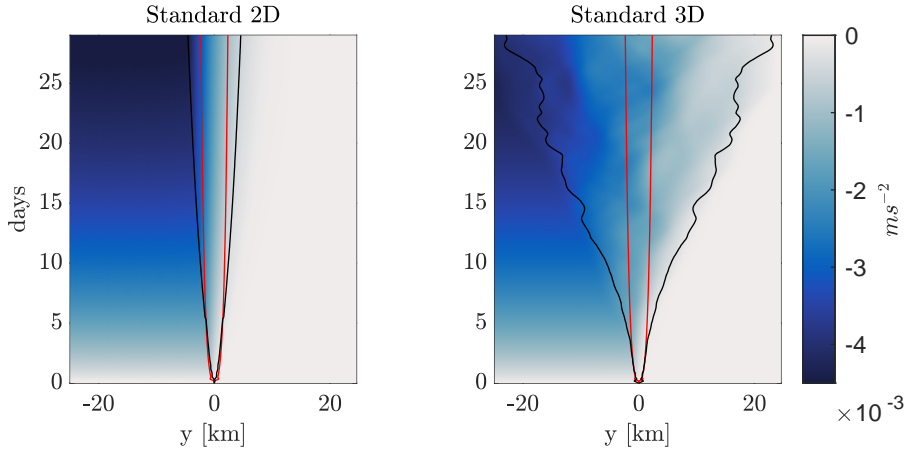


Figure 3.26: Deformation radius (red line) and measured lateral transfer distance  $L_{fit}$  (black line) for Standard 2D (left) and Standard 3D (right) simulations.

valid scaling is

$$L_d = \frac{\sqrt{\dot{B}t}}{f} \quad (3.10)$$

where  $\dot{B}$  is the buoyancy flux at the surface, measured in  $\text{m}^2\text{s}^{-3}$  and computed as

$$\dot{B} = \frac{g}{\rho_0 [\text{gm}^{-3}]} \dot{S} \quad (3.11)$$

with  $\dot{S}$  the surface fluxes of salinity ( $\text{g m}^{-2} \text{s}^{-1}$ ). Although the buoyancy flux is variable in time,  $L_d$  in (3.10) is still  $\propto t^{1/2}$ . This scaling is compared with the deformation radius in (3.9). Since in the frontal region it is difficult to point out the stratification  $N^2$  which gives different  $L_d$  for different choices, the  $\Delta b$  formula is here used. In particular,  $\Delta b$  is computed as the difference between the two symmetric averaged ML areas with respect to the ice edge. Although the frontal spin-down affects the buoyancy in the two regions, in the two-dimensional configuration this method is not introducing error since isopycnals are almost vertical. The mixed-layer depth is considered constant. The scaling in (3.9) and (3.10) gives the same deformation radius measure for two-dimensional simulations. The comparison is plotted in the left upper panel in Fig. 3.25 for the Standard 2D simulation.

In order to estimate the realistic deformation radius in frontal adjustment processes, the simulated ML average buoyancy field is fitted with an exponential or

a linear behaviour. The typical length scale of the fit is then used to track the intrusion of dense water at the base of the ML. Here, it is observed that both the linear and the exponential fits give the same length scale. This fact is expected since the frontal region is symmetrically distributed between the two regions and in the fit the extremes of the frontal region are taken symmetrically with respect to  $y = 0$ . The frontal slump is well described by a linear behaviour also in the three-dimensional configuration, where eddies are enhanced.

A consideration has to be made: since brine rejection happens also in the ice-covered region, the frontal adjustment process is affected by a combination of overturning processes from the two sides of the front. In order to simplify the analysis, the ice-covered far right ML average buoyancy field is subtracted from the buoyancy in the whole domain. This procedure is not affecting the comparison between the two methods, as long as the buoyancy difference in (3.9) is computed as  $\Delta b(t) = \overline{b_{ML,covered}}(t) - \overline{b_{ML,open}}(t)$  with a time variable ice covered ML buoyancy  $b_{ML,covered}$ .

Upper left panel in Fig. 3.25 shows also the time evolution of the typical distance indicated as  $L_{fit}$  for the Standard 2D experiment. After 5 days, the typical frontal spin-down distance departs from the deformation radius law proposed by *Matsumura and Hasumi* [2008]. The three-dimensional front tilts more rapidly than the two-dimensional one, as visible in Fig. 3.25 (upper right). The bottom left plot in Fig. 3.25 shows the ratio  $b_L/b_{left}$  between the value of ML buoyancy at distance  $L$  from the ice edge in the open ocean region and the ML buoyancy at the far left boundary, for  $L$  equal to  $L_{fit}$  and  $L_d$  in (3.10). Both 2D and 3D Standard simulations are shown. The ratio  $b_L/b_{left}$  is a measure of the confidence of the deformation radius scaling. The realistic  $L_{fit}$  is located at the distance at which the density varies of about 95% or 90% (for 2D and 3D experiments, respectively); the classical deformation radius instead is not well representing the spread of the front after 5 days, for both two and three-dimensional configuration. The front is spreading faster than expected also in the geostrophic adjusted front.

Higher forcing implies a faster spread, although in the three-dimensional case oscillations appear in the solution after 15 days due to the interaction between big eddies and with the domain boundaries (bottom right in Fig. 3.25).

A visualization of the Hovmöller diagram of the ML buoyancy and the observed lateral transfer distance (black line) and the deformation radius (red line) is plotted in Fig. 3.26 for the Standard 2D and 3D simulations. The far right buoyancy has been already subtracted.

This result urges to find an explanation for the different behaviour, not only in the more complex agesotrophic submesoscale context but also in the geostrophic adjustment process. A diffusion process that enhances the restratification has to be considered.

# Conclusion

In this work the wintertime refreezing of an open ocean area near a sea ice edge has been studied through idealized high resolution numerical simulations. The hydrostatic version of the Massachusetts Institute of Technology general circulation model (MITgcm) [Marshall *et al.*, 1997] has been used. Sea ice thermodynamics has been modeled with the two-layer sea ice thermodynamic package of the MITgcm model [Winton, 2000]. The ocean model domain is a square channel of 50x50 km initially equally divided in an open ocean part and a sea ice covered region. The control experiment of a three-dimensional configuration forced by an external air temperature of  $-20^{\circ}\text{C}$  is compared with the analogous two-dimensional configuration, its non rotating case and higher and lower forcing experiments with air temperatures of  $-40$  and  $0^{\circ}\text{C}$ , respectively.

Due to the temperature difference between air and ocean, heat fluxes are established. Since the oceanic temperature is already near freezing, new sea ice forms, causing salt fluxes by rejecting dense brine into the ocean mixed-layer (ML). Simulations show that brine rejection is weaker, but still present, in the initially ice-covered region. Density increases especially in the open ocean area and is immediately vertically mixed throughout the ML by convective adjustment. A buoyancy front grows at the sea ice edge and undergoes gravitational overturning, with velocities at the surface and the bottom of the ML acting in opposite directions. As a response to jet formation, along sea ice edge currents with the same opposite behaviour are geostrophically adjusted. Baroclinic instabilities develop into mixed-layer eddies (MLEs), also called submesoscale eddies, which are allowed only in three-dimensional simulations. It is observed that submesoscale eddies grow in 5 days and totally dominate the dynamics after 10 days. Since the Coriolis effect can not be neglected at high latitudes, the restratification mechanism of an ice-edge front is controlled by MLEs.

Brine rejection at the oceanic surface also injects negative potential vorticity (PV) into the ocean, which settles at the base of the ML, being mainly driven by the mean stratification  $N^2$ . MLEs drive faster restratification of the ML, lowering

$|PV|$  in the frontal region. In the non rotating case, instead, this can not happen due to the absence of vorticity in the flow.

The energetics of the system is studied decomposing total kinetic energy into mean kinetic energy (MKE) and eddy kinetic energy (EKE). TKE peaks at the surface and the bottom of the ML, where jets are established. In the control experiment, EKE and MKE becomes comparable in 5 days and the total kinetic energy is perfectly equal to EKE at day 10. Turbulent kinetic energy budget is dominated by the buoyancy production term  $\overline{w'b'} > 0$ , that leads the ML restratification.

The effect of submesoscale eddies in the frontal spin-down process is also studied by comparing the Eulerian overturning streamfunction with the eddy overturning streamfunction. For the control experiment, after 5 days, the eddy overturning streamfunction is of the same order of magnitude of the Eulerian one, and it completely drives the slumping after 10 days.

An important length scale to describe the frontal spin-down problem is the distance at which the dense-enriched water intrudes into the buoyant water at the ML base. In geostrophic adjustment problem the typical distance is determined by the Rossby deformation radius  $L_d = NH/f = \sqrt{\Delta b H}/f$ . Through buoyancy conservation, *Matsumura and Hasumi* [2008] scale the typical buoyancy transfer length as  $\propto t^{1/2}$  or  $t^{1/3}$ , accordingly to the relative size of  $L_d$  with respect to the opening length. Here, it is found that the scaling proposed by *Matsumura and Hasumi* [2008] holds for initial times up to 3 days, with a faster rate for increasing times, when used in two-dimensional configurations. The transfer rate is further increased when MLEs are present. This can be explained assuming that a diffusive ageostrophic process increases the spread of lateral transfer at longer times. Note that *Matsumura and Hasumi* [2008] adopt a lead configuration with maximum width of 800 m, artificially close the opening after 1, 3 or 10 days and prove the  $t^{1/3}$  scaling. The difference in geometry and time scales between their configuration and the present study can explain why they didn't observe this diffusion.

The comparison between external forcing strength reveals that a higher forcing drives faster and larger submesoscale eddies and larger frontal density transfer length scale, although after 15 days the interaction of eddies with the domain boundaries can not be neglected and affects the solution.

In the present study the Arctic Ocean has been idealized and some assumptions have been made. The wind driven circulation has not been considered. This is suitable for weak winds, although it is estimated that winds will likely be more

important in the future reduced Arctic sea ice cover. For future studies, it would be interesting to explore the interaction of a sea ice edge front with a spiraling flow in the Ekman layer. Winds can impress a mechanical stress also on sea ice dynamics, though sea ice drift is not expected for sufficiently thick and compact sea ice cover that may be connected to land. For the time scales considered in this work it is possible to assume that sea ice is governed by thermodynamics. Also oceanic waves have not been considered and the ocean is initially at rest. The interactions with waves can importantly affect the ML restratification; they could more efficiently spread properties laterally or break up submesoscale eddies toward dissipation. Oceanic waves also move sea ice, that is transported toward the Atlantic Ocean on long time scales. The coupling with ocean surface waves is a target for future work. In the present study, atmospheric freshwater fluxes, such as precipitation, are omitted.

To conclude, the present work has explored some theoretical tools that can be used to investigate the oceanic response at a refreezing sea ice edge. Reynolds decomposition helped in dividing into mean and turbulent features and in observing their relative magnitude. Here, it has been confirmed that MLEs rapidly enhance the restratification process by subtracting energy from the mean flow and increasing the turbulent kinetic energy of a brine driven ocean at a sea ice edge. Finally, through the length scale analysis, a new process emerges after several days both in simple geostrophic adjustment of an overturning front and, even more strongly, when submesoscale eddies are energized and drive restratification of the mixed-layer and lateral transport – ageostrophic diffusion. This diffusive process spreads the frontal region and its typical size departs from the scaling proposed by *Matsumura and Hasumi* [2008]. Therefore, submesoscale eddies can be more important than expected in high latitude seas. Future studies can help in further investigating the process. At last, the present work will help in understanding the more complex system of two interacting sea ice edge fronts at a refreezing lead, that will be the objective of future study. Key questions in the brine driven lead problem will be the relationship of submesoscale energetics and the lateral spread of density to the length scales of the lead problem, notably lead width and the ML depth.

# Appendix A

## Derivation of MLE parametrization

The derivation of the MLE parametrization follows *Fox-Kemper et al.* [2008].

Let's consider the general diabatic Boussinesq mean buoyancy equation (where  $\nabla \cdot \mathbf{u} = 0$ ):

$$\frac{D\bar{b}}{Dt} = \frac{\partial \bar{b}}{\partial t} + \nabla \cdot \bar{\mathbf{u}}\bar{b} + \nabla \cdot \overline{\mathbf{u}'b'} = \bar{\mathcal{D}} \quad (\text{A.1})$$

where  $\mathcal{D}$  is the diabatic term.

The potential energy per unit area can be computed as

$$\begin{aligned} PE &= \frac{1}{A} \int_A \int_{-H}^{\eta} \rho g z \, dx dy dz \\ &= \frac{1}{A} \int_A \left[ \int_{-H}^{\eta} \rho_0 g z dz - \int_{-H}^{\eta} \rho_0 b z dz \right] dx dy \\ &= \frac{1}{A} \int_A \rho_0 \left[ \frac{1}{2} g (\eta^2 - H^2) - \int_{-H}^{\eta} b z dz \right] dx dy \end{aligned} \quad (\text{A.2})$$

and subtracting the initial value and dividing per  $\rho_0(H + \eta) \approx \rho_0 H$  gives

$$\langle PE \rangle = -\langle bz \rangle + \left\langle \frac{1}{2H} g \eta^2 \right\rangle \quad (\text{A.3})$$

where  $\langle \cdot \rangle$  represents the  $xyz$  average. In the frontal spindown problem the potential energy is extracted by the submesoscale eddies ( $\bar{w}\bar{b} \ll \overline{w'b'}$ ) and the potential energy variations are related to the vertical buoyancy eddy fluxes:

$$\frac{d\langle PE \rangle}{dt} = -\frac{d}{dt} \langle z'b' \rangle = -\langle w'b' \rangle \quad (\text{A.4})$$

A parametrization for the vertical buoyancy flux  $\overline{w'b'}$  is needed. First, the PE release due to baroclinic instability can be represented by the exchange of fluid parcels over a decorrelation distance  $(\Delta y, \Delta z)$  in  $\Delta t$ :

$$\frac{d\langle PE \rangle}{dt} \approx \frac{\Delta PE}{\Delta t} \propto \frac{\Delta z \Delta b}{\Delta t} \quad (\text{A.5})$$

By writing the buoyancy variation as coming from the vertical and the horizontal displacement

$$\Delta b = \Delta y \frac{\partial \bar{b}}{\partial y} + \Delta z \frac{\partial \bar{b}}{\partial z} \quad (\text{A.6})$$

and using the proportionality between the slope of the fluxes and the isopycnal slope

$$\frac{\Delta y}{\Delta z} \propto \frac{-\frac{\partial \bar{b}}{\partial z}}{\frac{\partial \bar{b}}{\partial y}} \quad (\text{A.7})$$

it remains only the horizontal buoyancy gradient in the vertical restratification process:

$$\langle w'b' \rangle \propto \frac{\Delta z \Delta y \frac{\partial \bar{b}}{\partial y}}{\Delta t} \quad (\text{A.8})$$

The time scale  $\Delta t$  is the turnover time for the eddies  $\Delta t = \Delta y / \mathcal{V}$ , where  $\mathcal{V}$  is the eddy velocity scale.  $\mathcal{V}$  is of the same order of magnitude as the mean horizontal velocity, i.e. the thermal wind velocity:  $\mathcal{V} \propto U \approx -\frac{H}{f} \frac{\partial \bar{b}}{\partial y}$ , using the vertical constrain  $\Delta z \propto H$ . Finally the vertical buoyancy eddy flux scales with

$$\langle w'b' \rangle \propto \frac{H^2}{|f|} \left( \frac{\partial \bar{b}}{\partial y} \right)^2 \quad (\text{A.9})$$

and it is set to be positive definite, with the absolute value of  $f$  taken to extract PE in both hemispheres, thus placing dense water under light water and slumping the front.

In analogy, using the same consideration above, a scaling for the horizontal eddy fluxes can be obtained:

$$\begin{aligned} \overline{w'b'} &\propto \frac{H^2}{|f|} (\nabla_H \bar{b})^2 \\ \overline{v'b'} &\propto -\frac{H^2 \frac{\partial \bar{b}}{\partial z}}{|f|} \nabla_H \bar{b} \end{aligned} \quad (\text{A.10})$$

Vertical eddy fluxes are upward, they restratify the ML extracting PE. Horizontal eddy fluxes are down the mean horizontal buoyancy gradient.

Eddies effect is largely adiabatic. Thus, they can be represented by an overturning streamfunction. The eddy fluxes are related to this streamfunction and the mean buoyancy gradient:

$$\overline{\mathbf{u}'b'} \equiv \Psi \times \nabla \bar{b} \quad (\text{A.11})$$

or equivalently

$$\begin{aligned} \overline{v'b'} &= -\Psi \bar{b}_z \\ \overline{w'b'} &= \Psi \bar{b}_y \end{aligned} \quad (\text{A.12})$$

where the indices stand for partial derivative in the given direction and with

$$\Psi \propto \frac{H^2}{|f|} \nabla \bar{b} \times \hat{\mathbf{z}} \quad (\text{A.13})$$

Note that, due to the perpendicularity of the horizontal mean buoyancy gradient to the vertical direction, the overturning streamfunction is only in the along-front direction. It represents the overturning of the front. The final form of the overturning streamfunction is found to be (FK08):

$$\Psi = C_e \frac{H^2 \mu(z)}{|f|} \nabla \bar{b} \times \hat{\mathbf{z}} \quad (\text{A.14})$$

with  $C_e = 0.06 - 0.08$  the efficiency factor and  $\mu(z)$  the vertical structure function

$$\mu(z) = \left[ 1 - \left( \frac{2z}{H} + 1 \right)^2 \right] \left[ 1 + \frac{5}{21} \left( \frac{2z}{H} + 1 \right)^2 \right] \quad (\text{A.15})$$

This parametrization produces fluxes as in (A.11) and an eddy induced velocity, called Bolus velocity:

$$\mathbf{u}^* = \nabla \times \Psi \quad (\text{A.16})$$

# Appendix B

## Derivation of the Ertel PV equation

The equation for the Ertel potential vorticity (PV) is obtained from the momentum equations and the buoyancy equation in the Boussinesq approximation:

$$\frac{D\mathbf{u}}{Dt} + \mathbf{f} \times \mathbf{u} = -\nabla\phi + b\hat{\mathbf{k}} + \mathcal{F} \quad (\text{B.1})$$

$$\frac{Db}{Dt} = \mathcal{D} \quad (\text{B.2})$$

where  $\mathcal{F}$  are frictional forces,  $\mathcal{D}$  diabatic forcing, and the material derivative is  $\frac{D}{Dt} = \frac{\partial}{\partial t} + \mathbf{u} \cdot \nabla$ . Moreover, in the Boussinesq system  $\nabla \cdot \mathbf{u} = 0$ . In this work,  $\mathbf{f} = f\hat{\mathbf{k}}$  with  $f$  constant.

By taking the curl of the L.H.S in (B.1) and using the rule  $\mathbf{u} \cdot \nabla \mathbf{u} = \frac{1}{2}\nabla(\mathbf{u}\mathbf{u}) - \mathbf{u} \times (\nabla \times \mathbf{u}) = \nabla(\mathbf{u}\mathbf{u}) + \boldsymbol{\omega} \times \mathbf{u}$  with  $\boldsymbol{\omega} = \nabla \times \mathbf{u}$  the relative vorticity, one gets

$$\begin{aligned} \nabla \times \left( \frac{D\mathbf{u}}{Dt} + \mathbf{f} \times \mathbf{u} \right) &= \frac{\partial \boldsymbol{\omega}}{\partial t} + \nabla \times [(\boldsymbol{\omega} + \mathbf{f}) \times \mathbf{u}] \\ &= \frac{\partial \boldsymbol{\omega}}{\partial t} + \mathbf{u} \cdot \nabla(\boldsymbol{\omega} + \mathbf{f}) - (\boldsymbol{\omega} + \mathbf{f}) \cdot \nabla \mathbf{u} \end{aligned} \quad (\text{B.3})$$

Finally, (B.1) becomes

$$\frac{D(\boldsymbol{\omega} + \mathbf{f})}{Dt} = (\boldsymbol{\omega} + \mathbf{f}) \cdot \nabla \mathbf{u} + \nabla \times b\hat{\mathbf{k}} + \nabla \times \mathcal{F} \quad (\text{B.4})$$

The equation for the buoyancy gradient can be obtained taking the gradient of from (B.2)

$$\nabla \frac{Db}{Dt} = \nabla \frac{\partial b}{\partial t} + \nabla(\mathbf{u} \cdot \nabla b) = \frac{\partial \nabla b}{\partial t} + \mathbf{u} \cdot \nabla(\nabla b) + \nabla b \cdot \nabla \mathbf{u} \quad (\text{B.5})$$

which gives

$$\frac{D\nabla b}{\partial t} = \nabla \frac{Db}{Dt} - \nabla b \cdot \nabla \mathbf{u} = \nabla \mathcal{D} - \nabla b \cdot \nabla \mathbf{u} \quad (\text{B.6})$$

To combine (B.4) and (B.6), the dot-product with  $\nabla b$  and  $(\boldsymbol{\omega} + \mathbf{f})$ , respectively, is taken:

$$(\nabla b) \cdot \frac{D(\boldsymbol{\omega} + \mathbf{f})}{Dt} = \nabla b \cdot [(\boldsymbol{\omega} + \mathbf{f}) \cdot \nabla \mathbf{u}] + \nabla b \cdot (\nabla \times \mathcal{F}) \quad (\text{B.7})$$

$$(\boldsymbol{\omega} + \mathbf{f}) \cdot \frac{D\nabla b}{\partial t} = (\boldsymbol{\omega} + \mathbf{f}) \cdot \nabla \mathcal{D} - \nabla b \cdot [(\boldsymbol{\omega} + \mathbf{f}) \cdot \nabla \mathbf{u}] \quad (\text{B.8})$$

Summing up (B.7) and (B.8), the equation for the Ertel PV is obtained:

$$\frac{DQ}{Dt} = (\nabla \times \mathcal{F}) \cdot \nabla b + (\boldsymbol{\omega} + \mathbf{f}) \cdot \nabla \mathcal{D} \quad (\text{B.9})$$

where  $Q$  is the Ertel PV defined as

$$Q = (\boldsymbol{\omega} + \mathbf{f}) \cdot \nabla b \quad (\text{B.10})$$

Finally, (B.9) can be simply written in a conservation form

$$\frac{\partial Q}{\partial t} = -\nabla \cdot \mathbf{J} \quad (\text{B.11})$$

by introducing a flux of PV

$$\mathbf{J} = \mathbf{u}Q - \mathcal{F} \times \nabla b - (\boldsymbol{\omega} + \mathbf{f}) \mathcal{D} \quad (\text{B.12})$$

PV evolves due to frictional and diabatic effects and it is redistributed through advective processes of PV.

For inviscid and adiabatic flows, Ertel PV is conserved ( $\frac{DQ}{Dt} = 0$ ), and this constraint is usefully used to solve easily problems, like in the quasi-geostrophic theory.

# Appendix C

## Derivation of MKE and EKE equations

Using the Reynolds decomposition rule

$$\mathbf{u} = \mathbf{U} + \mathbf{u}' \quad (\text{C.1})$$

where  $\bar{\mathbf{u}} \equiv \mathbf{U}$  and the  $\overline{(\ )}$  stands for the average value such that  $\overline{(\ )}' = 0$ , the average of the kinetic energy of a fluid can be decomposed into a kinetic energy of the mean and a kinetic energy of the perturbation:

$$\begin{aligned} \overline{KE} &= \frac{1}{2} \overline{u_i^2} = \frac{1}{2} \overline{u_i^2} + \frac{1}{2} \overline{(u')_i^2} \\ &\equiv MKE + EKE \end{aligned} \quad (\text{C.2})$$

with  $MKE = \frac{1}{2} \overline{u_i^2}$  the mean kinetic energy and  $EKE = \frac{1}{2} \overline{(u')_i^2}$  the turbulent kinetic energy.

Two governing equations for the rate of change of the two separate terms can be build starting from the momentum equation:

$$\frac{D\mathbf{u}}{Dt} + \mathbf{f} \times \mathbf{u} = -\nabla\phi + b\hat{\mathbf{k}} + \mathcal{F} \quad (\text{C.3})$$

written in the Boussinesq approximation with  $\mathbf{f} = f\hat{\mathbf{k}}$  with  $f$  constant, and where  $\mathcal{F}$  are frictional forces. Moreover, the material derivative is  $\frac{D}{Dt} = \frac{\partial}{\partial t} + \mathbf{u} \cdot \nabla$  and  $\nabla \cdot \mathbf{u} = 0$ .

The energy budget equation is obtained by multiplying (C.3) by the velocity. Since the coupling terms between the mean and the eddy kinetic energy are non

linear, the derivation here is made posing  $\mathcal{F} = 0$  and zero Coriolis force. In the Einstein notation, under these assumption, the momentum equation becomes

$$\frac{\partial u_i}{\partial t} + u_j \frac{\partial u_i}{\partial x_j} = -\frac{\partial \phi}{\partial x_i} + b \delta_{i3} \quad (\text{C.4})$$

Now, by decomposing each variable into the mean and the perturbation and taking the average, the momentum equation for the mean can be obtained. It gives:

$$\frac{\partial U_i}{\partial t} + U_j \frac{\partial U_i}{\partial x_j} = -\frac{\partial \bar{\phi}}{\partial x_i} + \bar{b} \delta_{i3} - \frac{\partial}{\partial x_j} \overline{u'_i u'_j} \quad (\text{C.5})$$

Thus, due to the non linearity of the advection term, the mean flow is not independent by the perturbation flow. By subtracting (C.5) to (C.4) the momentum equation for the perturbation is found to be:

$$\frac{\partial u'_i}{\partial t} + U_j \frac{\partial u'_i}{\partial x_j} + u'_j \frac{\partial U_i}{\partial x_j} + u'_j \frac{\partial u'_i}{\partial x_j} = -\frac{\partial \phi'}{\partial x_i} + b' \delta_{i3} + \frac{\partial}{\partial x_j} \overline{u'_i u'_j} \quad (\text{C.6})$$

The two momentum equations for the mean and the eddy flows have a common term that appears with opposite sign in the two momentum equations, indicating a transfer of momentum from the mean flow to the turbulent flow.

Now, by multiplying (C.5) for  $U_i$  and (C.6) for  $u'_i$ , and taking the average, after some manipulations, the two equations for MKE and EKE are found:

$$\frac{\partial}{\partial t} \left( \frac{1}{2} U_i^2 \right) + U_j \frac{\partial}{\partial x_j} \left( \frac{1}{2} U_i^2 \right) = -\frac{\partial}{\partial x_i} U_i \bar{\phi} + U_i \bar{b} \delta_{i3} - \frac{\partial}{\partial x_j} (\overline{u'_i u'_j} U_i) + \overline{u'_i u'_j} \frac{\partial U_i}{\partial x_j} \quad (\text{C.7})$$

$$\frac{\partial}{\partial t} \left( \frac{1}{2} \overline{(u'_i)^2} \right) + U_j \frac{\partial}{\partial x_j} \left( \frac{1}{2} \overline{(u'_i)^2} \right) = -\frac{\partial}{\partial x_j} \left( \frac{1}{2} \overline{(u'_i)^2 u'_j} \right) - \overline{u'_i u'_j} \frac{\partial U_i}{\partial x_j} - \frac{\partial}{\partial x_i} \overline{u'_i \phi'} + \overline{b' w'}$$

(C.8)

Finally, the MKE and EKE equations are

$$\frac{D^M}{Dt} (MKE) = -\frac{\partial}{\partial x_i} U_i \bar{\phi} + W \bar{b} - \frac{\partial}{\partial x_j} (\overline{u'_i u'_j} U_i) + \overline{u'_i u'_j} \frac{\partial U_i}{\partial x_j} \quad (\text{C.9})$$

$$\frac{D^M}{Dt} (EKE) = -\frac{\partial}{\partial x_j} \left( \frac{1}{2} \overline{(u'_i)^2 u'_j} \right) - \underbrace{\frac{\partial}{\partial x_i} \overline{u'_i \phi'}}_{PW} + \underbrace{\overline{b' w'}}_{BP} - \underbrace{\overline{u'_i u'_j} \frac{\partial U_i}{\partial x_j}}_{SP} \quad (\text{C.10})$$

where  $\frac{D^M}{Dt} = \frac{\partial}{\partial t} + U_j \frac{\partial}{\partial x_j}$  is the material derivative with respect to the mean flow. The linear Coriolis term and dissipation term can be now added to the equations. Again, the budget equations for the mean and the turbulent kinetic energy have

an identical and opposite term, the shear production term SP, indicating that the two energy evolves one against the other.

The study of the EKE can be made by analyzing the effect of each terms in the R.H.S. of (C.10). The pressure work term PW, the buoyancy production term BP, and the shear production term SP can be positive or negative depending on the structure of the stratification, the mean shear flow and the pressure. For example, the buoyancy production term is positive if the fluid unstably stratified, and negative if it is stably stratified. Indeed, if  $N^2 < 0$ ,  $\bar{b}_z < 0$ ; thus, if the parcel deviates toward the surface,  $w' > 0$ , it would find itself around denser parcels, creating  $b' > 0$ , for which  $\overline{w'b'} > 0$  and EKE is created by pushing lighter water above denser water.

# Acknowledgments

The present work is the result of one-year long collaboration with Prof. Baylor Fox-Kemper and Prof. Christopher Horvat at Brown University in the Department of Earth, Environmental, and Planetary Sciences (DEEPS). I would like to thank Prof. Baylor Fox-Kemper for supporting and trusting me, and for being not only an advisor in this work but also an excellent professor. I appreciated his ability in explaining very complex concepts in an extremely clear way. With his sense of humor, he made me feel comfortable since our first meeting. I want to thank also Prof. Christopher Horvat who patiently introduced me to the Arctic Ocean studies and to numerical modeling. He has always been available and taught me many things about scientific community and also about America. He constantly made me feel helpful. I have to thank also Prof. Nadia Pinardi. Her enthusiasm made me love oceanography. She has encouraged me in my studies and she gave me the opportunity to go to the US. She also supported me during this work. My final thanks go to Fox-Kemper research group, who welcomed me and gave me food for thought and suggestions both during my stay at Brown and after my return to Italy.

# Bibliography

- Aagaard, K., and E. Carmack, The Role of Sea Ice and Other Fresh Water in the Arctic Circulation, *Journal of Geophysical Research*, *94*, 14,485–14,498, doi:10.1029/JC094iC10p14485, 1989.
- Arrigo, K. R., Sea Ice Ecosystems, *Annual Review of Marine Science*, *6*(1), 439–467, doi:10.1146/annurev-marine-010213-135103, pMID: 24015900, 2014.
- Barber, D. G., et al., Selected physical, biological and biogeochemical implications of a rapidly changing Arctic Marginal Ice Zone, *Progress in Oceanography*, *139*, 122–150, doi:https://doi.org/10.1016/j.pocean.2015.09.003, overarching perspectives of contemporary and future ecosystems in the Arctic Ocean, 2015.
- Barthélemy, A., T. Fichefet, H. Goosse, and G. Madec, Modeling the interplay between sea ice formation and the oceanic mixed layer: Limitations of simple brine rejection parameterizations, *Ocean Modelling*, *86*, 141–152, doi:https://doi.org/10.1016/j.ocemod.2014.12.009, 2015.
- Bitz, C. M., and W. H. Lipscomb, An energy-conserving thermodynamic model of sea ice, *Journal of Geophysical Research: Oceans*, *104*(C7), 15,669–15,677, doi:https://doi.org/10.1029/1999JC900100, 1999.
- Boccaletti, G., R. Ferrari, and B. Fox-Kemper, Mixed Layer Instabilities and Restratification, *Journal of Physical Oceanography*, *37*(9), 2228 – 2250, doi:10.1175/JPO3101.1, 2007.
- Bodner, A. S., and B. Fox-Kemper, A Breakdown in Potential Vorticity Estimation Delineates the Submesoscale-to-Turbulence Boundary in Large Eddy Simulations, *Journal of Advances in Modeling Earth Systems*, *12*(10), e2020MS002,049, doi:https://doi.org/10.1029/2020MS002049, e2020MS002049 10.1029/2020MS002049, 2020.

- Brenner, S., L. Rainville, J. Thomson, and C. Lee, The evolution of a shallow front in the Arctic marginal ice zone, *Elementa: Science of the Anthropocene*, 8, 14,485–14,498, doi:10.1525/elementa.413, 2020.
- Brown, K. A., J. M. Holding, and E. C. Carmack, Understanding Regional and Seasonal Variability Is Key to Gaining a Pan-Arctic Perspective on Arctic Ocean Freshening, *Frontiers in Marine Science*, 7, 606, doi:10.3389/fmars.2020.00606, 2020.
- Bush, J. W. M., and A. W. Woods, Vortex generation by line plumes in a rotating stratified fluid, *Journal of Fluid Mechanics*, 388, 289–313, doi:10.1017/S0022112099004759, 1999.
- Bush, J. W. M., and A. W. Woods, An investigation of the link between lead-induced thermohaline convection and Arctic eddies, *Geophysical Research Letters*, 27(8), 1179–1182, doi:https://doi.org/10.1029/1999GL002314, 2000.
- Carpenter, J. R., and M.-L. Timmermans, Deep mesoscale eddies in the Canada Basin, Arctic Ocean, *Geophysical Research Letters*, 39(20), doi:https://doi.org/10.1029/2012GL053025, 2012.
- Collins, M., et al., *Long-term Climate Change: Projections, Commitments and Irreversibility*, pp. 1029–1136, Intergovernmental Panel on Climate Change, Cambridge University Press, United Kingdom, 2013a.
- Collins, S. N., R. S. James, P. Ray, K. Chen, A. Lassman, and J. Brownlee, Grids in Numerical Weather and Climate Models, in *Climate Change and Regional/Local Responses*, edited by Y. Zhang and P. Ray, chap. 4, IntechOpen, Rijeka, doi:10.5772/55922, 2013b.
- Csanady, G., *Circulation in the Coastal Ocean*, Environmental Fluid Mechanics, Springer Netherlands, 1982.
- D’Asaro, E. A., Observations of small eddies in the Beaufort Sea, *Journal of Geophysical Research: Oceans*, 93(C6), 6669–6684, doi:https://doi.org/10.1029/JC093iC06p06669, 1988.
- Erlingsson, B., Two-Dimensional Deformation Patterns in Sea Ice, *Journal of Glaciology*, 34(118), 301–308, doi:10.3189/S0022143000007061, 1988.
- Fox-Kemper, B., and R. Ferrari, Parameterization of Mixed Layer Eddies. Part II: Prognosis and Impact, *Journal of Physical Oceanography*, 38(6), 1166 – 1179, doi:10.1175/2007JPO3788.1, 2008.

- Fox-Kemper, B., and D. Menemenlis, *Can Large Eddy Simulation Techniques Improve Mesoscale Rich Ocean Models?*, pp. 319–337, American Geophysical Union (AGU), doi:<https://doi.org/10.1029/177GM19>, 2008.
- Fox-Kemper, B., R. Ferrari, and R. Hallberg, Parameterization of Mixed Layer Eddies. Part I: Theory and Diagnosis, *Journal of Physical Oceanography*, *38*(6), 1145 – 1165, doi:[10.1175/2007JPO3792.1](https://doi.org/10.1175/2007JPO3792.1), 2008.
- Fox-Kemper, B., G. Danabasoglu, R. Ferrari, S. Griffies, R. Hallberg, M. Holland, M. Maltrud, S. Peacock, and B. Samuels, Parameterization of mixed layer eddies. III: Implementation and impact in global ocean climate simulations, *Ocean Modelling*, *39*(1), 61–78, doi:<https://doi.org/10.1016/j.ocemod.2010.09.002>, modelling and Understanding the Ocean Mesoscale and Submesoscale, 2011.
- Fox-Kemper, B., S. Bachman, B. Pearson, and S. Reckinger, Principles and advances in subgrid modeling for eddy-rich simulations, 2014.
- Fox-Kemper, B., et al., Challenges and Prospects in Ocean Circulation Models, *Frontiers in Marine Science*, *6*, doi:[10.3389/fmars.2019.00065](https://doi.org/10.3389/fmars.2019.00065), 2019.
- Gent, P. R., and J. C. McWilliams, Isopycnal Mixing in Ocean Circulation Models, *Journal of Physical Oceanography*, *20*(1), 150 – 155, doi:[10.1175/1520-0485\(1990\)020<0150:IMIOCM>2.0.CO;2](https://doi.org/10.1175/1520-0485(1990)020<0150:IMIOCM>2.0.CO;2), 1990.
- Gent, P. R., J. Willebrand, T. J. McDougall, and J. C. McWilliams, Parameterizing Eddy-Induced Tracer Transports in Ocean Circulation Models, *Journal of Physical Oceanography*, *25*(4), 463 – 474, doi:[10.1175/1520-0485\(1995\)025<0463:PEITTI>2.0.CO;2](https://doi.org/10.1175/1520-0485(1995)025<0463:PEITTI>2.0.CO;2), 1995.
- Häkkinen, Sirpa, Coupled ice-ocean dynamics in the marginal ice zones: upwelling/downwelling and eddy generation, *Journal of Geophysical Research*, *91*(C1), 819–832, doi:[10.1029/JC091iC01p00819](https://doi.org/10.1029/JC091iC01p00819), 1986.
- Haney, S., B. Fox-Kemper, K. Julien, and A. Webb, Symmetric and Geostrophic Instabilities in the Wave-Forced Ocean Mixed Layer, *Journal of Physical Oceanography*, *45*(12), 3033 – 3056, doi:[10.1175/JPO-D-15-0044.1](https://doi.org/10.1175/JPO-D-15-0044.1), 2015.
- Hibler, W. D., A Dynamic Thermodynamic Sea Ice Model, *Journal of Physical Oceanography*, *9*(4), 815 – 846, doi:[10.1175/1520-0485\(1979\)009<0815:ADTSIM>2.0.CO;2](https://doi.org/10.1175/1520-0485(1979)009<0815:ADTSIM>2.0.CO;2), 1979.
- Horvat, C., and E. Tziperman, Understanding Melting due to Ocean Eddy Heat Fluxes at the Edge of Sea-Ice Floes, *Geophysical Research Letters*, *45*(18), 9721–9730, doi:<https://doi.org/10.1029/2018GL079363>, 2018.

- Horvat, C., E. Tziperman, and J.-M. Campin, Interaction of sea ice floe size, ocean eddies, and sea ice melting, *Geophysical Research Letters*, *43*(15), 8083–8090, doi:<https://doi.org/10.1002/2016GL069742>, 2016.
- Hoskins, B. J., The role of potential vorticity in symmetric stability and instability, *Quarterly Journal of the Royal Meteorological Society*, *100*(425), 480–482, doi:<https://doi.org/10.1002/qj.49710042520>, 1974.
- Hunkins, K. L., Subsurface eddies in the Arctic ocean, *Deep Sea Research and Oceanographic Abstracts*, *21*(12), 1017–1033, doi:[https://doi.org/10.1016/0011-7471\(74\)90064-3](https://doi.org/10.1016/0011-7471(74)90064-3), 1974.
- Hutter, N., L. Zampieri, and M. Losch, Leads and ridges in Arctic sea ice from RGPS data and a new tracking algorithm, *The Cryosphere*, *13*(2), 627–645, doi:[10.5194/tc-13-627-2019](https://doi.org/10.5194/tc-13-627-2019), 2019.
- IPCC, *IPCC Special Report on the Ocean and Cryosphere in a Changing Climate*, In press., 2019.
- Ivanov, V. V., and P. N. Golovin, Observations and modeling of dense water cascading from the northwestern Laptev Sea shelf, *Journal of Geophysical Research: Oceans*, *112*(C9), doi:<https://doi.org/10.1029/2006JC003882>, 2007.
- Kozlov, I. E., A. V. Artamonova, G. E. Manucharyan, and A. A. Kubryakov, Eddies in the Western Arctic Ocean From Spaceborne SAR Observations Over Open Ocean and Marginal Ice Zones, *Journal of Geophysical Research: Oceans*, *124*(9), 6601–6616, doi:<https://doi.org/10.1029/2019JC015113>, 2019.
- Kozo, T. L., Initial model results for Arctic mixed layer circulation under a re-freezing lead, *Journal of Geophysical Research: Oceans*, *88*(C5), 2926–2934, doi:<https://doi.org/10.1029/JC088iC05p02926>, 1983.
- Manley, T. O., and K. Hunkins, Mesoscale eddies of the Arctic Ocean, *Journal of Geophysical Research: Oceans*, *90*(C3), 4911–4930, doi:<https://doi.org/10.1029/JC090iC03p04911>, 1985.
- Manucharyan, G. E., and A. F. Thompson, Submesoscale Sea Ice-Ocean Interactions in Marginal Ice Zones, *Journal of Geophysical Research: Oceans*, *122*(12), 9455–9475, doi:<https://doi.org/10.1002/2017JC012895>, 2017.
- Manucharyan, G. E., and M.-L. Timmermans, Generation and Separation of Mesoscale Eddies from Surface Ocean Fronts, *Journal of Physical Oceanography*, *43*(12), 2545 – 2562, doi:[10.1175/JPO-D-13-094.1](https://doi.org/10.1175/JPO-D-13-094.1), 2013.

- Marshall, J., C. Hill, L. Perelman, and A. Adcroft, Hydrostatic, quasi-hydrostatic, and nonhydrostatic ocean modeling, *Journal of Geophysical Research: Oceans*, *102*(C3), 5733–5752, doi:<https://doi.org/10.1029/96JC02776>, 1997.
- Maslowski, W., J. Clement Kinney, M. Higgins, and A. Roberts, The Future of Arctic Sea Ice, *Annual Review of Earth and Planetary Sciences*, *40*(1), 625–654, doi:10.1146/annurev-earth-042711-105345, 2012.
- Matsumura, Y., and H. Hasumi, Brine-Driven Eddies under Sea Ice Leads and Their Impact on the Arctic Ocean Mixed Layer, *Journal of Physical Oceanography*, *38*(1), 146 – 163, doi:10.1175/2007JPO3620.1, 2008.
- McWilliams, J. C., Submesoscale currents in the ocean, *Proceedings of the Royal Society A: Mathematical, Physical and Engineering Sciences*, *472*(2189), 20160,117, doi:10.1098/rspa.2016.0117, 2016.
- McWilliams, J. C., Oceanic Frontogenesis, *Annual Review of Marine Science*, *13*(1), 227–253, doi:10.1146/annurev-marine-032320-120725, PMID: 33395349, 2021.
- Mensa, J. A., and M.-L. Timmermans, Characterizing the seasonal cycle of upper-ocean flows under multi-year sea ice, *Ocean Modelling*, *113*, 115–130, doi:<https://doi.org/10.1016/j.ocemod.2017.03.009>, 2017.
- Mensa, J. A., M.-L. Timmermans, I. E. Kozlov, W. J. Williams, and T. M. Özgökmen, Surface Drifter Observations From the Arctic Ocean’s Beaufort Sea: Evidence for Submesoscale Dynamics, *Journal of Geophysical Research: Oceans*, *123*(4), 2635–2645, doi:<https://doi.org/10.1002/2017JC013728>, 2018.
- Miles, M. W., and R. G. Barry, A 5-year satellite climatology of winter sea ice leads in the western Arctic, *Journal of Geophysical Research: Oceans*, *103*(C10), 21,723–21,734, doi:<https://doi.org/10.1029/98JC01997>, 1998.
- Ou, H. W., Geostrophic Adjustment: A Mechanism for Frontogenesis, *Journal of Physical Oceanography*, *14*(6), 994 – 1000, doi:10.1175/1520-0485(1984)014<0994:GAAMFF>2.0.CO;2, 1984.
- Pegau, W. S., and C. A. Paulson, The albedo of Arctic leads in summer, *Annals of Glaciology*, *33*, 221–224, doi:10.3189/172756401781818833, 2001.
- Peralta-Ferriz, C., and R. A. Woodgate, Seasonal and interannual variability of pan-Arctic surface mixed layer properties from 1979 to 2012 from hydrographic data, and the dominance of stratification for multiyear mixed layer depth shoaling, *Progress in Oceanography*, *134*, 19–53, doi:<https://doi.org/10.1016/j.pocean.2014.12.005>, 2015.

- Perovich, D. K., and J. A. Richter-Menge, Loss of Sea Ice in the Arctic, *Annual Review of Marine Science*, 1(1), 417–441, doi:10.1146/annurev.marine.010908.163805, pMID: 21141043, 2009.
- Pham, H. T., and S. Sarkar, The role of turbulence in strong submesoscale fronts of the Bay of Bengal, *Deep Sea Research Part II: Topical Studies in Oceanography*, 168, 104,644, doi:https://doi.org/10.1016/j.dsr2.2019.104644, atmosphere-Ocean Dynamics of Bay of Bengal - Volume I, 2019.
- Pnyushkov, A., I. V. Polyakov, L. Padman, and A. T. Nguyen, Structure and dynamics of mesoscale eddies over the Laptev Sea continental slope in the Arctic Ocean, *Ocean Science*, 14(5), 1329–1347, doi:10.5194/os-14-1329-2018, 2018.
- Proshutinsky, A., R. Krishfield, M.-L. Timmermans, and T. J. M., *McGraw-Hill Yearbook of Science & Technology*, chap. Arctic Ocean freshwater balance., pp. pp. 31–34, McGraw-Hill Book Co., 2013.
- Richter-Menge, J. A., and B. C. Elder, Characteristics of pack ice stress in the Alaskan Beaufort Sea, *Journal of Geophysical Research: Oceans*, 103(C10), 21,817–21,829, doi:https://doi.org/10.1029/98JC01261, 1998.
- Riser, S., et al., Fifteen years of ocean observations with the global Argo array, *Nature Clim. Change*, 6, 145–153, doi:10.1038/nclimate2872, 2016.
- Rudnick, D., D. Costa, K. Johnson, C. Lee, and M.-L. Timmermans, ALPS II – Autonomous Lagrangian Platforms and Sensors., *Tech. rep.*, A Report of the ALPS II Workshop, February 21–24, La Jolla, CA, 66 pp., eds. 2018.
- Schulson, E. M., Compressive shear faults within arctic sea ice: Fracture on scales large and small, *Journal of Geophysical Research: Oceans*, 109(C7), doi:https://doi.org/10.1029/2003JC002108, 2004.
- Semtner, A. J., *A Model for the Thermodynamic Growth of Sea Ice in Numerical Investigation of Climate*, RAND Corporation, Santa Monica, CA, 1975.
- Skyllingstad, E. D., and D. W. Denbo, turbulence beneath sea ice and leads: A coupled sea ice/large-eddy simulation study, *Journal of Geophysical Research: Oceans*, 106(C2), 2477–2497, doi:https://doi.org/10.1029/1999JC000091, 2001.
- Smagorinsky, J., GENERAL CIRCULATION EXPERIMENTS WITH THE PRIMITIVE EQUATIONS: I. THE BASIC EXPERIMENT, *Monthly Weather Review*, 91(3), 99 – 164, doi:10.1175/1520-0493(1963)091<0099:GCEWTP>2.3.CO;2, 1963.

- Smith, D. C., and J. H. Morison, A numerical study of haline convection beneath leads in sea ice, *Journal of Geophysical Research*, 98(C6), 10,069–10,083, doi:10.1029/93JC00137, 1993.
- Smith, G., et al., Polar Ocean Observations: A Critical Gap in the Observing System and Its Effect on Environmental Predictions From Hours to a Season, *Frontiers in Marine Science*, 6, doi:10.3389/fmars.2019.00429, 2019.
- Smith, S. D., R. D. Muench, and C. H. Pease, Polynyas and leads: An overview of physical processes and environment, *Journal of Geophysical Research: Oceans*, 95(C6), 9461–9479, doi:https://doi.org/10.1029/JC095iC06p09461, 1990.
- Smith IV, D. C., and J. H. Morison, Nonhydrostatic haline convection under leads in sea ice, *Journal of Geophysical Research: Oceans*, 103(C2), 3233–3247, doi:https://doi.org/10.1029/97JC02262, 1998.
- Smith IV, D. C., J. W. Lavelle, and H. J. S. Fernando, Arctic Ocean mixed-layer eddy generation under leads in sea ice, *Journal of Geophysical Research: Oceans*, 107(C8), 17–1–17–17, doi:https://doi.org/10.1029/2001JC000822, 2002.
- Steiner, N., et al., Comparing modeled streamfunction, heat and freshwater content in the Arctic Ocean, *Ocean Modelling*, 6(3), 265–284, doi:https://doi.org/10.1016/S1463-5003(03)00013-1, 2004.
- Stern, H. L., and R. E. Moritz, Sea ice kinematics and surface properties from RADARSAT synthetic aperture radar during the SHEBA drift, *Journal of Geophysical Research: Oceans*, 107(C10), SHE 14–1–SHE 14–10, doi:https://doi.org/10.1029/2000JC000472, 2002.
- Stirling, I., The importance of polynyas, ice edges, and leads to marine mammals and birds, *Journal of Marine Systems*, 10(1), 9–21, doi:https://doi.org/10.1016/S0924-7963(96)00054-1, 1997.
- Talley, L., *Descriptive Physical Oceanography: An Introduction*, Elsevier Science, 2011.
- Tandon, A., and C. Garrett, Mixed Layer Restratification Due to a Horizontal Density Gradient, *Journal of Physical Oceanography*, 24(6), 1419 – 1424, doi:10.1175/1520-0485(1994)024<1419:MLRDTA>2.0.CO;2, 1994.
- Tandon, A., and C. Garrett, Geostrophic Adjustment and Restratification of a Mixed Layer with Horizontal Gradients above a Stratified Layer, *Journal of Physical Oceanography*, 25(10), 2229 – 2241, doi:10.1175/1520-0485(1995)025<2229:GAAROA>2.0.CO;2, 1995.

- Thomas, L. N., A. Tandon, and A. Mahadevan, *Submesoscale Processes and Dynamics*, pp. 17–38, American Geophysical Union (AGU), doi:<https://doi.org/10.1029/177GM04>, 2008.
- Timmermans, M., J. Toole, A. Proshutinsky, R. Krishfield, and A. Plueddemann, Eddies in the Canada Basin, Arctic Ocean, Observed from Ice Tethered Profilers, in *AGU Fall Meeting Abstracts*, vol. 2006, pp. OS53D–03, 2006.
- Timmermans, M.-L., and J. Marshall, Understanding Arctic Ocean Circulation: A Review of Ocean Dynamics in a Changing Climate, *Journal of Geophysical Research: Oceans*, *125*(4), e2018JC014378, doi:<https://doi.org/10.1029/2018JC014378>, e2018JC014378 10.1029/2018JC014378, 2020.
- Timmermans, M.-L., S. Cole, and J. Toole, Horizontal Density Structure and Restratification of the Arctic Ocean Surface Layer, *Journal of Physical Oceanography*, *42*(4), 659 – 668, doi:10.1175/JPO-D-11-0125.1, 2012.
- Toole, J. M., R. A. Krishfield, M.-L. Timmermans, and A. Proshutinsky, The Ice-Tethered Profiler: Argo of the Arctic, *Oceanography, issue volume*, doi:10.5670/oceanog.2011.64, 2011.
- Vallis, G., *Atmospheric and Oceanic Fluid Dynamics: Fundamentals and Large-scale Circulation*, Cambridge University Press, 2006.
- Vavrus, S., and S. Harrison, The impact of sea ice dynamics on the Arctic climate system, *Climate Dynamics*, *20*, other: DOI 10.1007/s00382-003-0309-5, 2003.
- Wadhams, P., A. Gill, and P. Linden, Transects by submarine of the East Greenland Polar Front, *Deep Sea Research Part A. Oceanographic Research Papers*, *26*(12), 1311–1327, doi:[https://doi.org/10.1016/0198-0149\(79\)90001-3](https://doi.org/10.1016/0198-0149(79)90001-3), 1979.
- Wernecke, A., and L. Kaleschke, Lead detection in Arctic sea ice from CryoSat-2: quality assessment, lead area fraction and width distribution, *The Cryosphere*, *9*(5), 1955–1968, doi:10.5194/tc-9-1955-2015, 2015.
- Wettlaufer, J. S., M. G. Worster, and H. E. Huppert, The phase evolution of Young Sea Ice, *Geophysical Research Letters*, *24*(10), 1251–1254, doi:<https://doi.org/10.1029/97GL00877>, 1997.
- Willmes, S., and G. Heinemann, Sea-Ice Wintertime Lead Frequencies and Regional Characteristics in the Arctic, 2003–2015, *Remote Sensing*, *8*(1), doi:10.3390/rs8010004, 2016.

- Winton, M., A Reformulated Three-Layer Sea Ice Model, *Journal of Atmospheric and Oceanic Technology*, 17(4), 525 – 531, doi:10.1175/1520-0426(2000)017<0525:ARTLSI>2.0.CO;2, 2000.
- Zhang, J., D. Rothrock, and M. Steele, Recent Changes in Arctic Sea Ice: The Interplay between Ice Dynamics and Thermodynamics, *Journal of Climate - J CLIMATE*, 13, 3099–3114, doi:10.1175/1520-0442(2000)013<3099:RCIASI>2.0.CO;2, 2000.
- Zhao, M., and M.-L. Timmermans, Vertical scales and dynamics of eddies in the Arctic Ocean’s Canada Basin, *Journal of Geophysical Research: Oceans*, 120(12), 8195–8209, doi:<https://doi.org/10.1002/2015JC011251>, 2015.
- Zhao, M., M.-L. Timmermans, S. Cole, R. Krishfield, A. Proshutinsky, and J. Toole, Characterizing the eddy field in the Arctic Ocean halocline, *Journal of Geophysical Research: Oceans*, 119(12), 8800–8817, doi:<https://doi.org/10.1002/2014JC010488>, 2014.
- Zhao, M., M.-L. Timmermans, S. Cole, R. Krishfield, and J. Toole, Evolution of the eddy field in the Arctic Ocean’s Canada Basin, 2005–2015, *Geophysical Research Letters*, 43(15), 8106–8114, doi:<https://doi.org/10.1002/2016GL069671>, 2016.